# The Microstructure, Morphology and Mechanical Properties of Rapidly Solidified Al-10wt%Si Alloy

by

William Andrew Blake Hearn

A thesis submitted in partial fulfillment of the requirements for the degree of

Master of Science
in
Materials Engineering

Department of Chemical and Materials Engineering
University of Alberta

# ABSTRACT

Hypoeutectic Al-Si alloys are widely used in both the automotive and aerospace industries, due to their strong corrosion resistance, good castability and relatively high strength-to-weight ratio. Despite this wide use, these alloys have a major limitation related to the Si phase that forms within the eutectic structure. In the as-cast state this eutectic Si phase forms a flaky lamellar morphology that combined with the inherent brittle nature of Si significantly reduces the ductility and the mechanical property performance of these alloys.

To improve and modify this eutectic Si phase, alloy additions and/or rapid solidification can be used. However, the underlying mechanisms behind this Si phase refinement are poorly understood, especially for modification via rapid solidification. As such, the research in this thesis aimed to shed light on how rapid solidification affects the microstructure of hypoeutectic Al-Si alloys.

To conduct this analysis a rapidly solidified Al-10wt%Si alloy, that was produced under varying rapid solidification conditions, was examined. The microstructure of this Al-10Si alloy was found to consist of a primary α-Al phase and a secondary Al + Si eutectic structure. From an analysis of the primary α-Al phase two distinct growth directions were identified: a <100> growth and a <110> growth. In addition, the formation of a "seaweed" or "coral-like" α-Al structure was observed. The transition in growth from <100> to <110>, along with the propensity for seaweed growth, was found to become more prevalent as solidification became more rapid, suggesting that rapid solidification caused this shift in the α-Al morphology.

The analysis of the secondary Al + Si eutectic structure was done via a characterization of the Si growth morphology, where the observed Si morphologies were mapped as a function of the local eutectic solidification conditions. From this analysis it was found that the Si morphology transitioned from flaky → fibrous → globular + fibrous → globular as solidification became more rapid; where the globular morphology was considered to be the finest morphology and the flaky morphology was considered the coarsest morphology. The beginning of the flaky → fibrous, fibrous → globular + fibrous and the globular + fibrous → globular transitions occurred at local eutectic cooling rates of ~60 K/s, ~350 K/s, and ~1200 K/s respectively.

Further analysis related these microstructural changes to the hardness of the Al-10Si alloy, and in doing so it was found that the alloy hardness increased monotonically with the Si morphology. By shifting to a globular Si the Al-10Si alloy was able to achieve improvements in hardness of up to 24%. Indicating that control of this morphology is an important factor when considering the mechanical properties and characteristics of hypoeutectic Al-Si alloys. Given that this Si morphology is the key to improving mechanical property performance in hypoeutectic Al-Si alloys, this work recommends that other rapid solidification processes adjust their processing conditions to invoke this globular Si morphology.

# ACKNOWLEDGEMENTS

I would first like to extend my most sincere gratitude to my supervisor, Professor Hani Henein, as his support during my research cannot be explained in words. I would not be in my current position, nor have the passion for what I do if it was not for his guidance.

I would like to thank Dr. Mark Gallerneault for our many spirited discussions that helped me gain a deeper understanding of my work, along with helping to ignite my passion.

I would like to thank Professor Michel Rappaz for our conversations when I started my thesis, as they were in-valuable and helped guide me throughout my research.

I would like to thank Professor Guillaume Reinhart for the fantastic discussions that we had and his many helpful suggestions.

Thanks to Bob Smith and Clark Bicknell (machine shop) and Walter Bodez, Les Dean and Richard Cooper (instrument shop) for their technical support.

Thanks to Nathan Gerein for his help and support with the FE-SEM and to Diane Caird for her help conducting XRD analysis.

I would like to thank my partner in crime Dr. Abdoul-Aziz Bogno for his guidance during my work but more importantly his friendship. Without him my research would not have been the same.

I would like to thank Dr. Jonas Valloton for all his help, from the early morning 3-hour EBSD sessions to the many helpful discussions we had at his desk (as I invaded his personal space).

I thank the many members of the AMPL research group at the University of Alberta. All of you were so amazing and I truly cherish the great times that we had together.

I would like to thank my entire family for all their love and support, in particular, I would like to thank my mother, Dr. Nataliya Hearn, and my father, Bill Hearn.

Most importantly I would like to express how thankful I am to my fiancé, Ida Mannisto, as her love, caring and support are things that I cannot imagine living without.

Lastly, I would like to thank NSERC and Equispheres for funding this project.

# TABLE OF CONTENTS

# LIST OF TABLES

# LIST OF FIGURES

# LIST OF SYMBOLS

## *Greek Symbols*

| | | |
|---|---|---|
| λ | $m$ | Secondary Dendrite Arm Spacing |
| $\Gamma$ | $mK$ | Gibbs-Thompson Coefficient |
| $\rho$ | $kgm^{-3}$ | Density |
| $\varphi$ | $-$ | Extremum Condition Parameter |
| $\sigma_y$ | $MPa$ | Yield Strength |

## *Latin Symbols*

| | | |
|---|---|---|
| $C_d$ | $-$ | Drag Coefficient |
| $C_L$ | $wt\%$ | Solute Composition in the Liquid |
| $Cp_m$ | $JK^{-1}$ | Droplet Specific Heat |
| $CR_{eut}$ | $Km^{-1}$ | Local Eutectic Cooling Rate |
| $D$ | $m$ | Droplet Diameter |
| $D_G$ | $m$ | Grain Diameter |
| $D(L)$ | $m^2s^{-1}$ | Diffusion Coefficient |
| $f$ | $-$ | Phase Fraction |
| $g$ | $ms^{-2}$ | Acceleration due to Gravity |
| $G_{eut}$ | $Km^{-1}$ | Local Eutectic Thermal Gradient |
| $\Delta H$ | $J$ | Latent Heat of Fusion |
| $h_{eff}$ | $Wm^{-2}K^{-1}$ | Effective Heat Transfer Coefficient |
| $k$ | $-$ | Partition Coefficient |
| $k_T$ | $Wm^{-1}K^{-1}$ | Thermal Conductivity |
| $L$ | $Jkg$ | Latent Heat of Fusion |
| $M$ | $\mu m^3s^{-1}$ | Coarsening Parameter |

|  |  |  |
|---|---|---|
| $m$ | $K$ | Slope of Liquidus Line |
| $\frac{m_\alpha}{m_S}$ | $wt\%$ | Solute Composition in the Liquid |
| $Nu$ | $-$ | Nusselt Number |
| $P$ | $m$ | Perimeter Length of Particle |
| $Pr$ | $-$ | Prandtl Number |
| $Re$ | $-$ | Reynold Number |
| $r_f$ | $m$ | Freezing Radius of Solidification Front |
| $S$ | $m^2$ | Surface Area of Particle |
| $\dot{T}$ | $Ks^{-1}$ | Cooling Rate during Coarsening |
| $\Delta t$ | $s$ | Total Time for Solidification |
| $\Delta T$ | $K$ | Temperature Interval of Solidification |
| $T_E'$ | $K$ | Eutectic Nucleation Temperature |
| $T_E$ | $K$ | Eutectic Temperature |
| $\Delta T_E$ | $K$ | Eutectic Nucleation Undercooling |
| $\Delta T_{eut}$ | $K$ | Local Undercooling during Eutectic Growth |
| $T_L$ | $K$ | Liquidus Temperature |
| $T_m$ | $K$ | Droplet Temperature |
| $T_P$ | $K$ | Primary Nucleation Temperature |
| $\Delta T_P$ | $K$ | Primary Nucleation Undercooling |
| $T_R$ | $K$ | End of Recalescence Temperature |
| $\dot{T}_S$ | $Ks^{-1}$ | Solidification Cooling Rate |
| $t_{sl}$ | $s$ | Local Solidification Time during Coarsening |
| $\Delta T_{SL}$ | $K$ | Temperature Interval of Coarsening |
| $T_S$ | $K$ | Droplet Surface Temperature |
| $T_\infty$ | $K$ | Ambient Gas Temperature |

| | | |
|---|---|---|
| $v$ | $ms^{-1}$ | Droplet Relative Velocity |
| $v^*$ | $ms^{-1}$ | Local Eutectic Growth Velocity |
| $W_E$ | $wt\%$ | Eutectic Weight Fraction |

# 1 INTRODUCTION

The hypoeutectic Al-Si alloy system is known for its strong corrosion resistance, good castability and relatively high strength-to-weight ratio [1]. These characteristics make it an important cast alloy systems and have led to its widespread usage in both the automotive and aerospace industries [2]. However, even with these desirable properties, hypoeutectic Al-Si alloys have limited usage as structural materials, due to the inherent characteristics of the Si phase that forms within the eutectic structure. Typically, this eutectic Si phase forms a high aspect ratio morphology that, in combination with the brittle nature of Si, decreases the ductility of the alloy and leads to poor structural performance.

While it is known that the Si morphology can be modified, using alloying additions or by using rapid solidification [3], how this modification occurs is poorly understood. This is especially true when looking at Si modification via rapid solidification, as currently no mechanism can explain how rapid solidification refines and modifies the eutectic Si phase.

To better understand this phenomenon the research in this thesis examined the influence of rapid solidification on an Al-10wt%Si alloy. This Al-10Si alloy was produced using Impulse Atomization (IA), as this technique achieves both high cooling rates and large undercoolings during processing. IA also allows for a wide range of cooling rates and undercoolings to be achieved, making it possible to catalogue the influence of rapid solidification over an extensive range of conditions.

The main objective of this work was to categorize how rapid solidification affected the microstructure of the Al-10Si alloy and to relate these shifts in the microstructure to the mechanical properties. In doing so it would allow for the development of a Process → Microstructure → Property relationship, that could help quantify the necessary conditions and microstructure that maximized the alloy properties. An additional objective of this work was to define the shifts in the eutectic Si phase morphology, during refinement, as a function of specific solidification conditions. To accomplish this a solidification microstructure map was developed that related the observed Si morphologies to the local solidification conditions of the eutectic structure.

# 2 LITERATURE REVIEW

## 2.1 AL-SI ALLOY SYSTEM

The Al-Si alloy system is a binary eutectic, shown in Figure 2-1, where there is limited solid solubility of Si in Al and no solid solubility of Al in Si. In this system, there is only one invariant reaction which occurs at a temperature of 577°C and a Si content of 12.6wt%. At this eutectic point the liquid phase turns into an $\alpha + \beta$ eutectic structure, where the $\alpha$ phase is predominantly Al and the $\beta$ phase is predominantly Si [4].

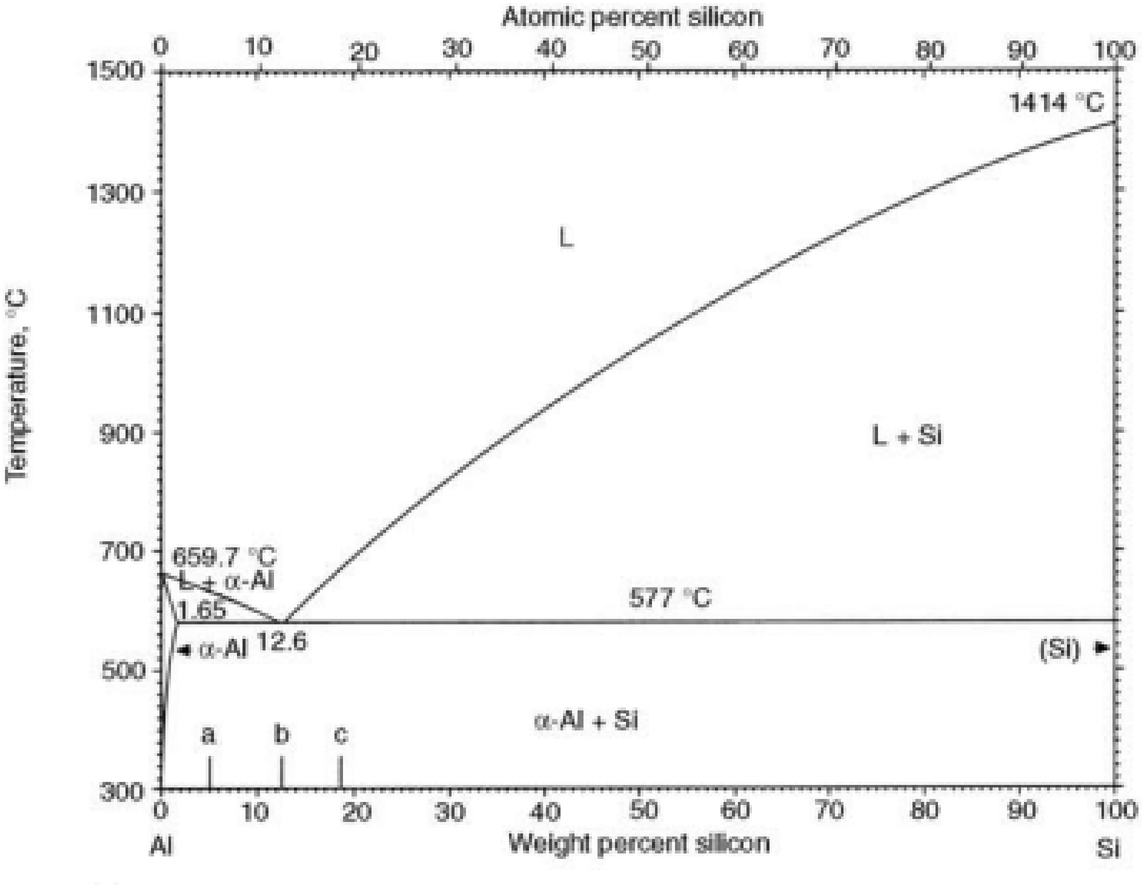

Figure 2-1: Al-Si phase diagram *[5]*.

While the temperature plateau of the eutectic point is 577°C this plateau can change depending on the cooling rate. If the cooling rate increases it will make the system behave as if the eutectic point was shifted to higher Si contents, causing a depression of the eutectic temperature. This depression, caused by an increased cooling rate, can be explained by the coupled region effect.

A coupled region represents a field within a phase diagram where diffusion into the liquid can occur at the solid/liquid front [4]. Since Si is a non-metal, it has directed covalent bonds that cause it to grow anisotropically into faceted crystals. This faceted growth of Si requires more undercooling than the non-faceted growth of Al [4], leading to the formation of an asymmetric coupled zone that is skewed towards the Si-rich portion of the phase diagram. As a consequence, even if the composition of the alloy is hypereutectic (>12.6 wt.% Si), the first structure that forms, under undercooled conditions, is an α + β eutectic structure. A schematic outlining the asymmetric coupled zone for the Al-Si system is shown below in Figure 2-2.

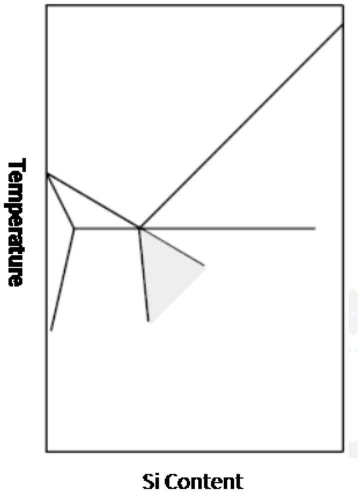

Figure 2-2: Schematic outlining the asymmetric coupled zone of the Al-Si system *[6]*.

## 2.2 AL-SI ALLOY COMPOSITION

The Si content of an Al-Si alloy is an important factor to consider as it will impact the phases and components that form during solidification. As well, this Si content will affect the mechanical properties, where an increase in Si will increase the hardness, Young's modulus, porosity, and brittleness of the alloy [7] [8].

In this thesis a hypoeutectic Al-Si alloy is examined, at a composition of Al-10wt%Si. Under equilibrium solidification conditions this alloy will form a two-component structure consisting of:

1. A primary α-Al phase, and,
2. A secondary Al + Si eutectic structure.

This typical two-component microstructure can be seen below in Figure 2-3.

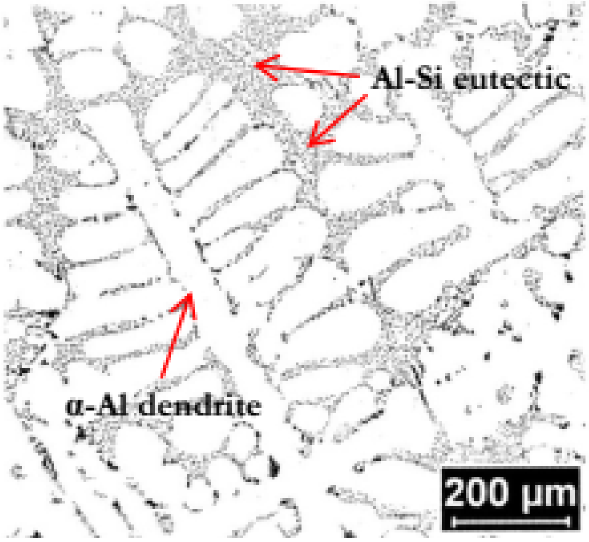

Figure 2-3: Typical two-component microstructure of a hypoeutectic Al-Si alloy *[9]*.

The formation of this microstructure follows a two-part solidification path that initially involves the nucleation and growth of the primary α-Al phase, followed by the nucleation and growth of the Al + Si eutectic structure.

## 2.3 GROWTH OF THE PRIMARY $\alpha$-AL PHASE IN AL-SI ALLOYS

In an as-cast state the primary α-Al phase will form into non-faceted dendrites, where the spatial orientation of each dendrite is related to the direction of heat flow and the thermal gradient [10].

Regarding the overall orientation of the primary α-Al dendrites this is determined by the lattice symmetry and the physical properties at the solidification front. Typically, FCC materials like Al will grow in the <100> crystallographic direction, as this is the easiest growth direction for cubic lattice materials [10]. However, this growth direction can change depending on the conditions during solidification and the chemical composition of the alloy [11] [12] [13] [14].

The morphology of these growing α-Al dendrites is dependent on the perturbations and the instabilities at the solidification front, which come about due to undercooling in the liquid [10]. This undercooling, experienced during growth, consists of 4 parts: (1) thermal undercooling, (2) constitutional undercooling, (3) curvature undercooling and (4) kinetic undercooling.

While all play an important role, the constitutional undercooling is the critical factor that determines whether perturbations will form at the solidification front [10]. With this concept the constitutional undercooling was used to develop a criterion to describe the critical cooling rate for a flat solidification front [10]:

$$\frac{G_T}{v_R} \geq \frac{\Delta T_C}{k D_L} \tag{2-1}$$

Where $\frac{G_T}{v_R}$ is the cooling rate, $\Delta T_C$ is the constitutional supercooling, k is the partition coefficient and $D_L$ is the diffusion coefficient.

If the cooling rate exceeds the criterion in Equation 2-1, then the flat solidification front transitions into a front with instabilities. These instabilities in turn cause a planar to columnar transition in the α-Al dendrite morphology [10] [15]. If these instabilities continue to pile-up it leads to more transitions in the α-Al dendrite morphology, with a schematic of these transitions being shown in Figure 2-4.

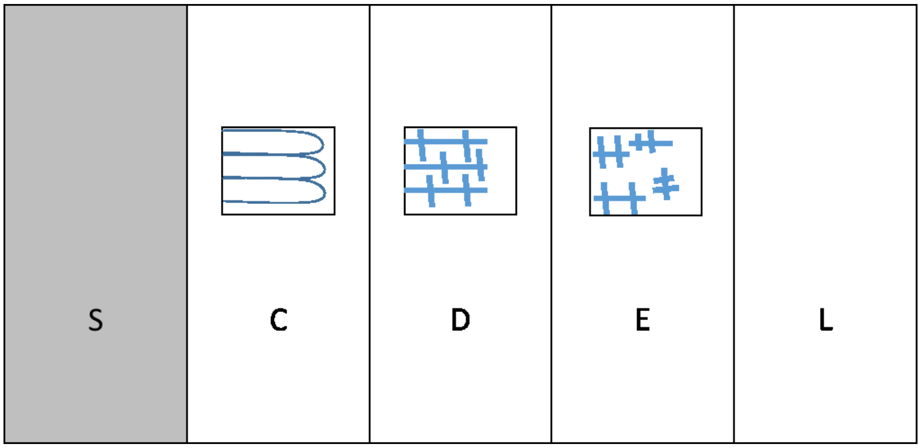

Figure 2-4: Schematic of the transitions in the α-Al dendrite morphology. S refers to a planar front, C refers to a columnar/cellular front, D refers to a dendritic front, E refers to an equiaxed front and L is a purely liquid front.

Examining Figure 2-4, the other key transition in the α-Al growth morphology occurs between the cellular and dendritic morphologies. During this shift there is a loss of stability at the spherical tip of the growing dendrites, leading to branching of the dendrites and the formation of secondary arms [16].

The spacing and thickness of these secondary arms is directly related to the solidification time, where an increase in solidification time increases the secondary dendrite arm spacing. This relationship was found in the work of Spear and Gardner [17] and is shown below:

$$\lambda = 5.5(Mt_{sl})^{\frac{1}{3}} \qquad (2\text{-}2)$$

Where λ is the secondary dendrite arm spacing (SDAS), $t_{sl}$ is the local solidification time for coarsening and M is the coarsening parameter.

The spacing between secondary dendrite arms is an important factor for Al alloys, as a decrease in the SDAS leads to a finer microstructure and improves the mechanical properties of the alloy [18] [19] [20].

## 2.4 NUCLEATION OF THE EUTECTIC STRUCTURE IN AL-SI ALLOYS

When examining the nucleation of the eutectic structure, in Al-Si alloys, there are three proposed growth modes, shown in Figure 2-5 [21] [22] [23]:

1. Nucleation at or adjacent to the mold wall,
2. Nucleation on the primary α-Al dendrites, and,
3. Heterogeneous nucleation within the interdendritic liquid.

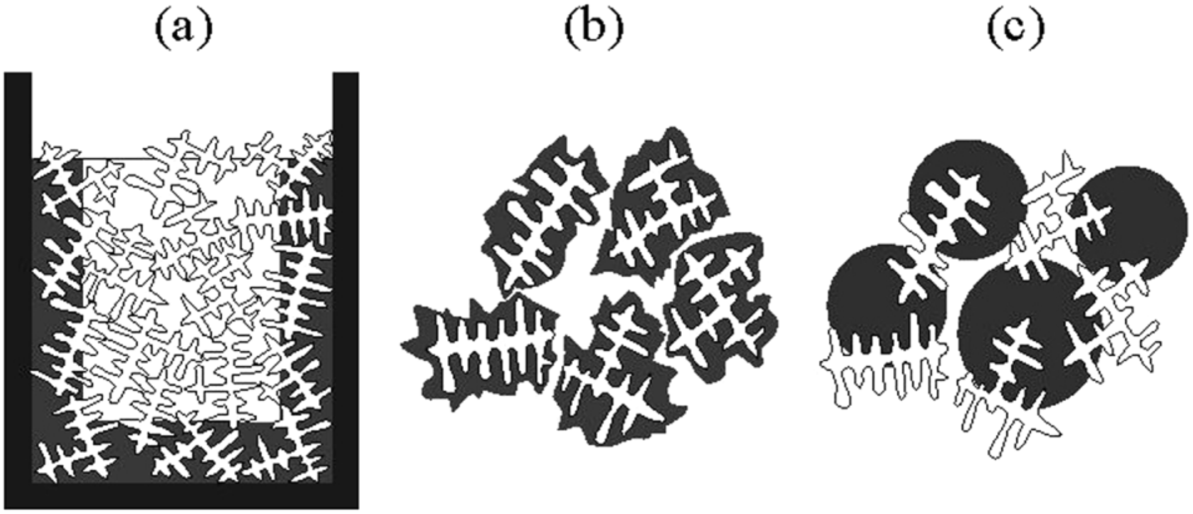

Figure 2-5: Eutectic nucleation modes in Al-Si alloys: (a) Nucleation at the mold wall (b) Nucleation and growth off the α-Al dendrites. (c) Heterogeneous nucleation within the interdendritic liquid *[21]*.

The type of growth mode that occurs is dependent on the nucleation of the Si phase, as the eutectic structure does not begin to grow until the first Si phase forms [22]. It has been suggested that the nucleation of Si is influenced by oxide films and by impurities within the melt, as both are attractive nucleants for Si [24] [25].

In an unmodified Al-Si alloy, the eutectic structure typically nucleates at the α-Al dendrite tips [22] [23]. However, if the alloy is modified with an alloy addition, the nucleation of the eutectic shifts to the mold wall [26] or to locations within the interdendritic liquid [21] [26].

The cause of this shift is thought to be due to the available nucleants within the melt. In an unmodified Al-Si alloy, the Si nucleates at the α-Al dendrites, as there is a noticeable presence of impurities and oxide films there [24]. However, with a modified Al-Si alloy these oxides and impurities at the α-Al dendrites are less prevalent, as many form with the alloy additions instead. This removal of favorable Si nuclei, from the dendrite tips, makes it possible for nucleation to occur within the interdendritic liquid or at the mold walls [27].

## 2.5 GROWTH OF THE EUTECTIC STRUCTURE IN AL-SI ALLOYS

During the growth of the Al + Si eutectic structure, the Si acts as the leading phase at the solidification interface, with the Al growing around it [28]. The growth of the Si phase is faceted, while the growth of the surrounding Al matrix is non-faceted. This combination of faceted and non-faceted growth leads to a complex and irregular eutectic structure, shown in Figure 2-6, as the faceted Si phase can only grow along well-defined planes and directions [28].

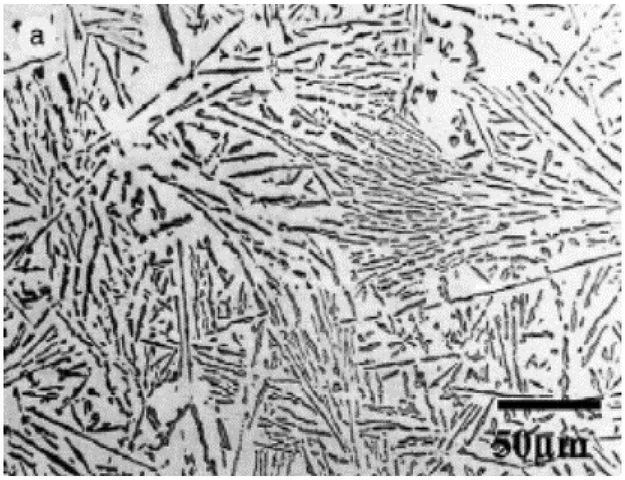

Figure 2-6: Example of irregular eutectic growth in an Al-12.5wt%Si alloy *[6]*.

The faceted nature of Si also causes it to form into a flaky lamellar morphology [10]. This flaky Si growth is believed to occur via twinning, through the twin plane re-entrant edge (TPRE) mechanism [29], shown in Figure 2-7.

The equilibrium habit of Si is an octahedral bound by eight (111) planes. If a twin is introduced into the Si crystal, there are six edges of intersection with this (111) plane and two external angles between the planes. One at 141° and one at 219° [4]. The bounding plane at 141° forms a re-entrant corner, while the bounding plane at 219° forms a ridge. The TPRE mechanism suggests that the re-entrant corners are more favorable for atomic bonding of the Si and as such act as Si nucleation sites. The presence of these re-entrant corners leads to rapid growth in the (211) direction [4]; where the growth of the Si continues until it becomes a trigonal solid that is completely bounded by ridges. Or if the crystal has two or more twins (giving it numerous re-entrant corners), the Si keeps growing in the (211) direction, upon these re-entrant corners, until it can no longer do so [4].

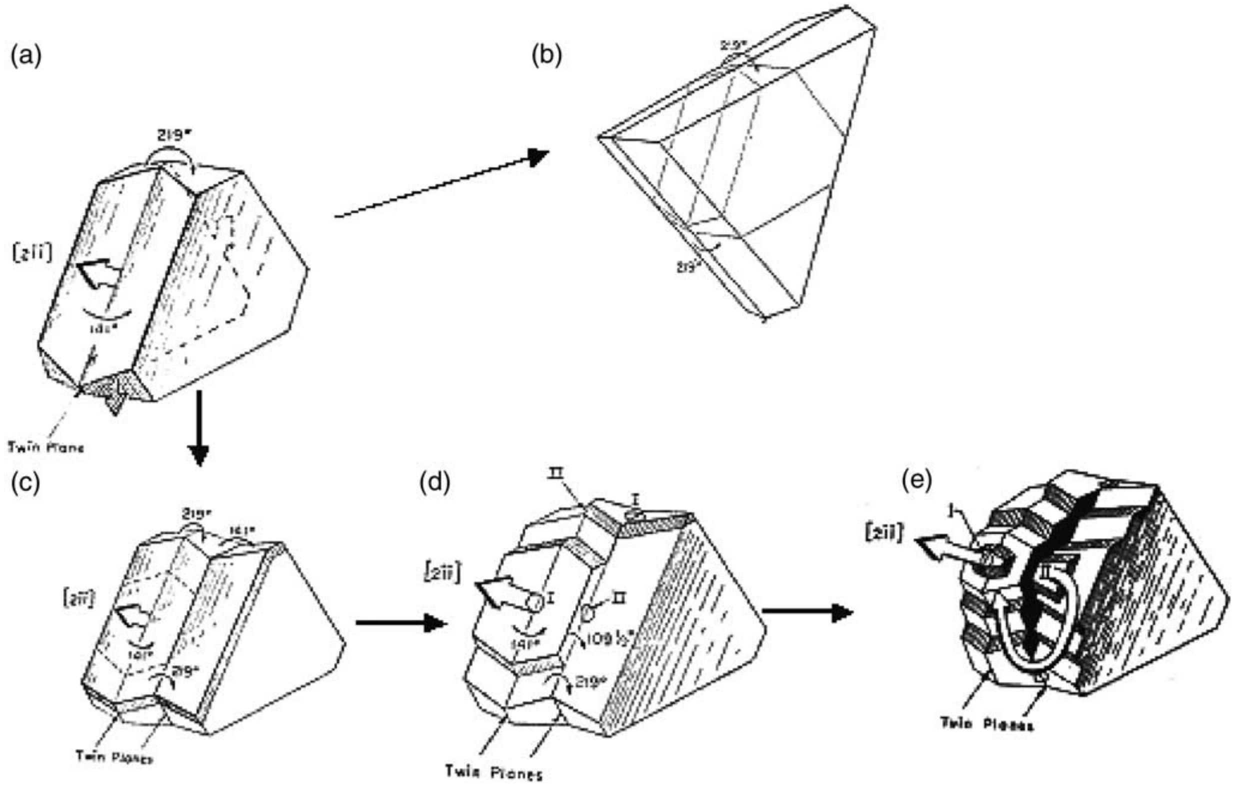

Figure 2-7: Schematic of the TPRE mechanism. (a) Si crystal with a single twin. (b) Closure of a twin due to ridge formation on the edge. (c) Si crystal with two twins. (d) & (e) Nucleation and continued growth of the Si from re-entrant corners in the (211) direction *[29]*.

The outwards growth of Si, via the TPRE, is also influenced by the local growth velocity. At low growth velocities branching of the Si occurs via displacement twinning, shown in Figure 2-8, where the growth of twins will occur laterally with respect to the main Si flakes [4].

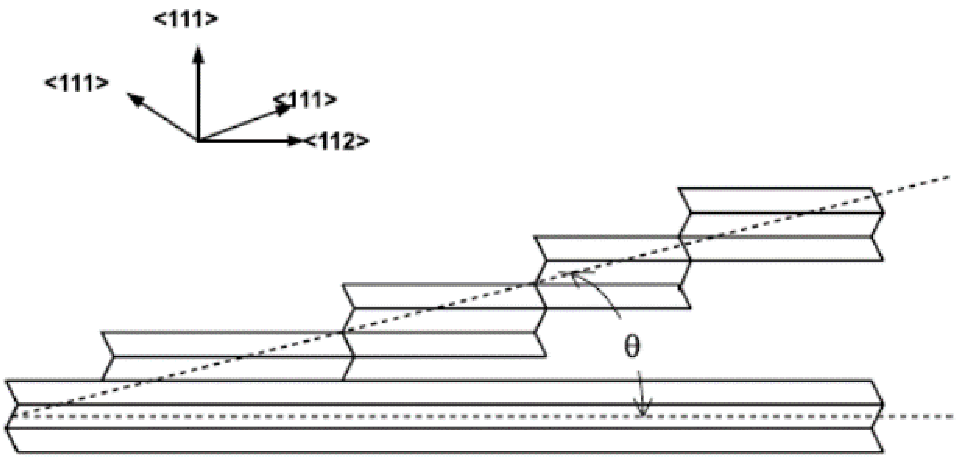

Figure 2-8: Schematic of the flake like Si growth due to displacement twinning *[30]*.

At higher growth velocities multiple twinning occurs, shown in Figure 2-9. This increased growth velocity increases the Si inter-flake spacing, causing the Si to grow outwards in order to ensure that the Si required for further growth is readily available. The growth of these branched Si flakes occurs at angles that are integer multiples of 70.5° [4].

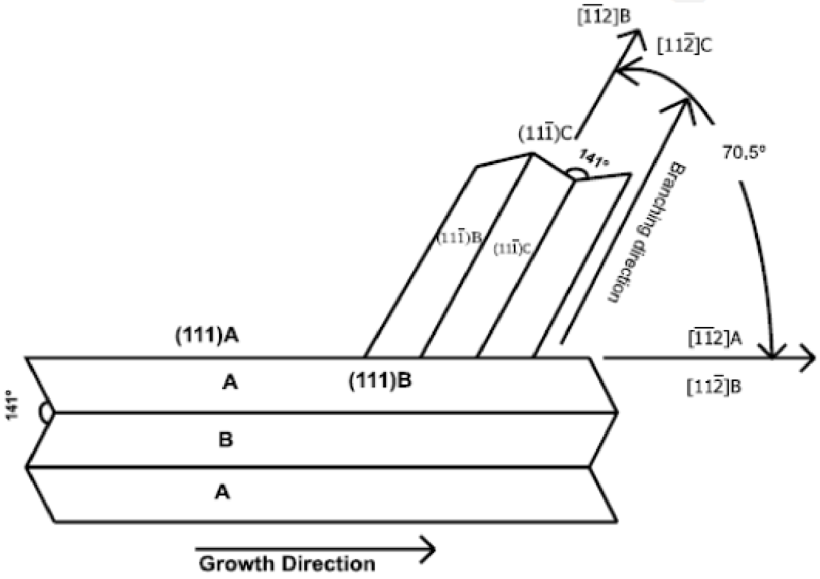

Figure 2-9: Schematic of the flake like Si growth due to multiple twinning *[30]*.

While the TPRE mechanism adequately describes Si growth in unmodified Al-Si alloys, it does not explain the Si growth when modifiers are present. Results from TEM experiments by Lu et al. [31] and Shamsuzzoha et al. [30] found that Si twinning is much more frequent in modified alloys than in unmodified alloys [4]. This finding leads to the conclusion that, in modified alloys, Si growth occurs via a layer mechanism (Figure 2-10) which involves the atomic attachment of Si at ledges.

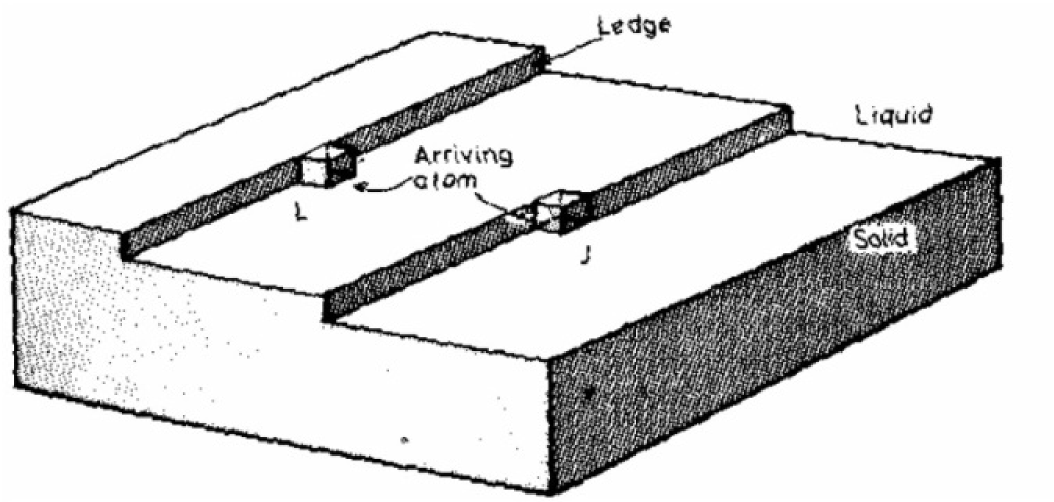

Figure 2-10: Schematic of the layer growth mechanism where Si growth occurs via atomic attachment to the ledges of the Si crystal *[32]*.

Although this layer mechanism explains Si growth in modified alloys, it does not explain how the Si nucleated. In the TPRE mechanism Si nucleation is considered to occur only at re-entrant corners. However, for this to be true the Si had to of grown as a perfect crystal. This assertion was disproven in work by Kitamura et al. [33] and Sunagawa et al. [34], as they found that screw dislocations could also act as nucleation sites for Si.

These results led to the conclusion that Si nucleation can occur at many features, beyond just re-entrant corners. So, the concept of Si nucleation was extended out to include four types of preferential growth sites: (1) kinks, (2) steps, (3) re-entrant corners and (4) surface nucleation sites [4], where their effectiveness for Si nucleation decreases going from kinks to surface nucleation sites. Essentially, the type of nucleation site determines whether the growth of the Si occurs via the TPRE or via the layer mechanism.

## 2.6 MODIFICATION OF EUTECTIC SI PHASE

While the equilibrium growth of the eutectic Si phase is an elongated lamellar structure, it is possible to modify it into a fibrous and rod-like shape. This lamella → rod transition of the Si morphology is sought after as it noticeably improves the mechanical properties of the alloy. With typical effects being a 50% improvement in the tensile strength and a three-fold improvement in the ductility, for cast Al-Si alloys [35].

Work by Hedge et al. [36] categorized this lamella → rod transition of the Si morphology into six classes of refinement. This classification, shown in Table 2-1, was meant to highlight the various stages and Si morphologies during said transition.

Table 2-1: Classification of the lamella → rod Si transition in Al-Si alloys *[36]*.

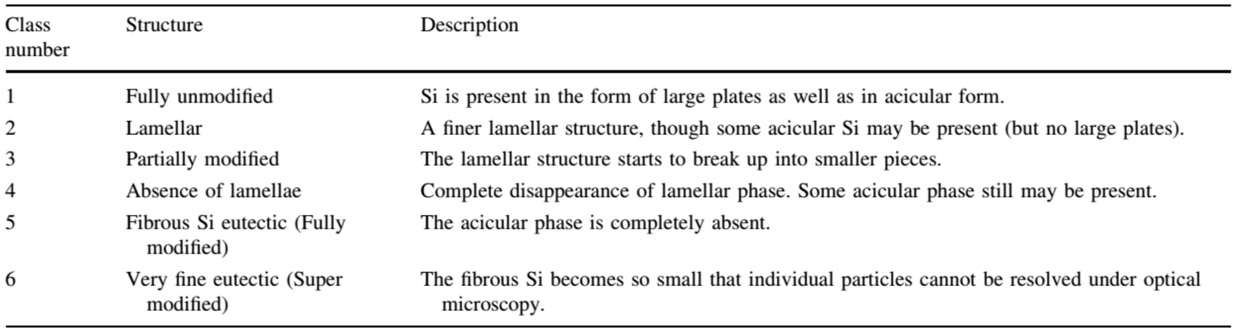

| Class number | Structure | Description |
|---|---|---|
| 1 | Fully unmodified | Si is present in the form of large plates as well as in acicular form. |
| 2 | Lamellar | A finer lamellar structure, though some acicular Si may be present (but no large plates). |
| 3 | Partially modified | The lamellar structure starts to break up into smaller pieces. |
| 4 | Absence of lamellae | Complete disappearance of lamellar phase. Some acicular phase still may be present. |
| 5 | Fibrous Si eutectic (Fully modified) | The acicular phase is completely absent. |
| 6 | Very fine eutectic (Super modified) | The fibrous Si becomes so small that individual particles cannot be resolved under optical microscopy. |

To achieve this Si modification two techniques are used [3]:

1. Use of alloy additions, and,
2. Control of the solidification conditions.

In this section the influence of both techniques, on the modification of the eutectic Si morphology, is examined.

### 2.6.1 **Influence of Alloy Additions**

The first technique that can be used to modify the Si morphology is the use of alloy additions. From past work, it was found that a wide range of additions can be used to achieve the lamella → rod transition of the eutectic Si, with the most common additions being Na, Sr, Ca, Ba, Li and various rare earth elements [10] [37] [38] [39] [40].

To explain how these alloying additions refined the Si morphology two groups of theories have been developed [36]:

1. Restricted nucleation theory, and,
2. Restricted growth theory.

Restricted nucleation theory considers that the refinement of the Si phase is achieved by limiting the number of Si nucleation events. Here alloy additions are considered to be inherently reactive, meaning that they will want to form compounds with preexisting nuclei within the melt. This removal of potential nuclei significantly reduces the number of possible Si nucleation events, suppressing eutectic nucleation. With eutectic nucleation suppressed the Si undercools, increasing the driving force for solidification [41] and in turn, causing refinement of the Si morphology [36].

Restricted growth on the other hand considers Si refinement to be caused by alloy additions impeding the growth of Si. In this theory, it is believed that the alloy additions move directly to potential sites for Si growth and inhibit the Si from growing any further [36].

The most commonly accepted mechanism to describe modification via restricted growth is Impurity Induced Twinning (IIT). IIT considers that alloy additions act as impurities that “poison” growing layers of Si. During this “poisoning” the alloy additions get adsorbed onto surface steps and kinks, preventing the attachment of Si atoms to the crystal [4]. These adsorbed atoms induce twinning by altering the atomic stacking sequence, as new Si layers seek to grow around these atoms.

While these two theories are commonly accepted there are still noticeable issues and concerns with both.

Regarding restricted nucleation theory, it cannot explain the large undercoolings that are observed when modifiers are present [4].

As for restricted growth theory some questions remain regarding the IIT mechanism. For one, it cannot not explain why Si growth occurs via the TPRE in unmodified alloys, as IIT can only explain Si modification via the layer growth mechanism. The IIT mechanism also cannot explain the difference between the best theoretical and the best practical atomic radius for modifier elements, nor can it explain the phenomenon of over-modification [4].

These lingering concerns indicate that while there is an understanding of eutectic Si modification via alloy additions, some questions still remain.

### 2.6.2 **Influence of Solidification Conditions**

The other method to refine the Si morphology is through the control of the solidification conditions, specifically through the control of the cooling rate. By increasing the cooling rate, it is shown that the Si morphology can be modified from a flake-like lamellar structure, into a fibrous and rod-like shape. While previous works have highlighted this transition in the Si morphology (see Table 2-1) the underlying mechanism(s) as to why this modification took place have not been identified, nor have these transitions in the Si morphology been linked to technical cooling rates or solidification conditions.

Initially it was proposed by Thall and Chalmers [42] that this modification, via cooling rate, was related to the surface energy of the Al/Si solid interface [4]. In this mechanism Thall and Chalmers proposed that the advance of the interface was dependent on a balance between the heat flow and the latent heat of fusion [4]. Using this framework, it was found that (theoretically) the Al phase will grow faster than the Si phase. So, as the cooling rate increases it was thought that this leading growth of the Al becomes more and more prominent, until it grows so far ahead of the Si that it encapsulates it and forces it to become refined. This encapsulation of the Si, by the faster growing Al, is shown schematically in Figure 2-11.

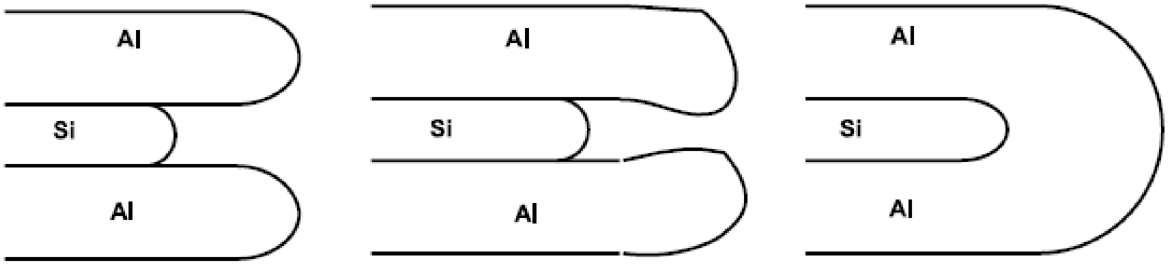

Figure 2-11: Mechanism of eutectic Si refinement, via surface energy, that was proposed by Thall and Chalmers *[42]*.

While in theory this mechanism worked it was found that Si and not Al was the leading phase at the eutectic solidification interface [43] [44], disproving this surface energy mechanism.

It was also found that the mechanisms used to describe Si refinement, via alloy additions, were inadequate to explain the modification caused by an increased cooling rate. The main difference between Si that had been modified via alloys additions, versus Si that had been modified via cooling rate, was that the amount of twinning that was present. In the Si modified by increased cooling rate the amount of twinning was substantially lower than what was seen in the Si modified by alloy additions [45]. Since twinning is an inherent part of the IIT mechanism, its reduced presence suggests that IIT cannot explain how this Si modification occurred.

With respect to categorizing the technical solidification conditions of the lamella → rod transition the most comprehensive work was done by Hosch et al. [35] on an Al-13Si alloy produced via the Bridgman technique. In this work they catalogued the transition of the Si morphology as a function of the growth velocity during directional solidification. By doing so they found that as the growth velocity increased, the eutectic Si would shift from an elongated, lamellar structure to a rod-like and fibrous one. This transition of the Si morphology was found to occur in two stages [35]:

1. The formation of in-plane Si rods, through the breakup of elongated lamella type Si, and,
2. The initiation of out-of-plane Si rod growth from in-plane Si rods.

While these two stages were present the shift between them was found to be gradual, and to occur in overlapping but distinct stages. Figure 2-12 outlines this lamella → rod transition in the Si morphology, as a function of the process growth velocity.

Examining Figure 2-12, elongated Si growth was found to dominate at growth velocities below 100 µm/s. But as the growth velocity increased to 250 µm/s this structure was found to degrade, leaving behind a mixture of skeletal Si plates and Si rods. This transition at 250 µm/s signified the first stage of the lamella → rod transition. At a growth velocity of 500 µm/s, the beginning of the second stage of the transition can be seen, as out-of-plane Si rod growth is observed for the first time. At the largest examined growth velocity, of 950 µm/s, the Si is found to be completely rod-like and fibrous.

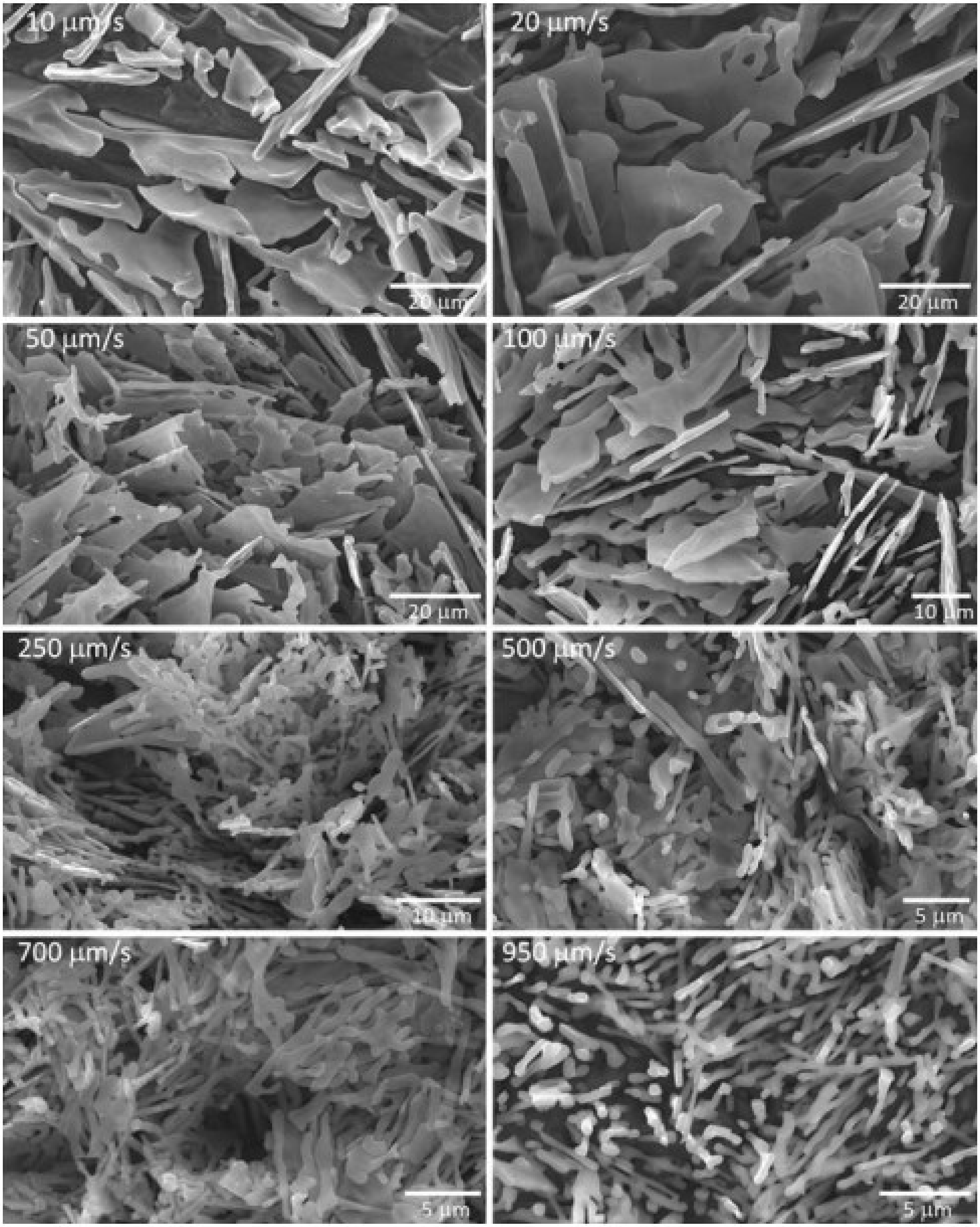

Figure 2-12: Transition in the Si morphology, as a function of growth velocity, for a directionally solidified, deep-etched, Al-13Si alloy *[35]*.

While this work provided a categorization of the lamella → rod transition it only dealt with one alloy composition and was done in terms of the process growth velocity, which noticeably limited the applicability of the work to other Al-Si alloys produced by different processes.

With that said, something that was apparent from this work was that the growth velocity of the solidification front affects the Si morphology that forms. It can therefore be assumed that if one can increase the solidification rate, beyond what was used in the Bridgman technique, more refined Si morphologies should be achieved.

One of the most effective methods to increase the cooling rate is rapid solidification. An example of this Si refinement via rapid solidification is shown below in Figure 2-13, which compares the microstructure of a slow cooled and a rapidly solidified Al-12.5Si alloy. Examining this figure, the size and distribution of the eutectic Si is an order of magnitude finer for the rapidly solidified sample in comparison to the slow cooled sample. Also, the rapidly solidified sample shows the formation of a meta-stable structure, a primary α-Al phase, that would not possible under low undercooling conditions.

Although it has been shown that rapid solidification will refine the eutectic Si phase, how and why it does so is still not understood.

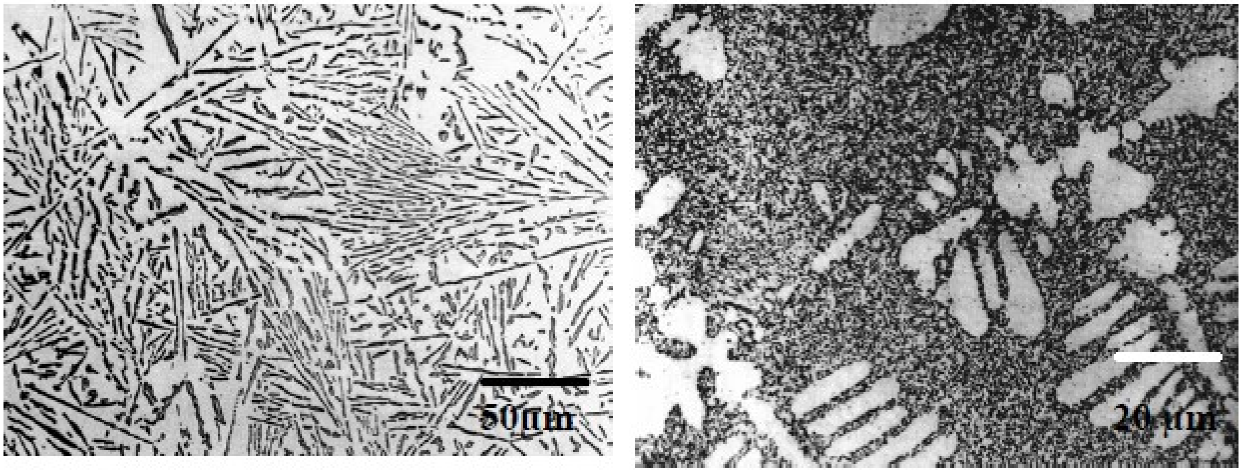

Figure 2-13: Microstructure of an Al-12.5Si alloy that was: (i) Slow cooled via conventional casting, shown in the image on the left. (ii) Rapidly solidified via chill casting, shown in the image on the right. *[6]*.

## 2.7 RAPID SOLIDIFICATION

With rapid solidification being an effective way to modify the eutectic Si phase it has become a noticeable area of interest. However, before understanding how rapid solidification refines the Si phase one must first understand what rapid solidification is.

Our current understanding of rapid solidification is that it relates to a liquid to solid transformation process that has a large driving force during solidification. This definition implies the importance of undercooling, as the driving force will increase the more the melt is undercooled. The ability to undercool a melt depends on the catalytic potency of heterogeneous nucleation sites, along with the nucleation kinetics during solidification [41]. For this reason, there are three different methods that can be used to achieve rapid solidification [41]:

1. Quenching or high rate of heat extraction from the melt,
2. Undercooling of a melt, and
3. A combination of both methods.

The first method, which bypasses heterogeneous nucleation kinetically, is based upon the rapid transfer of heat from a melt. This rapid heat transfer is achieved through the contact of a melt with a substrate or a medium. Now even though this contact can act as a heterogeneous nucleation site, large undercoolings are still achieved as the rate of heat removal is so rapid that the characteristic time for cooling becomes similar to the time required for critically sized nuclei to form [41]. This suppression of nuclei formation undercools the melt and causes there to be a large driving force during solidification. In some cases, this cooling rate is so high that nucleation is kinetically circumvented altogether, leading to an adiabatic type of solidification [46]. The most commonly used process to achieve this type of rapid solidification is quenching (e.g. melt spinning and splat cooling), where cooling rates of $10^6$ K/s can be achieved [41].

The second method, which deals with the limitation of heterogeneous nucleation sites, achieves high undercoolings by limiting the potential for nucleation to occur. To achieve this, a combination of factors can be used including: high purity materials, inert environments during processing, and containerless solidification. By using any or all of these techniques, the ability for nucleation to occur is noticeably suppressed. As a result, the melt undercools, providing a large driving force for solidification. However, unlike the first method this limitation of heterogeneous nucleation sites does not necessarily mean this method will achieve a high cooling rate. For example, the process of Electromagnetic Levitation (EML) only has cooling rates of 1-100 K/s during solidification [41] but still achieves rapid solidification (in portions of the sample) due to the large undercoolings that are reached through the suppression of heterogeneous nucleation sites.

The last method combines rapid heat transfer with the limitation of heterogeneous nucleation sites. The difference between this and the previous two methods is that here rapid solidification occurs prior, during and after solidification. This allows for both high cooling rates and large undercoolings to be achieved. A process that can achieve these conditions are drop-tube experiments. These experiments are inert and containerless, which allows them to reach high cooling rates and undercoolings due to the small size of the formed droplets and due to the large heat extraction capability of the surrounding inert gas.

The use of rapid solidification leads to noticeable deviations from equilibrium and causes the occurrence of many meta-stable effects during solidification. This leads to benefits such as [47]:

1. Large extensions of the solid solubility,
2. Formation of non-equilibrium and meta-stable phases,
3. Reduction in both the number and size of segregated phases, and,
4. The refinement of the microstructural features.

These advantages make rapid solidification a powerful technique that can achieve large improvements in both microstructural refinement and alloy properties.

## 2.8 CONTAINERLESS SOLIDIFICATION

While there are many techniques that can achieve rapid solidification, one of the most effective and efficient methods is containerless solidification. Although containerless solidification will not necessarily achieve high cooling rates, it does allow for large undercoolings to be achieved, which causes there to be a large driving force during solidification [41].

Containerless solidification achieves these large undercoolings through the elimination of crucible and substrate induced nucleation, which noticeably reduces the potential for heterogeneous nucleation within the melt [41].

While there are a wide range of containerless solidification techniques this section will only focus on three of these methods. For each method a quick description will be presented, along with an overview of their advantages and disadvantages with respect to rapid solidification processing.

### 2.8.1 **Electromagnetic Levitation (EML)**

During EML (see Figure 2-14) a metallic droplet is freely suspended and heated via electromagnetic levitation [48]. The principle of this technique is that a small metallic sample can be levitated by Lorentz forces, created by the electromagnetic field [49], while simultaneously being heated by the hysteresis losses as the electromagnetic field alternates directions [48]. This set-up, along with the fact that the process takes place in a high vacuum and inert environment, greatly suppresses heterogeneous nucleation within the droplet, allowing for extremely large undercoolings to be achieved.

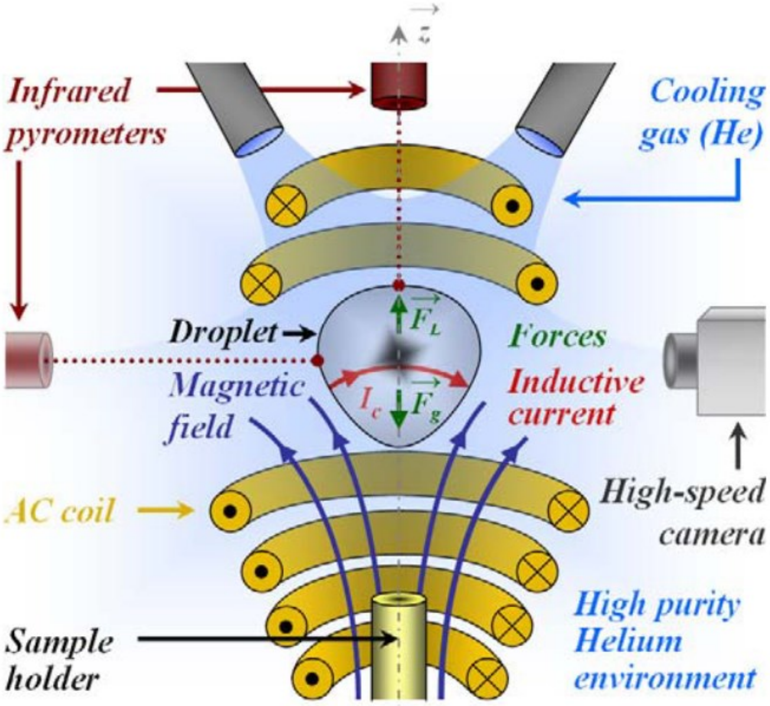

Figure 2-14: Schematic of an electromagnetic levitation apparatus *[50]*.

This technique is sought after as it is a very controllable process that can be monitored in-situ, allowing for direct measurements of the droplet temperature and the growth front to be made during solidification.

However, this technique can only generate one sample at a time and these samples are not large in terms of their volume (~6mm in diameter). As well, there is a noticeable amount of convection within the sample during EML, due to the eddy current and the Lorentz force. This convection makes it difficult to understand how the microstructure solidified, when conducting post-mortem analysis.

### 2.8.2 **Drop-Tube**

The drop-tube technique involves rapid cooling of small molten droplets as they fall containerlessly within a tube [48]. Typically, these tubes are filled with inert gas, to help limit the contaminants that could cause heterogeneous nucleation during solidification.

Initially, during this technique, an alloy is melted in a crucible that has an orifice placed in its bottom. Once an appropriate superheat is achieved for the melt, an overpressure of gas is applied, forcing a stream to be generated out of the orifice. This stream quickly breaks up into droplets that fall under gravity in an inert atmosphere.

Drop-tube allows for high undercoolings to be achieved as it avoids any nucleation at a mold wall or at a substrate during solidification. Large cooling rates can also be achieved due to the small size of the molten droplets and the large heat extraction capabilities of the surrounding inert gas. Another benefit of this technique is that many more droplets can be produced, in comparison to EML, allowing for a statistical analysis on nucleation and crystal growth to be conducted [48].

However, a limitation is that no in-situ measurements can be conducted. As well the magnitude of the undercooling, for drop-tube experiments, is much lower than the undercooling that is achieved during EML experiments.

### 2.8.3 **Gas Atomization**

Gas atomization is a technique that involves the break-up of a melt stream into droplets through interactions with a gas jet.

Similarly, to the drop-tube technique, the initial stage of gas atomization involves the melting of an alloy within a crucible that has an orifice placed in its bottom. Once the appropriate superheat is achieved, an over-pressure of gas is applied, to force the melt out of the orifice as a stream. However, instead of breaking up during free fall, this melt stream gets broken up into many small droplets via interactions with fast-moving gas jets. These gas jets disintegrate the melt stream by creating instabilities within the melt, that form by the shearing action of the gas flow and by the relative gas velocity [51]. After breaking up, the formed droplets will solidify as they fall via heat transfer to the surroundings.

Since gas atomization produces very small particles (<500μm), this leads to rapid heat transfer and extraction during solidification, allowing for large undercoolings and high cooling rates to be achieved.

However, even with this rapid rate of heat extraction the use of gas atomization has some drawbacks. For one it is a very chaotic process where heterogeneous nucleation cannot be controlled, unlike in EML and drop-tube experiments. This potential for heterogeneous nucleation is possible in a variety of ways during gas atomization [47]:

1. Nucleation due to inclusions, undissolved phases and/or crucible debris,
2. Nucleation due to surface oxidation, and,
3. Nucleation due to inter-particle collisions during flight.

Furthermore, the temperature of the atomizing gas will increase significantly during the process, causing the driving force for heat extraction to vary during solidification [52].

These factors, combined with the inability to conduct in-situ measurements, make it difficult to relate changes in microstructure to anything except for the process conditions of gas atomization, limiting the applicability of alloys that were studied using this technique.

## 2.9 IMPULSE ATOMIZATION

In this thesis the examined Al-10wt%Si alloy was produced using the containerless solidification technique of Impulse Atomization (IA). This technique, developed by Dr. Hani Henein at the University of Alberta [53], is a single fluid process that uses mechanical impulses to help breakup a melt stream into droplets. Once broken up these droplets will solidify via heat transfer to the surroundings, as they fall containerlessly within an inert chamber, akin to the drop-tube method. A schematic of the IA set-up is shown below in Figure 2-15.

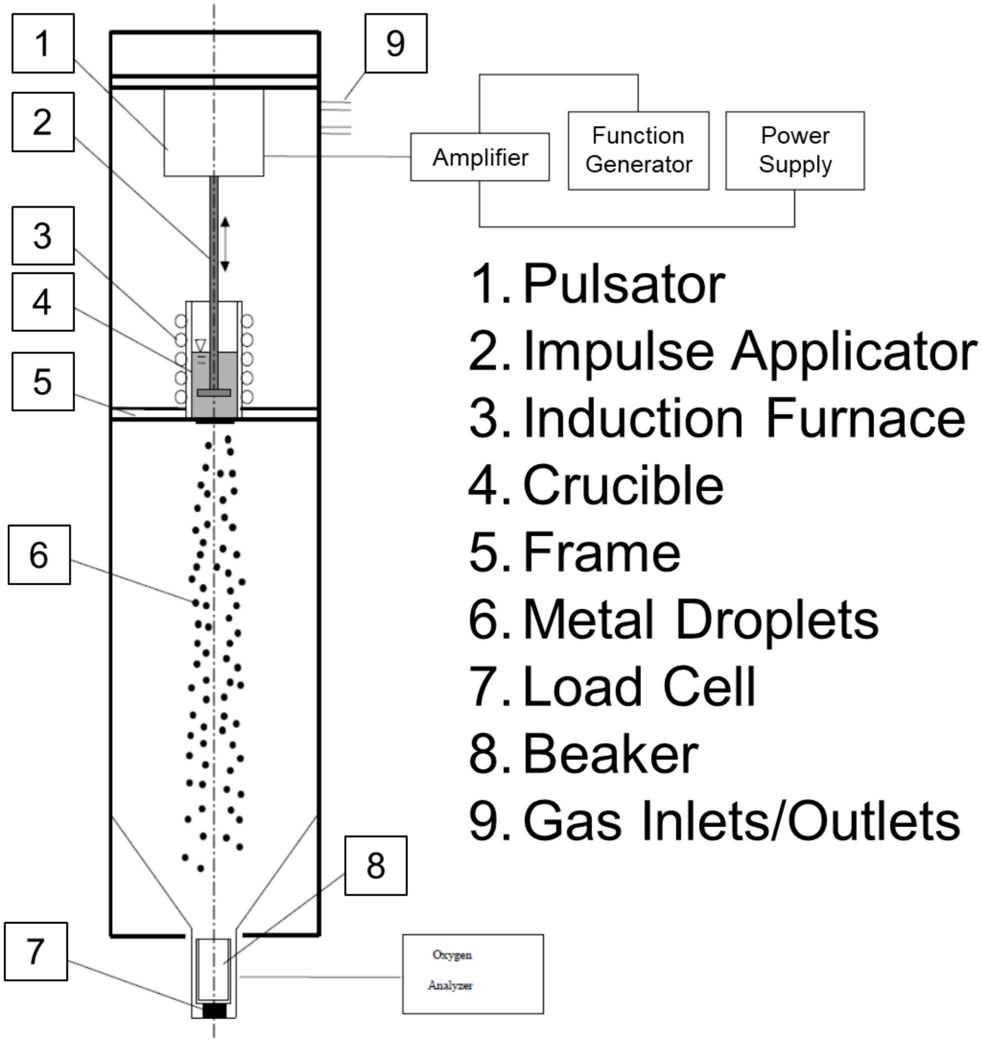

Figure 2-15: Schematic of the Impulse Atomization process *[54]*.

One of the advantages of IA is that heterogeneous nucleation is noticeably reduced, allowing for large undercoolings to be achieved during solidification. As well, unlike gas atomization, the temperature of the surrounding inert gas does not vary, meaning that the driving force for heat extraction will be constant.

These factors allow IA to achieve greater microstructural refinement, in comparison to other atomization processes, and in comparison, to EML experiments (since the droplet sizes are an order of magnitude smaller for IA in comparison to EML). This improved microstructural refinement of IA powders can be seen in Figure 2-16 from work that was done by Henein et al. [55]. In this figure the SDAS of an IA Al-Ni-Fe alloy was shown to be finer than the SDAS of the same alloy that was produced by either gas atomization or by centrifugal atomization.

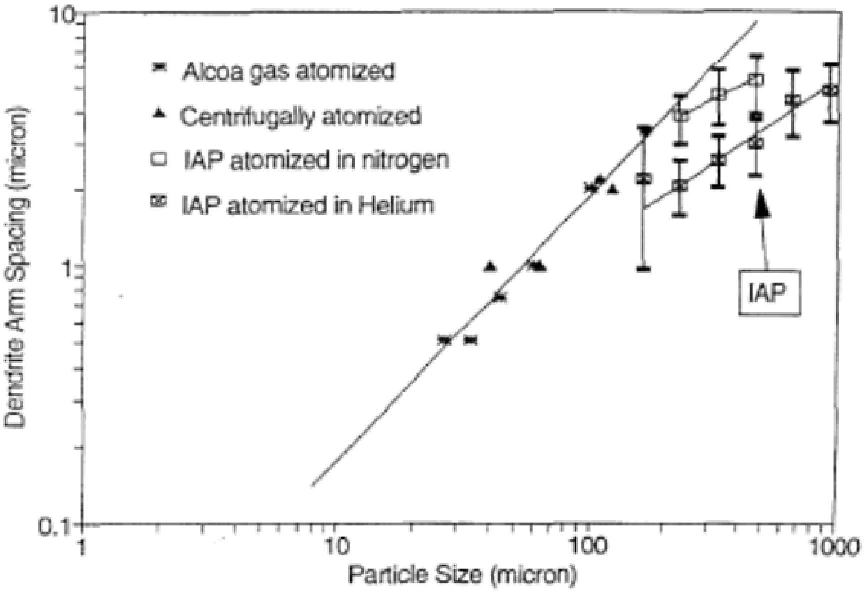

Figure 2-16: SDAS comparison of an Al-Ni-Fe alloy produced by a variety of atomization techniques *[55]*.

Another advantage of using IA, to study rapid solidification, is that convection in the droplet is noticeably limited during solidification. This limited convection makes it easier to understand how the microstructure formed, especially when conducting post-mortem analysis.

Even though IA has these advantages, it biggest weakness is that it is not yet feasible to carry out in-situ measurements to determine the thermal history of an IA droplet. To help solve this issue Wiskel et al. [56] developed a thermal model that could provide a full thermal history of a droplet, produced by IA, using post-mortem analysis. A detailed description of this thermal model can be found in Section 2.10.

These advantages, along with the ability to conduct in-depth examinations, using post-mortem analysis, make IA a very powerful tool that can characterize the solidification path of rapidly solidified alloys.

## 2.10 THERMAL MODEL FOR IMPULSE ATOMIZED DROPLETS

The thermal model, developed by Wiskel et. al [56], describes the transient heat flow that occurs during the solidification of IA droplets and is used to determine its thermal history. To accomplish this, the model expanded on previously developed heat transfer models, for molten metal droplets, moving in a gas stream.

The cornerstone of these previous models was the calculation of the heat exchange between the droplet and the surrounding gas, which can be accomplished by finding the effective heat transfer coefficient ($h_{eff}$). It was then found that an accurate estimation of the $h_{eff}$ was possible, by estimating the Nusselt number, across the entire surface of the droplet.

This estimation of the Nusselt number was typically done using Ranz-Marshall & Whitaker equations [56]. Through a comparison of experimental results and results from the thermal model, Wiskel et al. found that a modified Whitaker correlation (shown below) was the best fit to describe the effective heat transfer coefficient ($h_{eff}$) for an IA droplet [56].

$$Nu = \frac{h_{eff}D}{k_s} = 2\left(\frac{B}{k_s(m+1)}\right)\left(\frac{T_S^{m+1}-T_\infty^{m+1}}{T_S-T_\infty}\right) + \left(0.4Re^{\frac{1}{2}} + 0.06Re^{\frac{2}{3}}\right)Pr^{\frac{1}{4}}\left(\frac{\mu_\infty}{\mu_s}\right)^{\frac{1}{4}} \qquad (2\text{-}3)$$

Where D is the droplet diameter, $k_s$ is the conductivity, $\frac{\mu_\infty}{\mu_s}$ is the ratio between the viscosity at the free stream gas temperature and the viscosity at the droplet surface temperature, $T_\infty$ is the ambient gas temperature, $T_S$ is the temperature of the droplet surface and B & m are constants.

Along with this estimation of the effective heat transfer coefficient ($h_{eff}$) the thermal model had eight assumptions, listed below [56]:

1. Internal temperature gradients within the droplets are negligible,
2. The time for stream break up and spheroidization of ligaments is very small compared to the solidification time,
3. Initial velocity of droplet is 0.5 m/s [57],
4. The ambient gas temperature remains constant during atomization,
5. For radiation heat transfer, a droplet emissivity of 0.1 was used,
6. Thermal interaction between droplets is negligible,
7. Droplet undercooling is not considered, and,
8. Droplet diameter decreases during solidification.

Using these assumptions an estimation of the effective heat transfer coefficient ($h_{eff}$) could be made, allowing for a determination of the thermal history of an IA droplet.

Essentially the solidification of a molten droplet, during IA, involves the transfer of heat between the molten droplet and the surrounding gas. To describe this a governing heat transfer equation was developed:

$$\frac{dT_m}{dt} = -\frac{6h_{eff}}{\rho_m Cp_m D}(T_m - T_\infty) \tag{2-4}$$

Where $\frac{dT_m}{dt}$ is the change in droplet temperature with time, $\rho_m$ is the droplet density, $Cp_m$ is the droplet specific heat, and $T_m$ is the droplet temperature.

Along with this, the thermal model developed an expression to balance the influence of gravity, buoyancy and drag forces on the droplet as it falls. To create this expression a force balance was conducted using Newton's Second Law of Motion for a free-falling body:

$$\frac{dv}{dt} = \frac{\rho_m - \rho_g}{\rho_m} g - 0.75\frac{\rho_g}{\rho_m}\left(\frac{C_d}{D}\right)v^2 \tag{2-5}$$

Where $\frac{dv}{dt}$ is the acceleration, $\rho_g$ is the density of the gas, v is the relative velocity of the droplet to the ambient gas and $C_d$ is the drag coefficient which is calculated from $C_d = \frac{18.5}{Re^{0.6}}$.

The thermal model solved these two equations using a 4th order Runge-Kutta method and was set up as an .exe file.

## 2.11 PREVIOUS WORK ON THE MICROSTRUCTURAL ANALYSIS OF RAPIDLY SOLIDIFIED AL-SI ALLOYS

In this section a review of previous work, regarding the microstructural analysis of rapidly solidified Al-Si alloys, is presented. Due to the limited amount of work that has been done in this area, the results of each paper were presented and summarized as separate sub-sections.

### 2.11.1 **The Coupled Zone of Rapidly Solidified Al-Si Alloys**

Work by Pierantoni et al. [58] examined the influence of rapid solidification on Al-Si alloys (15.5 to 26 wt.% Si) produced by laser re-solidification. The aim of this work was to characterize the Al-rich boundary of the coupled eutectic zone, and was carried out using experimental results, in addition to theoretical results from a competitive growth model. Through this characterization the

Al-rich boundary of the coupled eutectic zone was found and plotted as a function of the growth rate (Figure 2-17) and as a function of the temperature (Figure 2-18).

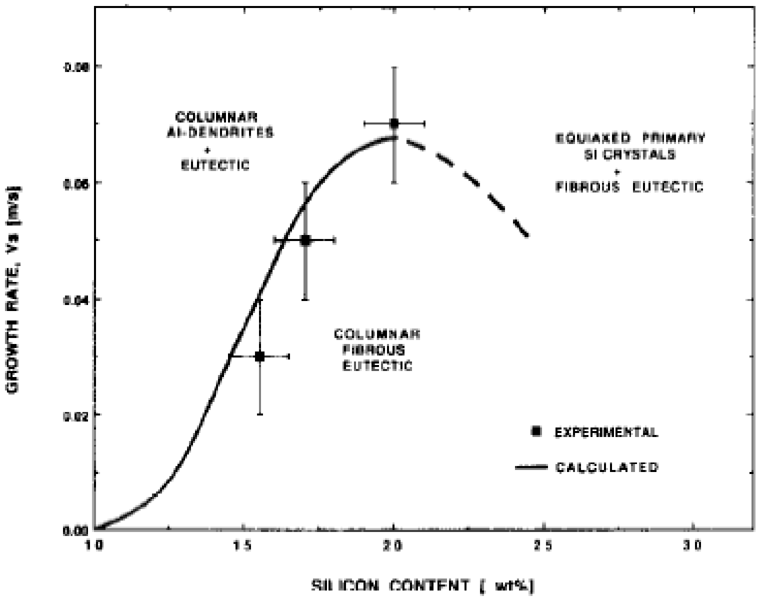

Figure 2-17: Al-rich boundary of the coupled eutectic zone plotted as a function of the Si content and the growth rate. *[58]*.

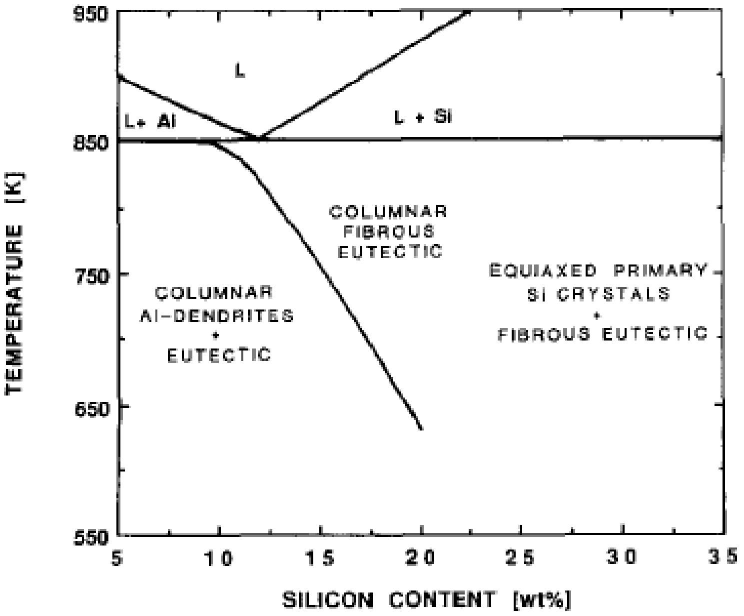

Figure 2-18: Al-rich boundary of the coupled eutectic zone super-imposed onto the Al-Si equilibrium phase diagram *[58]*.

While this work focused on determining the Al-rich boundary of the eutectic coupled zone, it also provided a mapping of the overall Al-Si microstructure as a function of various solidification conditions.

### 2.11.2 Microstructure of Rapidly Solidified Al-6Si Submicron Powders

In the work by Levi and Mehrabian [46] they examined the microstructure of micron and submicron Al-6Si alloy powders produced by electrohydrodynamic (EHD) atomization. Here it was found that decreasing the particle size would induce super-saturation within the powder, and lead to the formation of a homogenous microstructure. They also found that an increase in the undercooling, due to a decrease in the particle size, promoted the occurrence of multiple nucleation events and twinning within the sub-micron powders.

### 2.11.3 Microstructural Development in Hypereutectic Al-Si alloys Produced by Gas Atomization

Work by Genau [59], in her MSc thesis, examined the influence of rapid solidification on two hypereutectic Al-Si alloys (15 & 18 wt.% Si), produced by gas atomization. From this analysis two types of microstructures were observed:

1. A microstructure comprised of a cellular α-Al phase and an Al + Si eutectic structure.
2. A microstructure comprised of a pure coupled Al + Si eutectic structure.

Both microstructures showcased noticeable deviations from equilibrium, as these were not the typical microstructures that are seen for hypereutectic Al-Si alloys.

Beyond the morphology, it was found that a decrease in the particle size noticeably refined the scale of the microstructure, and that below a certain particle size (>11µm) a completely adiabatic type of solidification was found to occur.

### 2.11.4 Dynamical Evolution in the Microstructure of Finely Atomized Eutectic Al-Si alloys

Work by Trivedi et al. [60] conducted a quantitative examination of an Al-12.6Si alloy produced by gas atomization. Here they found that the microstructure of an Al-12.6Si alloy would transition from eutectic → dendritic → microcellular as the particle size decreased. Using these results, they created a microstructure-processing map for the Al-Si system, that related the fraction of a specific morphology, to a specific composition and a specific undercooling. This microstructure-processing map can be seen in Figure 2-19.

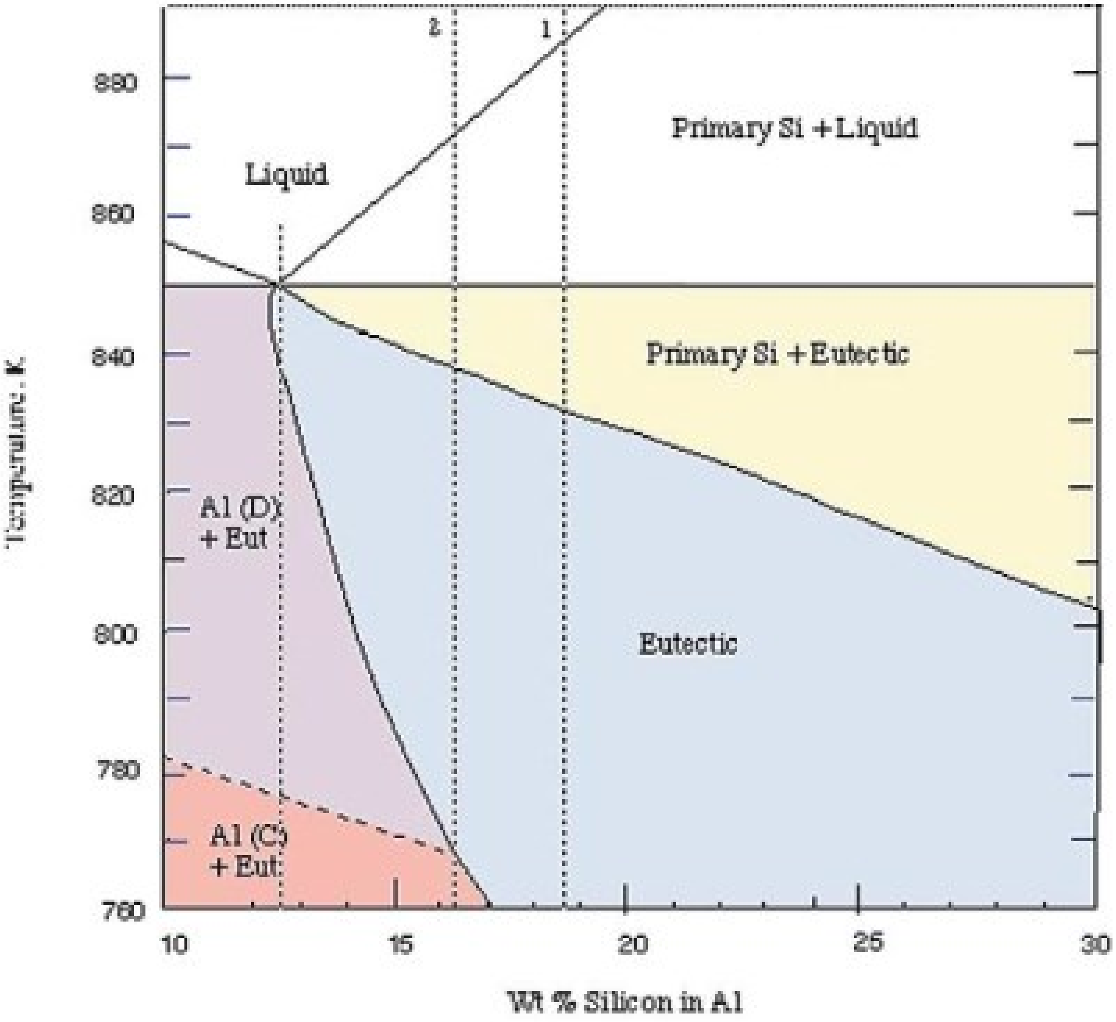

Figure 2-19: Microstructure-Processing map for the Al-Si system *[60]*.

### 2.11.5 **Hypereutectic Al-Si Powders Solidified under Far-From Equilibrium Conditions**

Work by Kalay et al. [61] expanded on the previously developed Al-Si microstructure-processing map [60], by examining more Al-Si alloy compositions (15, 18, 25 and 50 wt.%Si). Just as before they found that the morphology of the microstructure would shift from eutectic → dendritic → cellular → microcellular as the particle size decreased. This updated Al-Si microstructure-processing map can be seen in Figure 2-20.

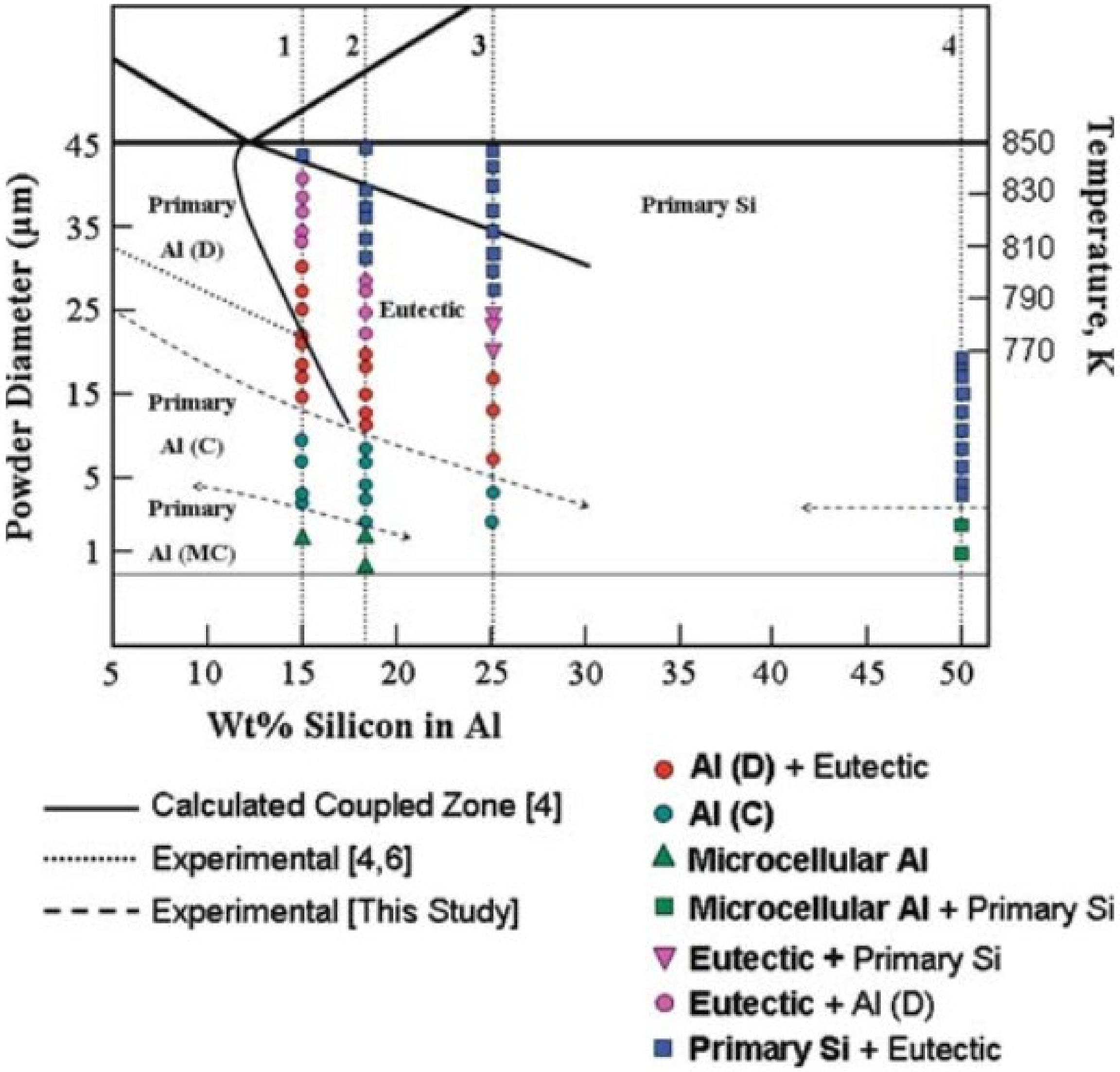

Figure 2-20: Extension of the Al-Si Microstructure-Processing map by Kalay et al. *[61]*.

### 2.11.6 **Effect of H2 Bubbling on the Rapid Solidification of an Al-5Si Alloy produced by IA**

Work by Brunner [62] focused on the influence of hydrogen bubbling on an Al-5Si alloy produced by Impulse Atomization (IA). This work found that during IA it was possible to achieve large undercoolings (~32K) and high cooling rates during processing.

In terms of microstructural refinement, of the Al-5Si alloy, it was found that the higher cooling rates led to greater refinement of the α-Al spacing, as well as greater refinement of the eutectic Si phase. As for the influence of hydrogen bubbling it was found to affect the eutectic fraction within the alloy but it did not seem affect the refinement of the eutectic Si interphase spacing.

## 2.12 REMAINING KNOWLEDGE GAPS & RESEARCH OBJECTIVES

While this literature review highlighted some of the work that has been done regarding the rapid solidification of Al-Si alloys it also showed that our understanding of the topic is still limited.

One of the issues with the examined past work was that it dealt with alloys that were produced by gas atomization. This meant that shifts in the microstructure had to be related to the process conditions of gas atomization, instead of being related to a technical cooling rate or some universal solidification condition. Making it difficult to extend this work, on the gas atomization of Al-Si alloys, to work that used different rapid solidification techniques.

Another aspect that is missing from past work is a detailed examination of how rapid solidification influenced the eutectic Si morphology. Although it is known that controlling this Si morphology is important, there was no in-depth work that focused on how, where or why this Si modification occurred, during rapid solidification.

From these various knowledge gaps three main research objectives were identified and used to formulate the scientific objectives of this thesis work, which dealt with the rapid solidification of an Al-10Si alloy:

1. An understanding of how rapid solidification influences the morphology of both the primary α-Al phase and the secondary Al + Si eutectic structure,
2. A quantification of the lamella → rod Si growth transition, during refinement, as a function of specific solidification conditions, and,
3. A relationship between the changes in the microstructure and the mechanical properties of the Al-10Si alloy.

# 3 EXPERIMENTAL PROCEDURE

In this chapter the experimental procedure for the analysis of the impulse atomized Al-10Si alloy will be outlined. This will include a description of the various characterization techniques, alloying materials, and processing conditions that were used.

## 3.1 MATERIALS & ALLOY PURITY

For the Al-10Si alloy, commercial purity Al (99.9%) and high purity Si (99.999%) was used. With the specific impurities of the commercial purity Al being listed in Table 3-1 below.

Table 3-1: Composition of the commercial purity aluminum provided by Alfa Aesar.

| **Element** | **Al** | **Si** | **Fe** | **Zn** | **Ga** |
|---|---|---|---|---|---|
| **Wt. %** | 99.9 | 0.014 | 0.048 | 0.017 | 0.005 |

Impurities, like Fe, can noticeably influence how the Al-Si alloy solidifies, even in trace amounts. So, the produced IA Al-10Si alloy was sent off for chemical analysis to determine its final Fe content. From this analysis the Fe content was 0.07wt% with the alloy. The full results of the chemical analysis can be found in Appendix A.

## 3.2 IMPULSE ATOMIZATION RUN CONDITIONS

In this work the examined Al-10Si alloy was produced using Impulse Atomization (IA), with two separate IA runs being conducted. The first run used helium gas (pre-purified 99.995%), a nozzle plate with 37 orifices, and an orifice size of 300µm. While the second run used argon gas (pre-purified 99.998%), a nozzle plate with 37 orifices, and an orifice size of 100 µm. A full list of the experimental conditions used during each IA run, can be found in Table 3-2.

For the heating and atomization of the Al-10Si alloy the oxygen content within the atomizer was kept below 10ppm. To achieve this oxygen content the atomization chamber was first pulled to a vacuum and then filled with inert gas. Once the chamber had been filled, continuous purging and gas feeding occurred until the desired oxygen content was achieved. This oxygen content could then be maintained as long as there was a positive pressure within the chamber.

Table 3-2: Al-10Si alloy IA run conditions.

| Run # | Atomization Gas | Orifice Size | # of Orifices | Superheat Temperature |
|---|---|---|---|---|
| 081516 | Helium | 300µm | 37 | 170°C |
| 160926 | Argon | 100µm | 37 | 170°C |

## 3.3 POWDER ANALYSIS

In this section the stages of powder analysis, for the IA Al-10Si alloy, is presented.

### 3.3.1 Powder Collection & Cleaning

Powders, produced by IA, were collected in a Pyrex beaker located at the bottom of the atomizer. This beaker contained high temperature oil and was meant to quench any large drips or powders that may have extraneously formed (due to inadvertent crucible wetting) during IA. However, this oil can also act as a surface contaminant, so prior to being analyzed the powders had to be cleaned.

The first stage of cleaning involved mixing for 2 to 3 minutes with toluene; where the used toluene was poured out as waste and new toluene was added. This process was repeated until the toluene being poured out was clear, indicating that no residual oil was present. After this, ethyl alcohol was added to help remove any residual toluene. Again, this mixture was shaken for 2 to 3 minutes and was repeated until the alcohol being poured out was clear. Once completed the remaining alcohol + powder mixture was drained using filter paper and left to air dry in a fume hood for 24 hours; allowing for any residual alcohol to evaporate.

### 3.3.2 Sieving

The collected powders were sieved using a W.S Tyler Sound Enclosure 6027 automatic sieving machine. The sieve selection for each atomization run was dependent on the orifice size of the nozzle, as this affected the particle size distribution.

For the #081516 run the screens were: <212 µm, 212-250 µm, 250-300 µm, 300-355 µm, 355-423 µm, 423-500 µm, 500-610 µm. 600-710 µm, 710-850 µm, 850-1000 µm and 1000-1180 µm. For the #160926 run the screens were: 75-90 µm, 90-105 µm, 105-125 µm, 125-150 µm, 150-180 µm, 180-212 µm, 212-250 µm, 250-300 µm, 300-355 µm, 355-423 µm, & 423-500 µm.

Once the powders had been sieved they were collected, labeled and stored into vials.

### 3.3.3 **Examined Particle Size Ranges**

From each IA run only six particle size ranges were selected for analysis, as this was found to adequately describe the size-distribution.

For the helium atomization run (#081516) the particle size ranges were: 212-250 µm, 300-355 µm, 355-423 µm, 423-500 µm, 850-1000 µm and 1000-1180 µm. For the argon atomization run (#160926) the particle size ranges were: 125-150 µm, 150-180 µm, 212-250 µm, 300-355 µm, 355-423 µm, and 423-500 µm.

### 3.3.4 **Criterion for Powders Chosen for Analysis**

For a specific powder to be selected for analysis the following two criteria had to be met:

1. The powder could not have been quenched in the oil bath, and,
2. The powder could not have had any inter-particle collisions.

To ensure that the first criterion was met a visual analysis of the microstructure was conducted. If the powder was quenched in the oil bath a clear two-region eutectic microstructure would be visible. So, it was said that if this structure was not seen then it meant that the powder had solidified during free-fall. To help visualize this an example of an IA Al-Si alloy powder, that had been partially quenched, is shown in Figure 3-1 from the work of Brunner [62].

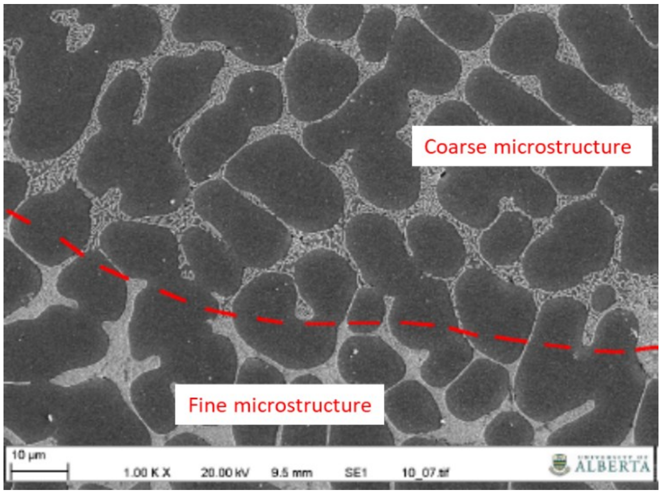

Figure 3-1: Microstructure of a partially quenched Al-5Si alloy produced by IA. The top region of the image, with the coarse microstructure, relates to the portion of the powder that solidified during free-fall. The bottom region of the image, with the fine microstructure, relates to the portion of the powder that was quenched in the oil bath. *[62]*.

Along with this visual analysis the thermal model, developed by Wiskel et al. [56], was used to calculate the required solidification distance for the coarsest particle size examined of each IA run. In both cases it was found that the powder would have fully solidified before it reached the oil bath (which was located ~4m below the crucible).

For the second criterion a visual analysis was used. Due to the controlled nature of IA the amount of inter-particle collisions is limited, and any collisions that did occur are easily spotted during visual analysis. An example of powders with inter-particle collisions can be found in Figure 3-2.

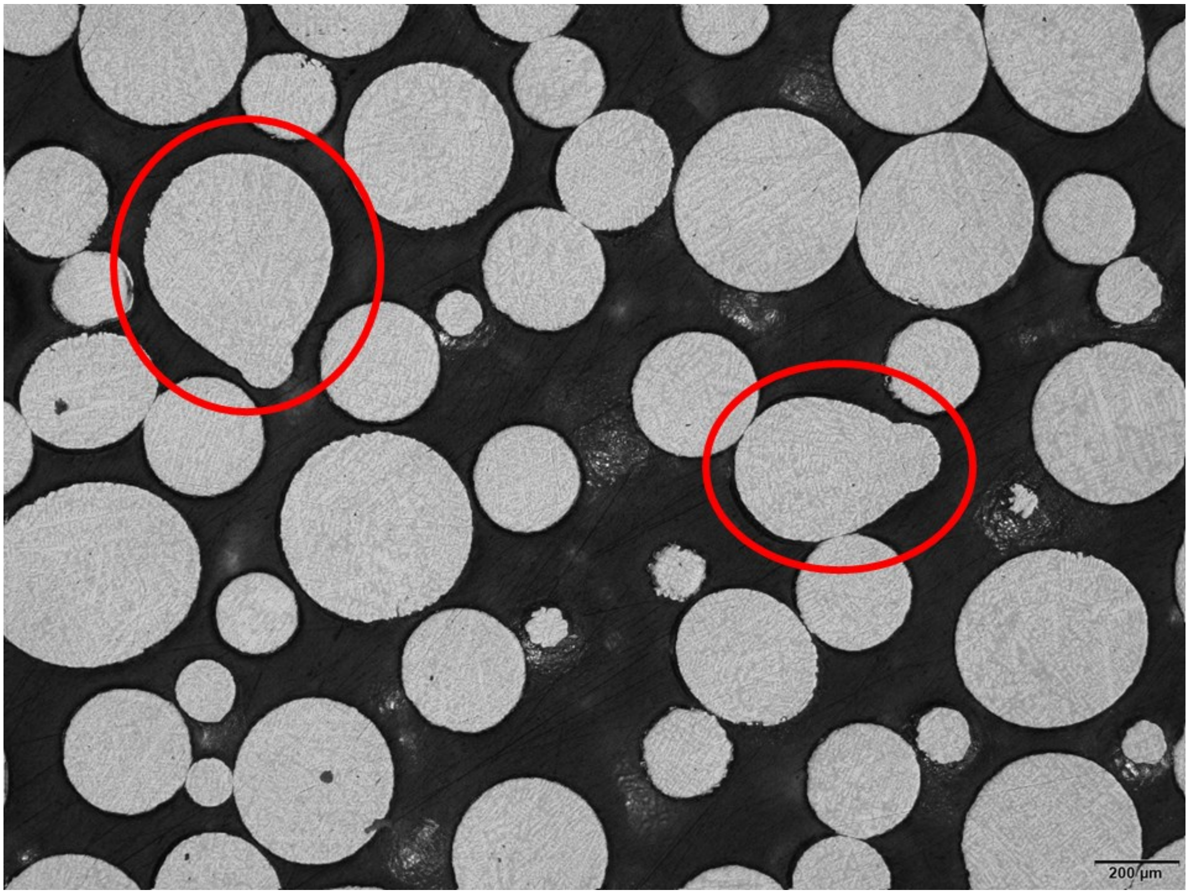

Figure 3-2: Example of Al-10Si powders that had inter-particle conditions. He 212-250µm sample.

## 3.4 METALLOGRAPHY

This section outlines the preparation and analysis techniques that were used to perform metallography on the IA Al-10Si alloy.

### 3.4.1 **Mounting, Grinding & Polishing**

To examine the microstructure of the Al-10Si alloy mounting, grinding and polishing was conducted. Initially the samples were cold mounted, in a mold, using West System 105 epoxy resin and West System 205 hardener. Once the resin had set, the samples were removed from the mold and ground/polished using a Buehler Automet 250 Auto-Polisher. The grinding and polishing procedure that was used is listed below in Table 3-3. Where ">>" relates to the rotation of the platen and the specimen holder in the same direction and "><" relates to the rotation of the platen and the specimen holder in the opposite direction.

Table 3-3: Grinding and polishing procedure used for IA Al-10Si alloy.

| Abrasive Size | Load (N) | Base Speed (RPM) | Relative Rotation | Time |
|---|---|---|---|---|
| ***400 Grit*** | 22 | 240 | >> | Until Plane |
| ***600 Grit*** | 22 | 240 | >< | 2 min |
| ***800 Grit*** | 22 | 240 | >< | 3 min |
| ***1200 Grit*** | 22 | 240 | >> | 4 min |
| ***6 µm*** | 22 | 150 | >< | 6 min |
| ***3 µm*** | 22 | 120 | >> | 3 min |
| ***1 µm*** | 22 | 120 | >> | 2 min |

After polishing the samples were cleaned using water, to remove any residual polishing suspension, and then dried using compressed air.

### 3.4.2 **Etching**

Due to their similarity in atomic mass the contrast between the Al and Si phases can be somewhat limited during microscopy analysis. As such, chemical etching was conducted to aid in the differentiation between the two phases. During this etching samples were subjected to Keller's Reagent (2.59wt% Nitric Acid, 0.64wt% HCl, 0.55% HF, 96.22wt% Water), for 20 to 25 seconds, at room temperature. After this these samples were cleaned with alcohol and water before being dried using compressed air. This etching process, using Keller's Reagent, greatly improved the visual contrast between the Al and Si phases. An example of this improved contrast, of the etched sample, is shown in Figure 3-3.

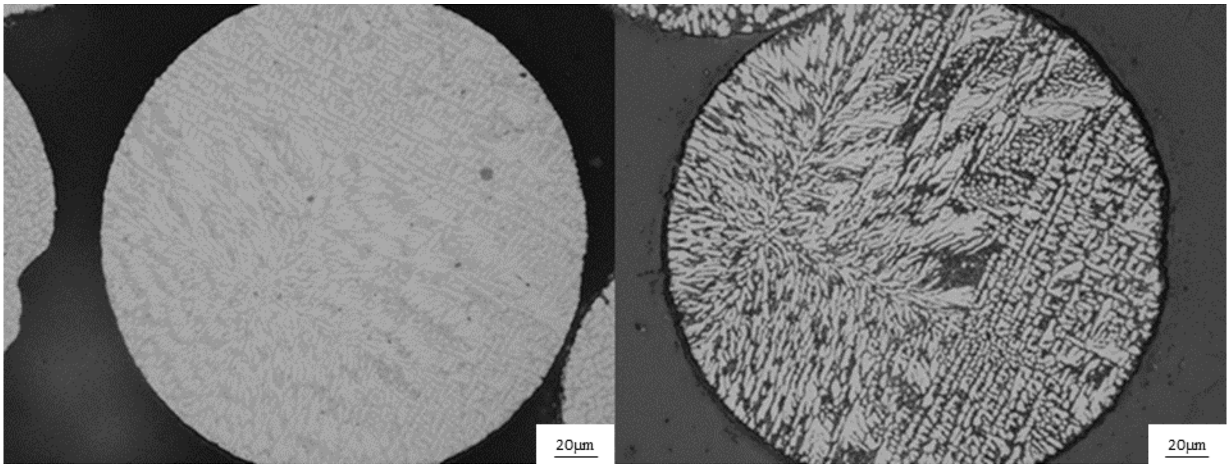

Figure 3-3: OM image showing the influence of Keller's Reagent. He 212-250µm sample.

### 3.4.3 **Deep Etching**

To analyze the 3D eutectic Si morphology deep etching was conducted to dissolve the surrounding Al. To conduct this deep etching a 3-step process was used. The first step involved chemical etching, through the immersion of a polished sample in a HCl solution (3N), for 45-60 seconds, at room temperature. The second step involved placing the sample in a water bath for 30 seconds. And the final step involved lightly spraying the sample with distilled water and then drying it with a gentle flow of compressed air.

### 3.4.4 **Optical Microscopy (OM)**

To analyze the macro-scale features of the microstructure, analysis of the prepared samples was conducted using an Olympus BX61 Optical Microscope, at magnifications of 50x, 100x, 250x and 500x. The analysis, using this optical microscope, focused on the morphology and spacing of the primary α-Al phase, along with measuring the eutectic fraction of the alloy.

### 3.4.5 **Scanning Electron Microscopy (SEM)**

To analyze the nano-scale aspects of the microstructure, analysis was conducted using a Zeiss Sigma 300 VP-Field Emission Scanning Electron Microscope (FE-SEM). During operation this FE-SEM was running at 10kv and dealt with magnifications between 2,000x to 15,000x. The analysis using the FE-SEM was focused on the morphology and the interphase spacing of the eutectic Si phase.

To prepare samples for SEM imaging a carbon coating was deposited onto the sample surface using a Leica EM SCD005 evaporative carbon coater. As well, conductive tape was placed around the top and bottom of the samples prior to any SEM imaging.

### 3.4.6 **Electron Backscatter Diffraction (EBSD)**

EBSD analysis was conducted using a Zeiss Sigma FE-SEM that was equipped with an HKL system. During operation this FE-SEM was running at 20 kV and dealt with magnification up to 5,000x. This EBSD analysis focused on determining the orientation, texture and growth of the primary α-Al phase.

To prepare samples for EBSD analysis a carbon coating was deposited onto the sample surface using a Leica EM SCD005 evaporative carbon coater. As well, conductive tape was placed around the top and bottom of the samples prior to any EBSD analysis.

### 3.4.7 **X-Ray Diffraction (XRD)**

XRD characterization was conducted using a Rigaku Powder X-Ray diffractometer, that used a Co/K-alpha1 tube. During operation the X-Ray diffractometer used a voltage of 38kV, a current of 38mA, and a wavelength of 1.78899Å. This analysis concentrated on determining the crystallographic texture of the Al-10Si alloy.

## 3.5 MICROSTRUCTURE CHARACTERIZATION AND MECHANICAL PROPERTY ANALYSIS

This section outlines the techniques that were used to characterize the microstructural refinement and the mechanical properties of the IA Al-10Si alloy.

### 3.5.1 **α-Al Dendrite Cell Size Measurement**

To quantify the refinement of the primary α-Al phase, the interphase spacing of the α-Al was measured using a "dendrite cell size" definition, shown in Figure 3-4. This "dendrite cell size" refers to the spacing between the centerlines of adjacent dendrite cells [63]. This definition was more reliable than using the secondary dendrite arm spacing as it is difficult to determine whether a dendrite is a secondary arm in these IA powders. This difficulty during analysis is due to the very fine size of the microstructure and its complex three-dimensional network.

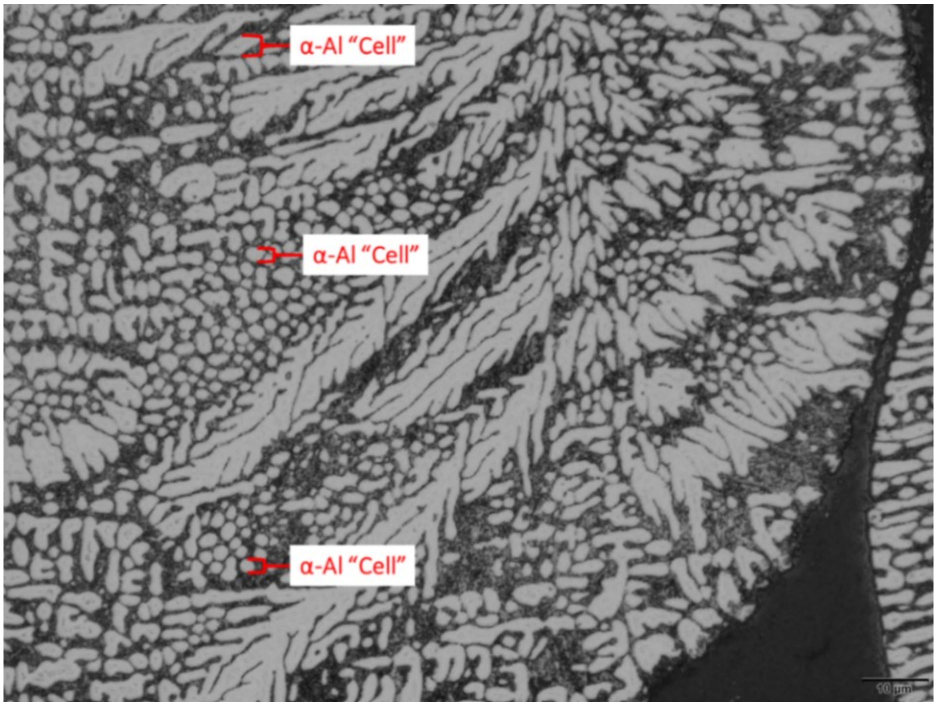

Figure 3-4: OM image showing an example of α-Al "dendrite cell". He 212-250μm sample.

These measurements of the α-Al dendrite cell spacing were conducted using ImageJ software via the linear intercept method. A schematic example of these measurements is found in Figure 3-5. For each particle size 10 to 14 powders were examined, with 5 to 7 measurements being conducted for each powder.

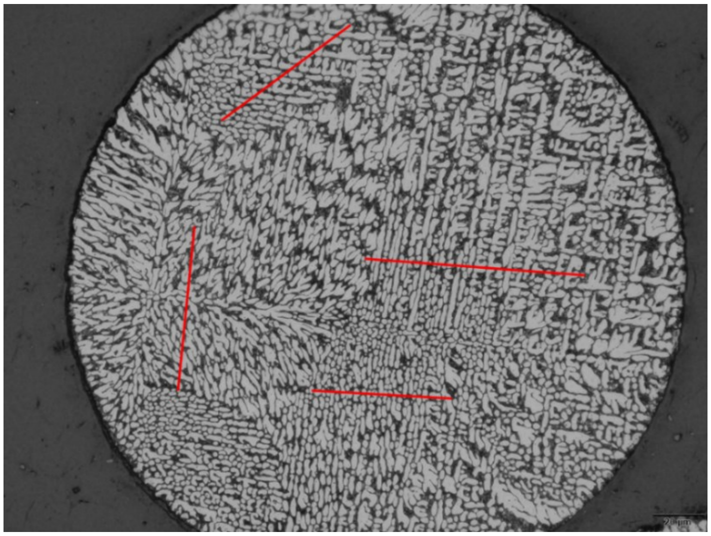

Figure 3-5: OM image outlining the linear intercept measurements used to measure the α-Al "dendrite cell size". He 212-250μm sample.

### 3.5.2 **Eutectic Si Spacing Measurement**

To quantify the refinement of the eutectic structure, eutectic Si spacing measurements were carried out via the linear intercept method using ImageJ software. For each particle size 4 to 6 powders were examined, with 10 to 12 spacing measurements being conducted for each powder. A schematic example of these eutectic Si spacing measurements can be found in Figure 3-6.

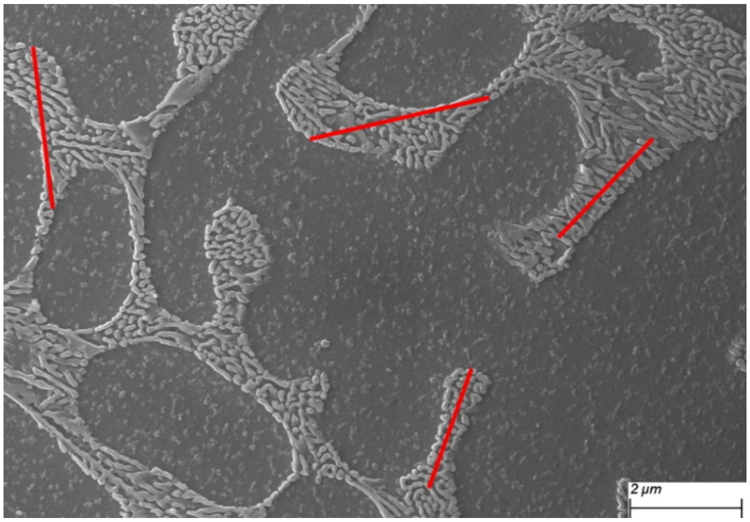

Figure 3-6: FE-SEM image outlining the linear intercept measurements used to measure the eutectic Si spacing. He 212-250μm sample.

### 3.5.3 **Vickers Hardness Measurement**

Vickers hardness measurements were conducted using a Buhler VH 3100 microhardness machine, to determine the bulk hardness of the Al-10Si alloy. The reason why only the bulk hardness could be measured was that the available diamond of the indenter was not fine enough to measure the hardness of specific features. For each particle size 30 to 40 hardness measurements were conducted, with an example of these hardness measurements being shown in Figure 3-7.

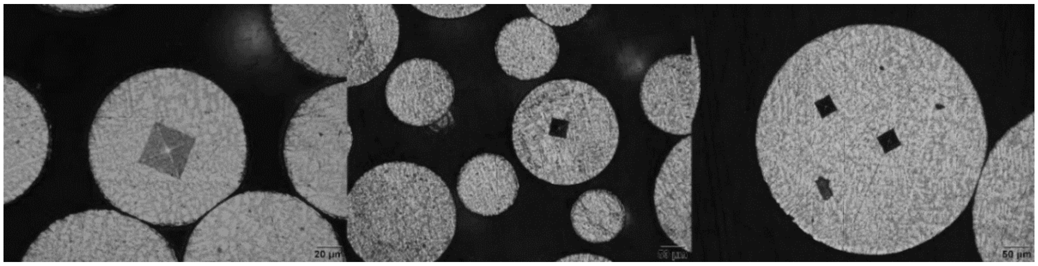

Figure 3-7: OM images showing examples of Vickers micro-hardness indentations.

The microhardness indentations were carried out at a load of 0.2N and a dwell time of 10 seconds. This load was chosen at it was the biggest load that did not have an indentation area larger than the area of the smallest particle size. This load was kept constant for all measurements as it was found that changing the applied load could vary the measured value of the Vickers hardness. This variation of the Vickers hardness, as a function of the applied load, is shown in Figure 3-8.

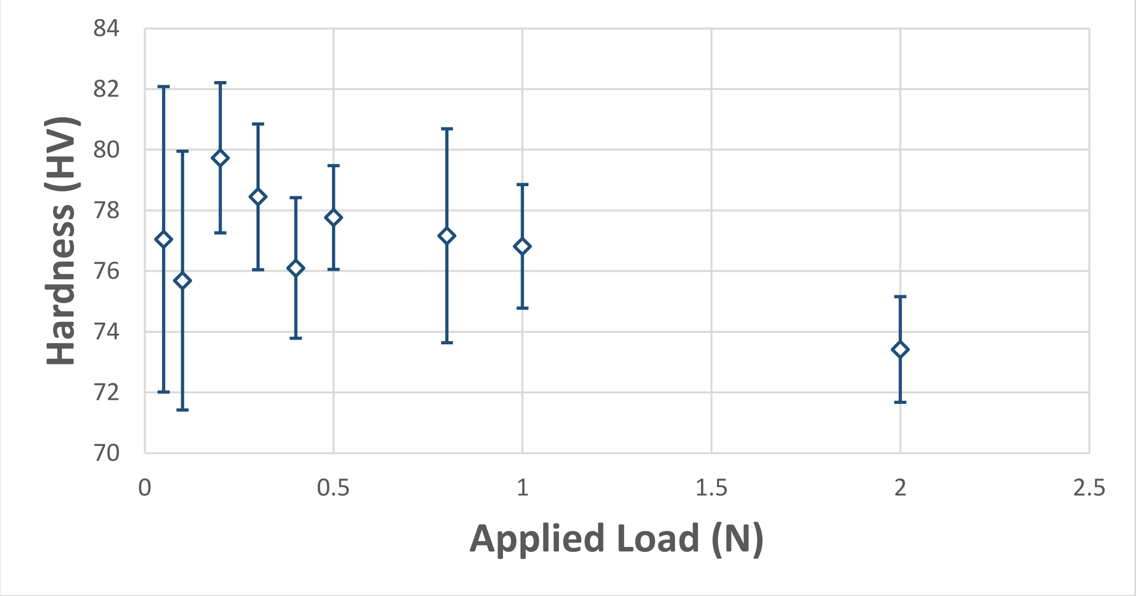

Figure 3-8: Measured Vickers hardness as a function of the applied load. He 212-250µm sample.

# 4 DISCUSSION & RESULTS

## 4.1 AL-10SI MICROSTRUCTURE CHARACTERISTICS

To characterize the influence of rapid solidification on the Al-10Si alloy the microstructure had to be examined. This examination of the microstructure involved a determination of the phases and the components that were present, along with a determination of how they were distributed. The results of this analysis will be presented in this section.

### 4.1.1 **Typical Microstructure**

The first aspect to be examined was the microstructure of the Al-10Si alloy, with typical microstructures being shown in Figure 4-1 and Figure 4-2. Figure 4-1 shows an Al-10Si alloy that was atomized in helium, and Figure 4-2 shows an Al-10Si alloy that was atomized in argon. While the processing conditions of the two samples was different (due to the higher heat removal afforded by helium vs. argon), the inherent phases, and overall structure was still similar.

The isolated dark regions are the primary α-Al phase, while the lighter regions are the eutectic Si phase. The darker regions located between the Si phase, shown in the magnified images of Figure 4-1 and Figure 4-2, are the eutectic Al, which has the same structure (and near identical composition) as the α-Al dendrites.

From this visual examination both microstructures displayed a primary α-Al phase and a secondary Al + Si eutectic structure. This two-part microstructure is typical of hypoeutectic Al-Si alloys and follows the expected path of an Al-10Si alloy under the Microstructure-Processing map that was developed by Trivedi and Kalay [60] [61].

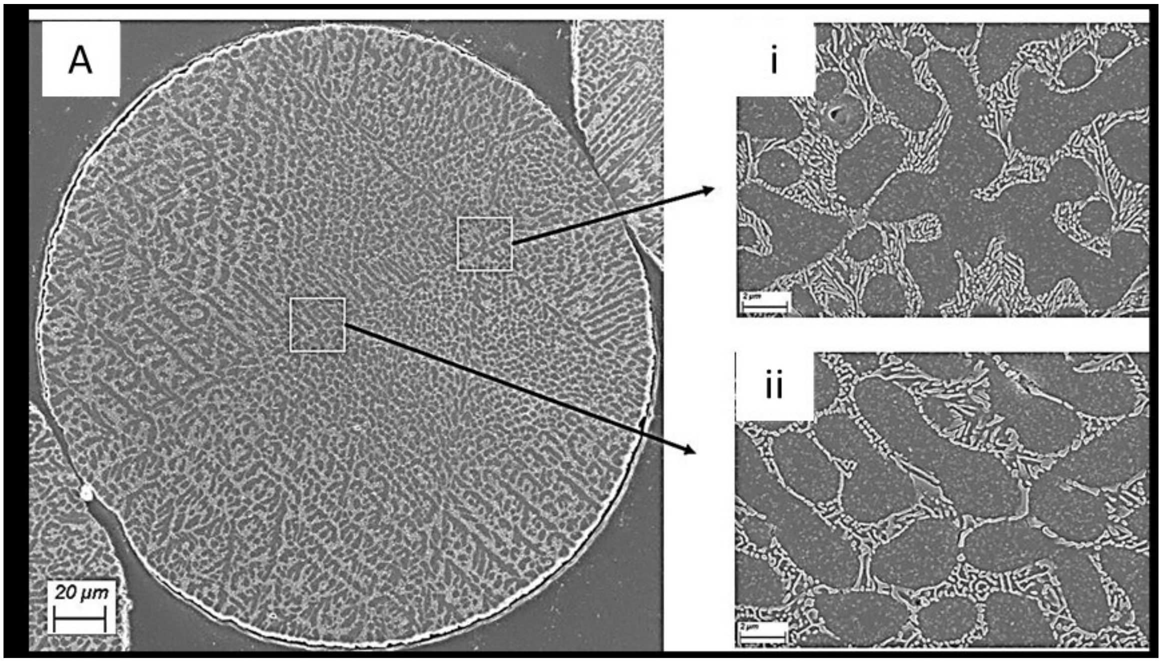

Figure 4-1: OM image of the typical microstructure of an IA Al-10Si powder that solidified in helium (He 212-250). Images i & ii show a greater magnification of the microstructure to highlight the eutectic structure *[64]*.

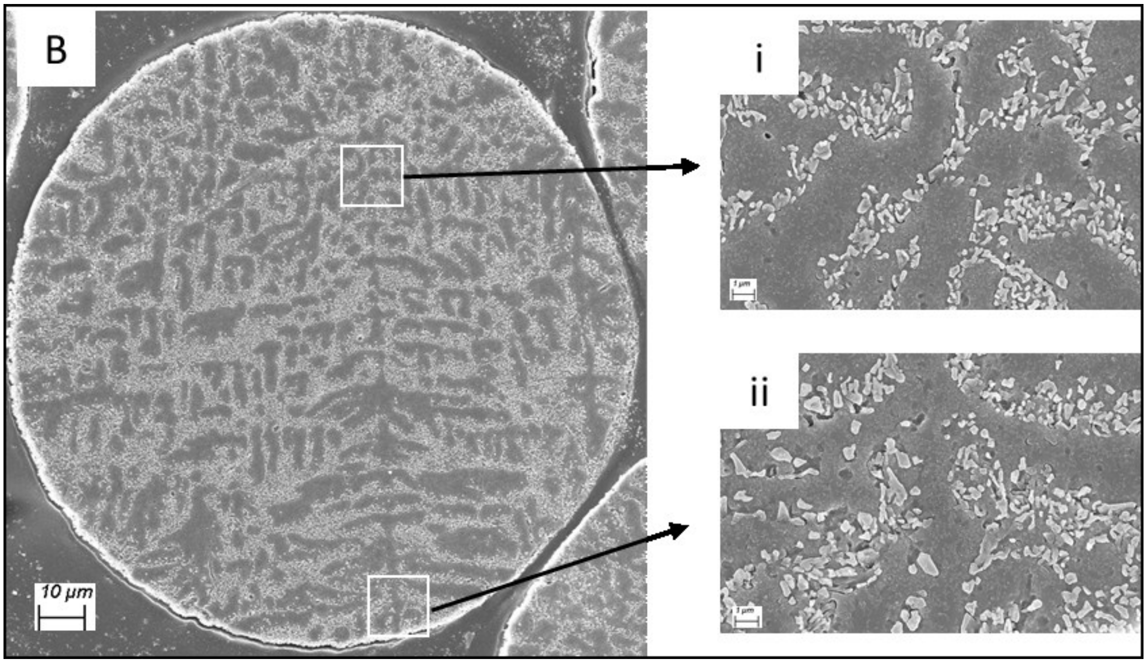

Figure 4-2: OM image of the typical microstructure of an IA Al-10Si powder that solidified in argon (Ar 125-150). Images i & ii show a greater magnification of the microstructure to highlight the eutectic structure.

To confirm this finding the Al-10Si alloy was analyzed via XRD analysis. From these XRD results, see Figure 4-3, pattern indexing established a solid solution Al phase and a Si phase. This confirmed that the major microstructural components were the α-Al phase and the Al + Si eutectic structure. The XRD analysis did not find the presence of any other phases or structures, beyond the two mentioned microstructural components.

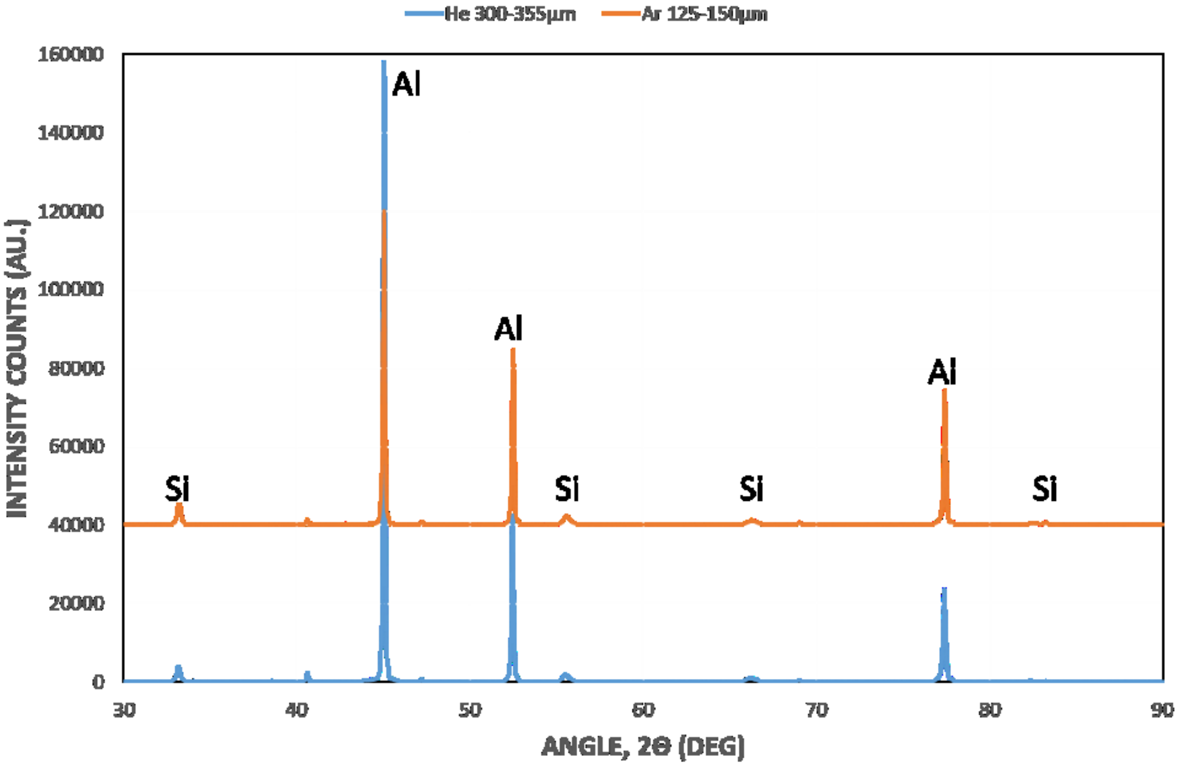

Figure 4-3: XRD patterns of the IA Al-10Si powders.

### 4.1.2 **Eutectic Fraction**

With the microstructure characterized, further analysis was conducted to determine the amount of each component within the alloy, which was done by measuring the eutectic fraction. To conduct this measurement a combination of optical images and ImageJ software was used. Initially the desired optical image of the Al-10Si alloy was cropped and converted into a binary form. This conversion, shown in Figure 4-4, was meant to visually separate the α-Al phase and the Al + Si eutectic structure.

In a binary form the eutectic area fraction could be measured using the ImageJ software and then converted into an eutectic weight fraction. The used methodology to convert the area fraction into the weight fraction is explained in greater detail in Appendix B.

These eutectic fraction measurements were conducted for all examined particle size ranges, with 12 to 15 measurements being conducted at each size range.

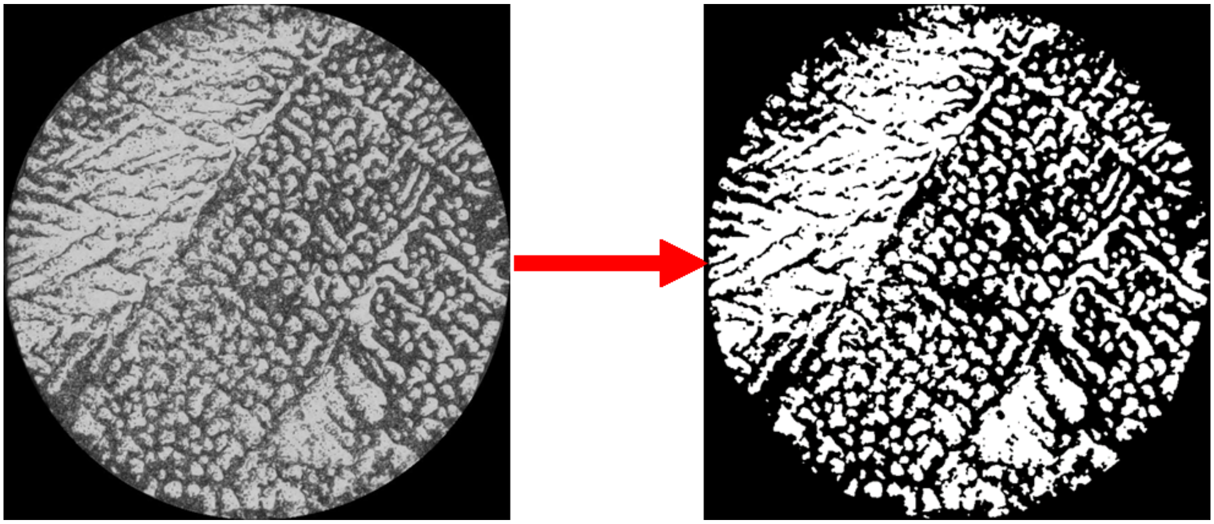

Figure 4-4: OM image showing the cropping and binary image conversion that was used to measure the eutectic fraction. Ar 125-150 sample.

Along with the experimentally measured eutectic fractions, the expected eutectic fraction, under both equilibrium and Guilliver-Scheil conditions, was determined and used as a comparison. For the Guilliver-Scheil estimation it assumed that during solidification there was [28]:

1. No diffusion in the solid phase once its forms,
2. Perfect mixing of solute in the liquid,
3. Equilibrium at the solid-liquid interface, and,
4. Solidus and liquidus are both straight line segments.

The estimation of the equilibrium and the Guilliver-Scheil eutectic fractions can be found in Appendix C.

These expected eutectic fractions, along with the measured eutectic fractions of the IA Al-10Si alloy, were plotted as a function of the particle size and the atomization gas in Figure 4-5.

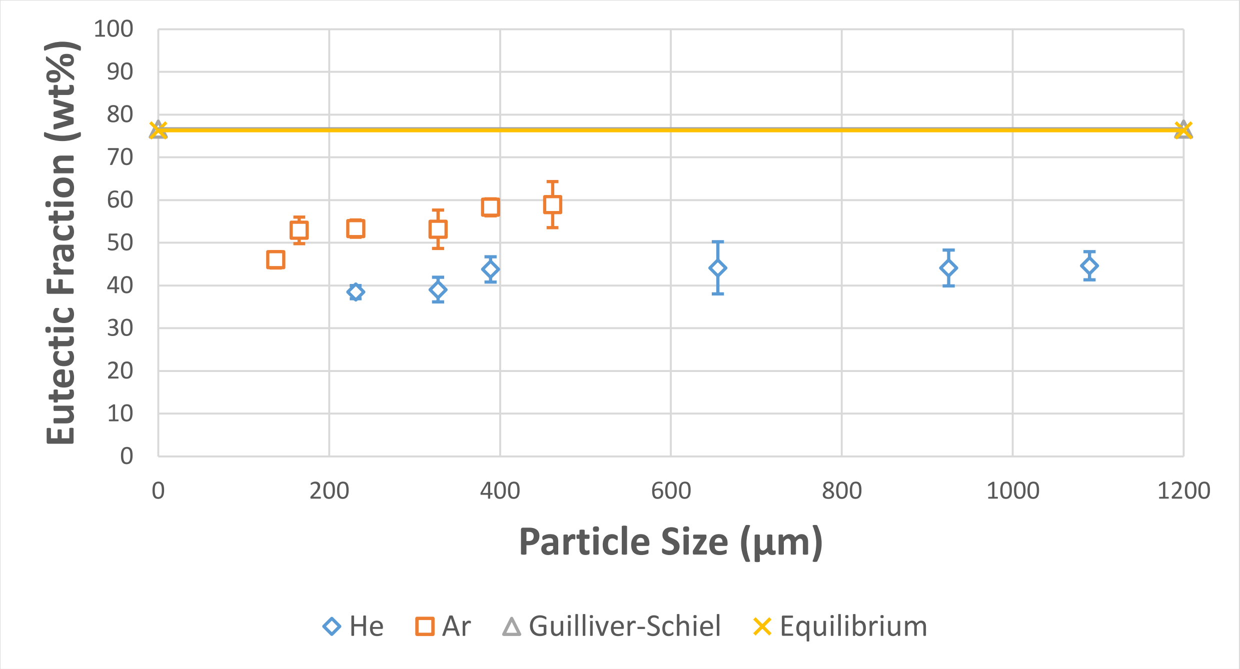

Figure 4-5: Eutectic fraction as a function of the particle size and the atomization gas.

Examining Figure 4-5, the eutectic fraction of the Al-10Si alloy was found to vary as a function of both experimental conditions, as a decrease in the particle size, or using helium instead of argon gas, lead to a decrease in the eutectic fraction.

The eutectic fraction of the impulse atomized Al-10Si alloy was also significantly lower than either the equilibrium or the Guilliver-Scheil estimations, even at the coarsest powder size. This reduction in the eutectic fraction is due to the influence of non-equilibrium effects during solidification, specifically, the large undercooling that is experianced prior to the nucleation of the eutectic structure.

These results demonstrated two things: first, that while the microstructure of the Al-10Si alloy will be composed of an α-Al phase and a eutectic structure, the proportion of each will vary and depend on solidification conditions. Second, that the fraction of these components is noticeably different than what was expected under equilibrium or Scheil conditions.

It should be noted that the reason for the similarity between the equilibrium and the Scheil estimations is the limited solid solubility of Si in Al. This limited solid solubility causes the assumptions of Scheil (i.e. complete mixing in the liquid and no diffusion in the solid [28]) to closely match what is expected under equilibrium conditions.

## 4.2 INFLUENCE OF EXPERIMENTAL CONDITIONS

Understanding the influence of the experimental conditions is an important aspect that must be considered when examining the microstructure of an alloy, as these conditions will noticeably influence the experienced solidification path.

For Impulse Atomization (IA) there are three controllable experimental conditions:

1. The particle size of the powder,
2. The atomization gas, and,
3. The superheat of the melt

In this work the melt superheat was not examined as it remained constant between IA experiments. As such, the influence of the particle size and the atomization gas on the solidification, microstructural refinement, and the hardness of the Al-10Si alloy was examined, with the results of this analysis being presented in this section.

### 4.2.1 **Influence on the Solidification Conditions**

In this section the influence of the experimental conditions on the solidification conditions of the Al-10Si alloy will be presented.

### *4.2.1.1 Eutectic Nucleation Undercooling*

The eutectic nucleation undercooling, which represents the undercooling prior to the nucleation of the eutectic structure, was the first condition to be examined. This undercooling is an important solidification parameter as it will significantly affect the refinement and morphology of the Al + Si eutectic structure.

#### 4.2.1.1.1 Estimation Method

To estimate the eutectic nucleation undercooling a trial and error method was developed that used the experimental measurements of the eutectic fraction, the Guilliver-Scheil micro-segregation model and meta-stable extensions of both the solidus and liquidus lines.

This method considered that the nucleation of the eutectic structure represented the end of α-Al phase coarsening. As such, any eutectic that formed did so after the eutectic structure nucleated, making it possible to relate the degree of eutectic undercooling to the amount of eutectic that was present within the microstructure.

Essentially the extensions of the solidus and liquidus would be used to estimate the theoretically expected eutectic fraction, under Guilliver-Scheil conditions, at a specific temperature. Using trial and error this theoretically calculated eutectic fraction would be compared to the measured eutectic fraction, until these two values matched. Once they did the eutectic nucleation temperature would be known and could be used to determine the eutectic nucleation undercooling.

To measure the eutectic fraction the process outlined in Section 4.1.2 was used. While the meta-stable extensions of the solidus and liquidus were found using ThermoCalc 2016b software with the ALDEMO and MALDEMO databases.

A more detailed explanation of this method can be found in Appendix D and the MATLAB script used for the eutectic nucleation undercooling estimation can be found in Appendix E.

#### 4.2.1.1.2 Results

The estimations of the eutectic nucleation undercooling, for each particle size range, were plotted as a function of the experimental conditions in Figure 4-6.

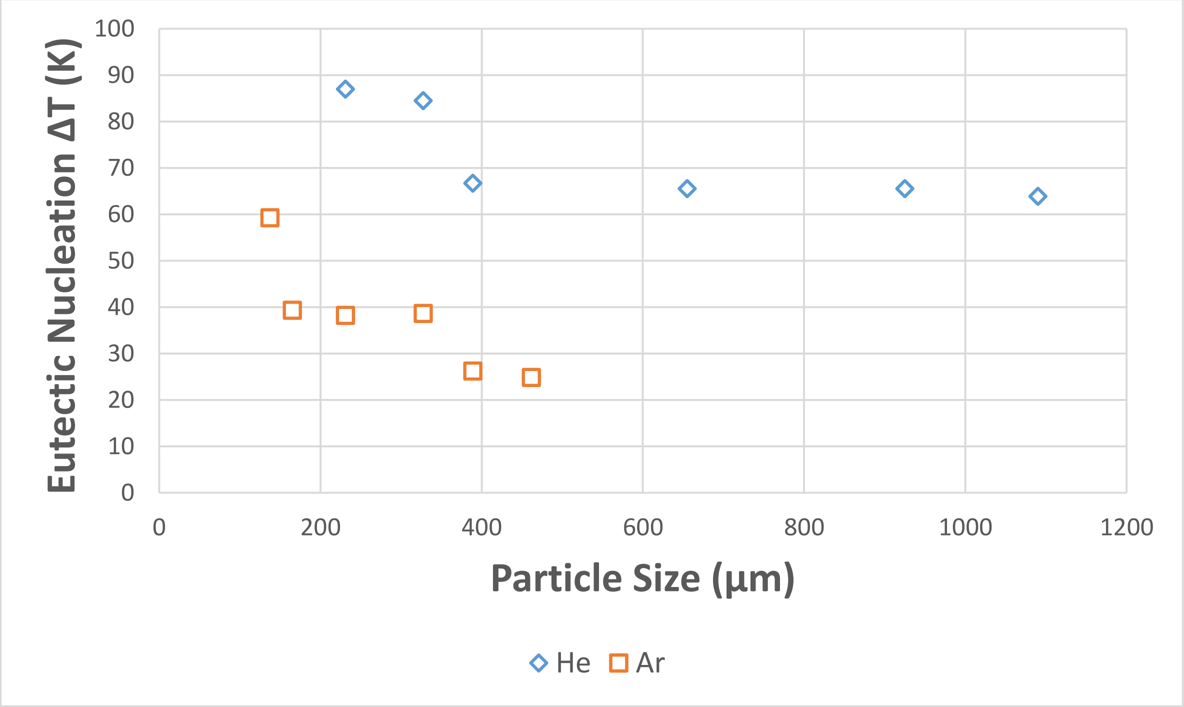

Figure 4-6: Eutectic nucleation undercooling as a function of the experimental conditions.

Figure 4-6 shows that both experimental conditions influenced the eutectic nucleation undercooling. With respect to the particle size, it was observed that a decrease in size led to an increase in the eutectic nucleation undercooling. The cause of this trend is the larger surface area to volume ratio of smaller particles. Having a larger surface area, relative to the volume, means that more of the molten droplet is in contact with the surrounding gas. Consequently, it allows for heat to be more effectively transferred to the surroundings and thus a higher undercooling to be achieved. Similar trends between the particle size and the undercooling were found in past works that dealt with other atomization techniques [46] [59] [60] [61].

In terms of the atomization gas it was found that using helium noticeably increased the eutectic nucleation undercooling. This was due to the substantially larger heat capacity and thermal conductivity of helium, which allows for heat to be more effectively extracted during solidification. Examining the thermo-physical properties of the two gases in Table 4-1 the heat capacity and thermal conductivity of helium is an order of magnitude larger than for argon.

Table 4-1: Thermo-physical properties of gases *[62]*.

| **Property** | **Units** | **Argon** | **Helium** |
|---|---|---|---|
| Heat Capacity | $Jkg^{-1}K^{-1}$ | 520 | 5195 |
| Density | $kgm^{-3}$ | $539.23 \cdot T^{-1.0205}$ | $48.14 \cdot T^{-1}$ |
| Conductivity | $10^4 WK^{-1}m^{-1}$ | $1.86 \cdot T^{0.7915}$ | $38.05 \cdot T^{0.7098}$ |
| Dynamic Viscosity | $10^5 Pa\ s$ | $0.0238 \cdot T^{0.7913}$ | $0.0367 \cdot T^{0.7}$ |

Between the two experimental conditions the atomization gas appeared to have a dominating influence; as none of the examined powders that were atomized in argon had an eutectic undercooling larger than a powder that was atomized in helium.

#### *4.2.1.2 Average Solidification Cooling Rate during α-Al Phase Coarsening*

The second condition to be examined was the average solidification cooling rate, which refers to the average solidification rate over the entirety of α-Al coarsening. This is an important solidification factor, because it will directly affect the secondary dendrite arm spacing (SDAS) and the overall scale of the microstructure. In Al alloys, reducing the SDAS is desired, as this will improve the distribution of the intermetallic and secondary phases [19] [65] [66], leading to more uniformly distributed properties.

#### 4.2.1.2.1 Estimation Method

To estimate the average solidification cooling rate, the range of α-Al coarsening must be defined.

During the solidification of the Al-10Si alloy the temperature of the droplet will cool at a rate that is dependent on the heat extraction divided by the specific heat [28]. In the absence of nucleation this droplet will become undercooled, until the temperature drops low enough that it reaches the characteristic nucleation temperature of some component within the droplet [28]. At this point the nucleation of the primary α-Al phase will occur, signaling the beginning of solidification.

Once the primary phase nucleates it causes the release latent heat, due to a change in entropy, which increases the temperature of the droplet, even though the overall heat content of the droplet decreases [28]. This phenomenon is referred to as recalescence.

The period of recalescence ranges from the primary nucleation temperature ($T_P$) to the end of recalescence temperature ($T_R$), where the end of recalescence is the point where all released latent heat has been absorbed. During this period of recalescence the nucleation and growth of the primary α-Al phase will occur.

After this period of recalescence α-Al coarsening will begin and will continue until the nucleation of the eutectic structure. From this the period of α-Al coarsening can be defined as the region between the end of recalescence temperature ($T_R$) and the eutectic nucleation temperature ($T_E'$).

To help visualize this, the solidification path of an undercooled Al-10Si alloy is schematically presented in Figure 4-7.

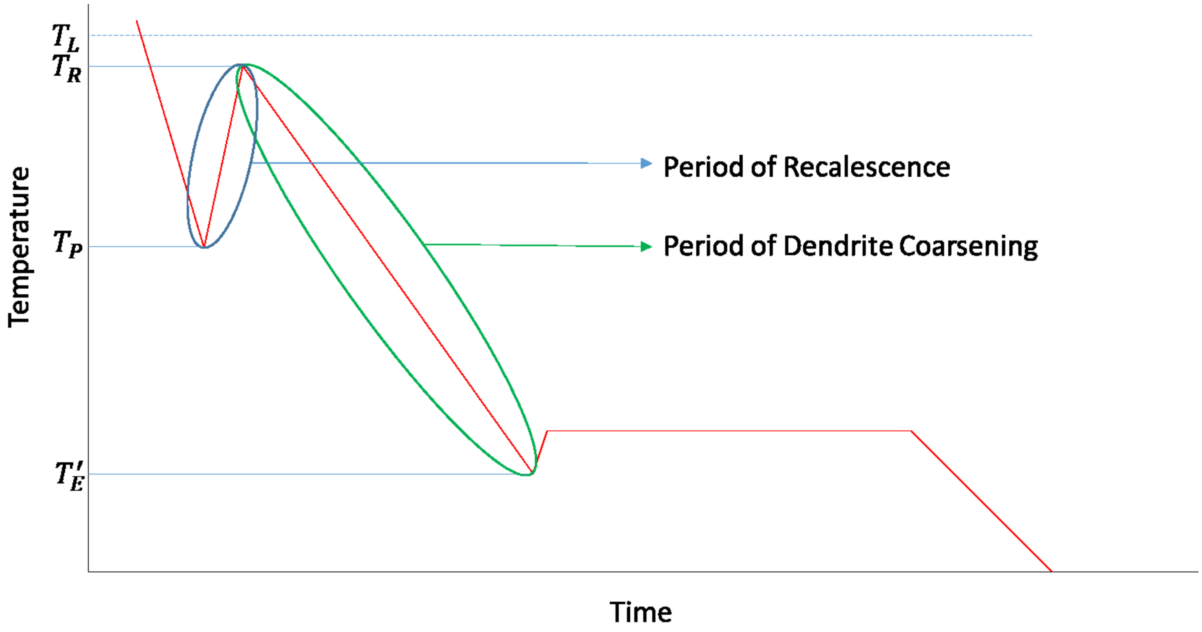

Figure 4-7: Schematic of an undercooled Al-10Si alloy, where the periods of recalescence and α-Al dendrite coarsening are highlighted.

Using this defined period of α-Al coarsening a method was developed, to estimate the average solidification cooling rate, that combined the estimation of the eutectic nucleation undercooling (from Section 4.2.1.1) with the thermal model that was developed by Wiskel et al. [56].

The estimation of the eutectic nucleation undercooling would be used to determine the temperature where α-Al coarsening ended ($T_E'$). While, the thermal model would be used to determine the temperature ($T_R$) and time ($t_R$) where coarsening began, along with the time where the $T_E'$ occurred. With these four values one could determine the average solidification cooling rate:

$$\dot{T} = \frac{T_R - T_E'}{t_R - t_E'} \qquad (4\text{-}1)$$

Where $\dot{T}$ is the average solidification rate during coarsening, $t_R$ is the time at which the end of recalescence occurred and $t_E'$ is the time at which the eutectic structure nucleated.

The thermal model developed by Wiskel et al. [56] describes the heat flow during the solidification of an IA droplet and is set-up as an .exe file that uses user inputs to calculate the thermal history of an IA droplet.

The first requirement of this .exe program is an input file containing the materials data of the examined alloy. The file used for the Al-10Si alloy can be found in Appendix F.

The second set of inputs are user inputs that are listed below:

1. Primary Nucleation Undercooling
2. Atomization Gas
3. Initial Gas Temperature (300K)
4. Droplet Diameter
5. Time Step (0.0001s)
6. Initial Melt Temperature
7. Stop Temperature (500C)
8. Initial Velocity (0.5m/s)

Inputs 2, 3, 4 & 6 depend on the sample and the experimental conditions, while inputs 5, 7 & 8 stay constant unless specified otherwise. For Input 1, the primary nucleation undercooling, its value was set to zero as it was found that the average solidification cooling rate did not vary much with this inputted $\Delta T_p$. This limited variability of the cooling rate, with respect to the inputted $\Delta T_p$, is shown in more detailed in Appendix G.

With these inputs the thermal model outputted the end of recalescence temperature ($T_R$), along with the thermal history of the droplet in a temperature vs. time .txt file. With this $T_R$, and $T_E'$ known the temperature vs. time .txt file was used to determine the time at which these two temperatures occurred. Thus, helping determine the $t_R$ and the $t_E'$.

The MATLAB code that was used to estimate the $\dot{T}$ can be found in Appendix H.

###### 4.2.1.2.2 Results

This estimated average solidification cooling rate was plotted as a function of the particle size and atomization gas in Figure 4-8.

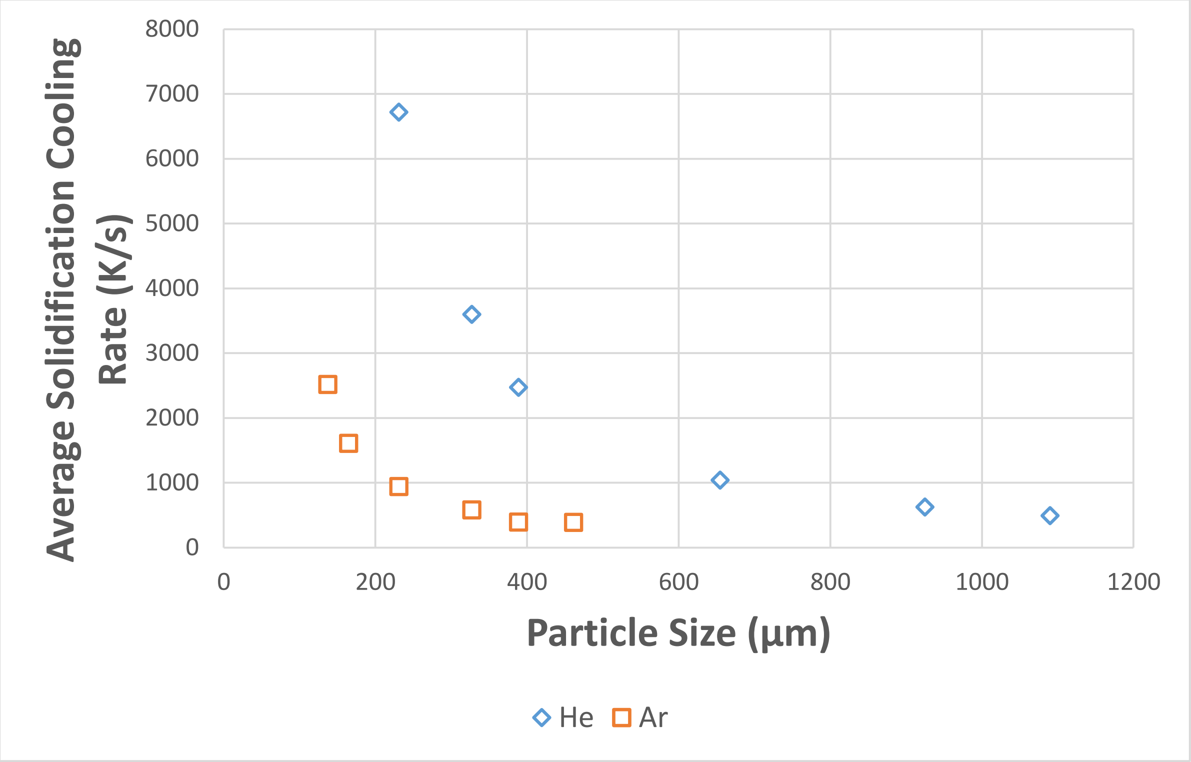

Figure 4-8: Average solidification cooling rate as a function of the experimental conditions.

Figure 4-8 shows that the IA Al-10Si alloy was able to achieve high solidification cooling rates. With the argon atomized samples having solidification cooling rates between ~400 to 2500 K/s, and the helium atomized samples having solidification cooling rates between ~500 to 6700 K/s.

From Figure 4-8, it was also observed that the experimental conditions had a noticeable impact on the average solidification cooling rate.

In terms of the particle size, it was found that the solidification cooling rate would increase as the particle size decreased, where the influence of the particle size became more pronounced as the size got smaller. This result was expected due to the larger surface area to volume ratio of smaller particles, which allows for a faster rate of heat extraction, from the sample, during solidification.

In terms of the atomization gas, it was found that the solidification cooling rate would be noticeably larger if helium gas was used instead of argon. The cause of this was the larger thermal conductivity and heat capacity of helium, which allows for heat to be more effectively extracted during solidification.

#### 4.2.1.2.3 Validation of Results

To validate this estimation of the average solidification cooling rate, a comparison with previous work on Al-Si alloys was conducted. The comparison entailed an examination of the relationship between the solidification cooling rate and the secondary dendrite arm spacing (SDAS).

As mentioned in Section 4.2.1.2 the size of the formed α-Al secondary dendrite arms is related to the amount of coarsening that occurs during solidification; where this coarsening is driven by the concentration gradient between the dendrite arms, along with the mass transfer from small arms to larger arms [67].

This mass transfer dependence of dendrite coarsening means there is also a time dependence. Using this Jones developed a relationship between the secondary dendrite arm spacing and the cooling rate which is shown below [68]:

$$\lambda = B(\dot{T})^{-n} \tag{4-2}$$

Where $\lambda$ is the secondary dendrite arm spacing (SDAS), $\dot{T}$ is the average solidification cooling rate during coarsening and B and n are constants. The B constant is based on the coarsening parameter (M) and as such should remain constant, as long as the alloy composition does not change.

For aluminum alloys the expected values for B & n are 50 and 1/3 respectively [68]. However, it was found that by varying the solute content, and the solidification conditions, deviations from these values can occur. For Al-Si alloys at 2.8, 4.3, 5, 6.9, 8.4 and 10wt% Si the B and n values ranged between 27-51 and 0.25-0.29 respectively [63]. The shifts in n and B were attributed to variations in the Si content, where increasing the Si content led to a decrease in the SDAS. This was ascribed to the low solubility of Si in Al that allowed for the extra solute to build up around the coarsening dendrites and impede their growth [63].

While the work [63] provided insight into the B & n values for Al-Si alloys, it only dealt with slow cooling conditions, over a limited range of cooling rates (0.1 to 200 K/s). Work done by Armstrong & Jones [69] determined the B and n constant for an Al-10.5wt%Si alloy at significantly higher cooling rates (400 to 12000 K/s). It was found that the average B value was ~47 and the average n value was ~1/3, which cohered with the previously obtained values.

To determine the B and n values for the impulse atomized Al-10Si alloy the α-Al dendrite cell spacing (from Section 3.5.1) was plotted as a function of the estimated average solidification cooling rate. From this, a log-log plot (with a power function fit) could be used to determine the B and n values. This plot, and derived power function, for the Al-10Si alloy is given in Figure 4-9. Also presented are past work by Anyalebechi [63] and Armstrong [69] for reference.

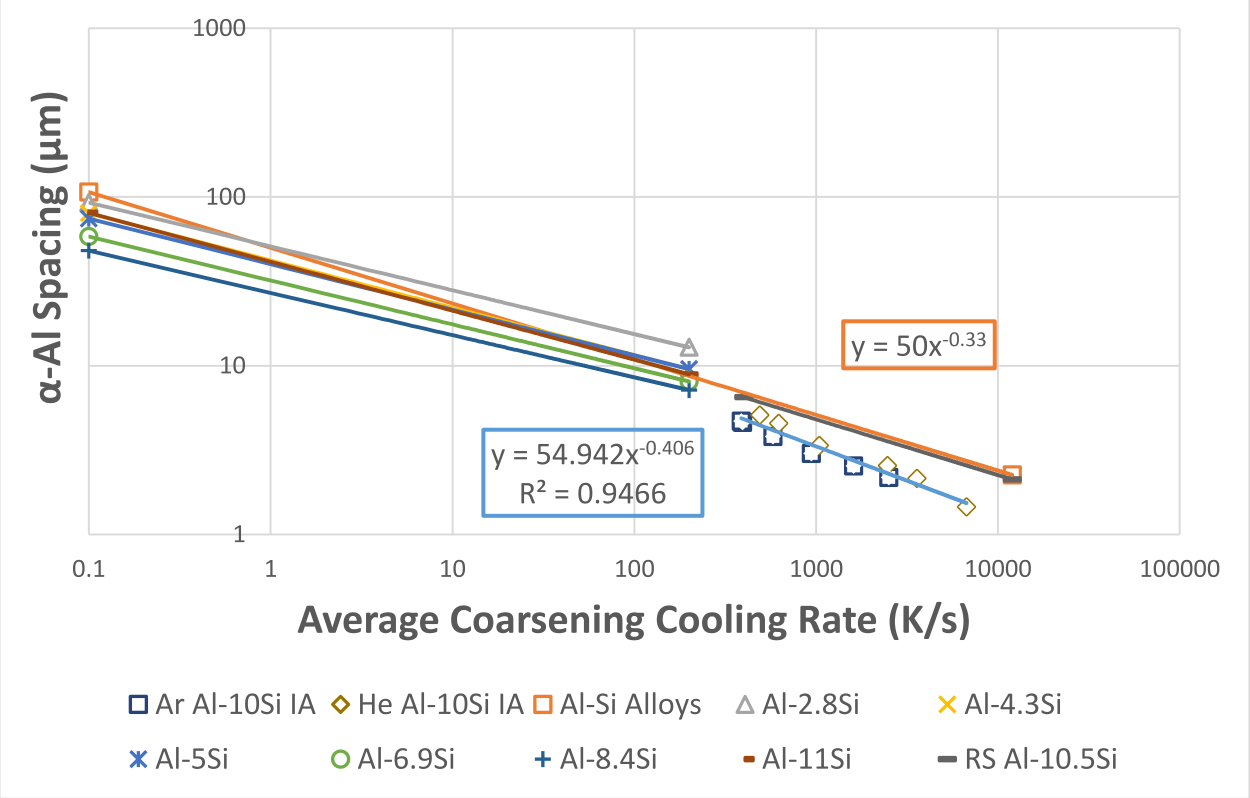

Figure 4-9: α-Al dendrite cell spacing as a function of the average solidification cooling rate. The B & n values for the impulse atomized Al-10Si alloy are shown in blue. The typical B & n values for Al alloys are shown in orange. This plot also includes B & n values from past work with Al-Si alloys by Anyalebechi *[63]* and Armstrong *[69]*.

Examining Figure 4-9, the values obtained in this research are very close to those reported by other workers, where the B and n values of IA Al-10Si alloy were found to be ~55 and ~0.41 respectively.

The most likely cause for the slight variation of the B & n values, for the Al-10Si alloy, was a lack of statistics. To get B & n values closer to 50 and 1/3, this SDAS versus cooling rate relationship needs to be conducted over a wider range of cooling rates, ideally over at least four to five orders of magnitude [70]. And as can be seen from Figure 4-9 the plotted points for the Al-10Si alloy only ranged over two orders of magnitude.

### 4.2.2 **Influence on the Interphase Spacing**

In this section the influence of the experimental conditions on the interphase spacing of both the α-Al phase and the Al + Si eutectic structure is presented.

#### *4.2.2.1 α-Al Interphase Spacing*

To quantify the influence of the experimental conditions on the refinement of the α-Al interphase spacing, dendrite cell spacing measurements from Section 3.5.1 were plotted as a function of the experimental conditions in Figure 4-10.

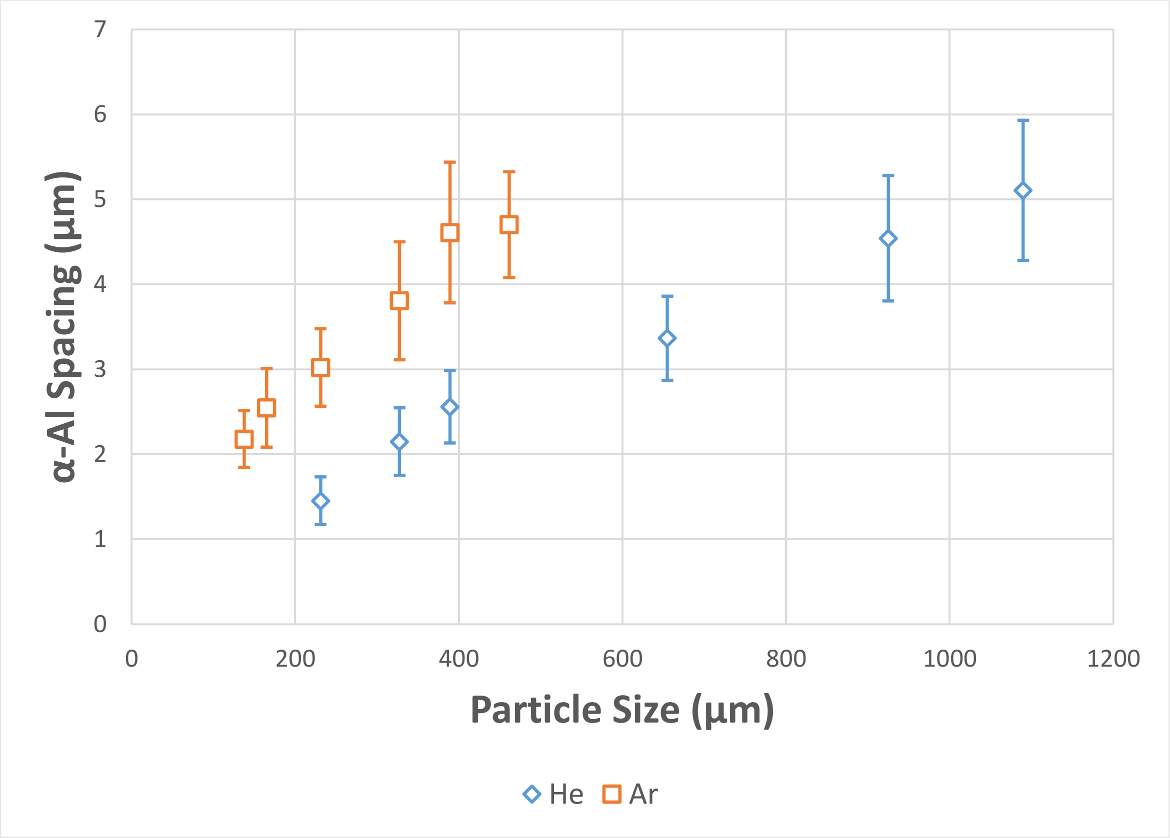

Figure 4-10: α-Al dendrite cell spacing as a function of the experimental conditions.

From Figure 4-10, a decrease in the particle size led to an increase in the refinement of the α-Al phase. This increased refinement was also observed when using helium instead of argon for the atomization gas. Both results were expected as similar trends were seen between the experimental conditions and the average solidification cooling rate in Section 4.2.1.2.

#### *4.2.2.2 Eutectic Si Interphase Spacing*

To quantify the influence of the experimental conditions on the refinement of the eutectic structure, eutectic Si spacing measurements from Section 3.5.2 were plotted a function of the experimental conditions in Figure 4-11.

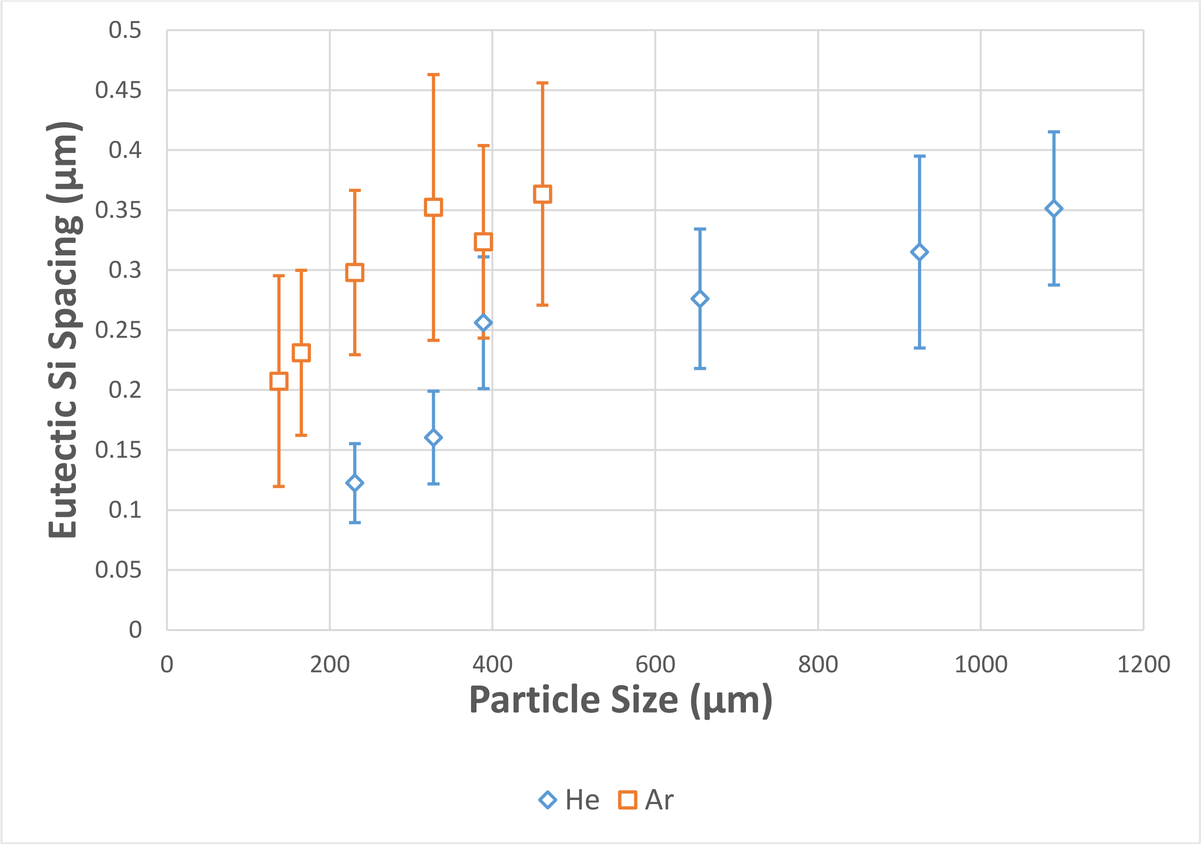

Figure 4-11: Eutectic Si spacing as a function of the experimental conditions.

From Figure 4-11, it was observed that the eutectic Si spacing would decrease as the particle decreased, and when helium was used instead of argon as the atomization gas. This is due to how a smaller particle size, and the use of helium instead of argon gas, increases the rate of solidification, leading to greater refinement. Both results were expected as similar trends were seen between the experimental conditions and the eutectic nucleation undercooling in Section 4.2.1.1.

### 4.2.3 **Influence on the Alloy Hardness**

To quantify the influence of the experimental conditions, on the mechanical properties, the Vickers hardness of the Al-10Si alloy was plotted as a function of the experimental conditions in Figure 4-12.

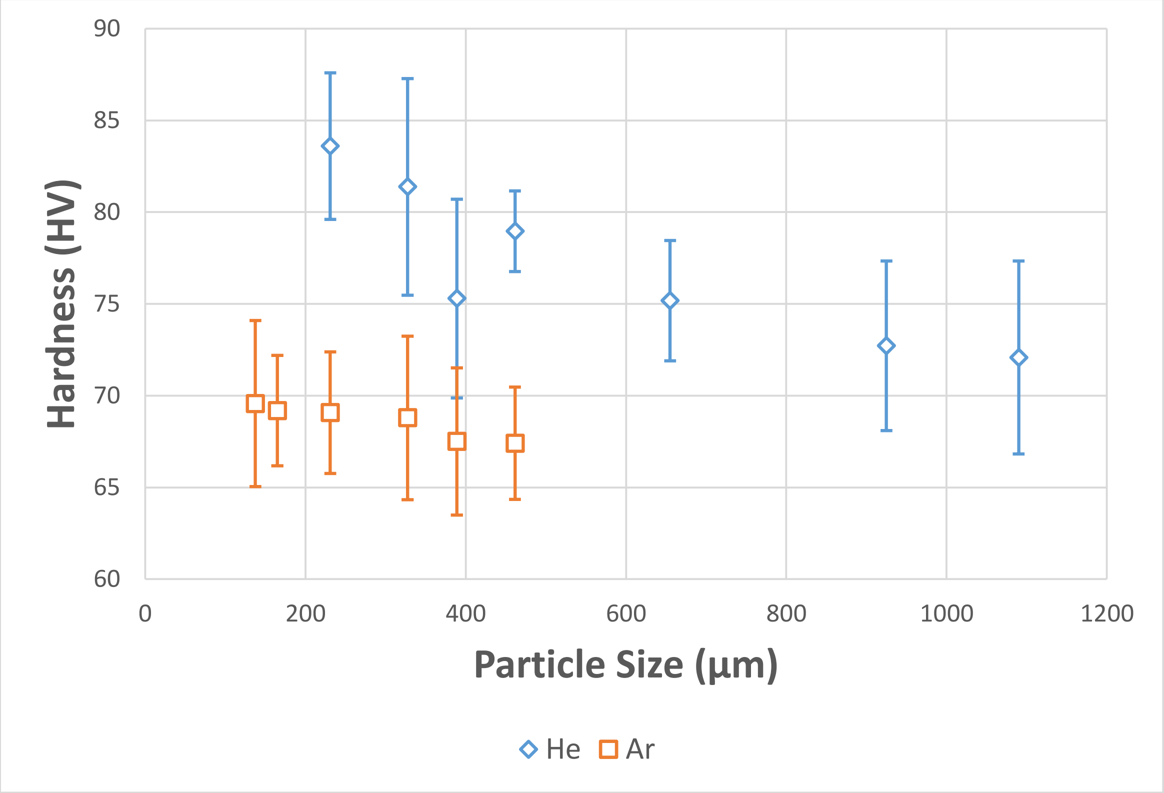

Figure 4-12: Vickers hardness as a function of the experimental conditions.

Examining Figure 4-12 the influence of the atomizing gas is evident, as the helium atomized samples had a higher hardness than the argon atomized samples. However, the influence of the particle size was less clear.

The hardness being a function of particle size was clear for the helium atomized samples. However, the same trend was not observed in argon atomized samples. This result suggests that a deeper, underlying factor is causing this variation in the measured hardness. Moreover, this result indicates that variations in the hardness cannot be explained simply by the experimental conditions of IA.

## 4.3 PRIMARY $\alpha$-AL PHASE NUCLEATION & GROWTH

In this section the influence of rapid solidification on the nucleation and growth of the primary α-Al phase is examined. This involves an analysis on the number of primary nucleation sites, along with a cataloging of the various α-Al phase growth morphologies.

### 4.3.1 **α-Al Nucleation**

From past work with IA it was found that the number of primary phase nucleation sites in Al alloys was dependent on the alloy system. As Al-Cu [13] and Al-Fe [71] alloys were found to have a single nucleation event. Meanwhile, Al-Ni alloys were shown to have multiple nucleation events [72]. To determine the number of nucleation sites, these past works used X-Ray micro-tomography which provided a 3D characterization of a powder's microstructure. However, in the current work with the Al-10Si alloy there was not an opportunity to conduct X-Ray micro-tomography. Hence, a different approach was used.

This different approach considered that if a powder had a single nucleation event it meant that the powder would have grown as a single crystal [13]. As its only direction of growth should be away from the lone nucleation site. So, it was stated that if it could be proven that a powder grew as a single crystal, then it could be said that the powder had a single nucleation event. However, if the powder did not grow as a single crystal, then it meant that the powder had multiple nucleation events.

Using this logic, the number of nucleation sites in the Al-10Si powders was determined via EBSD analysis, with the results being shown in Figure 4-13. Examining Figure 4-13B, we can see that the growth in the Z-direction is completely uniform. These are characteristics of single crystal growth, which seems to show that the Al-10Si powder had a single nucleation event. Looking at Figure 4-13C, the pole figure data shows a distinct and unique crystallographic texture. Again, these findings point to the fact that the powder grew as a single crystal. This type of result was seen by the other Al-10Si powders that were analyzed via EBSD.

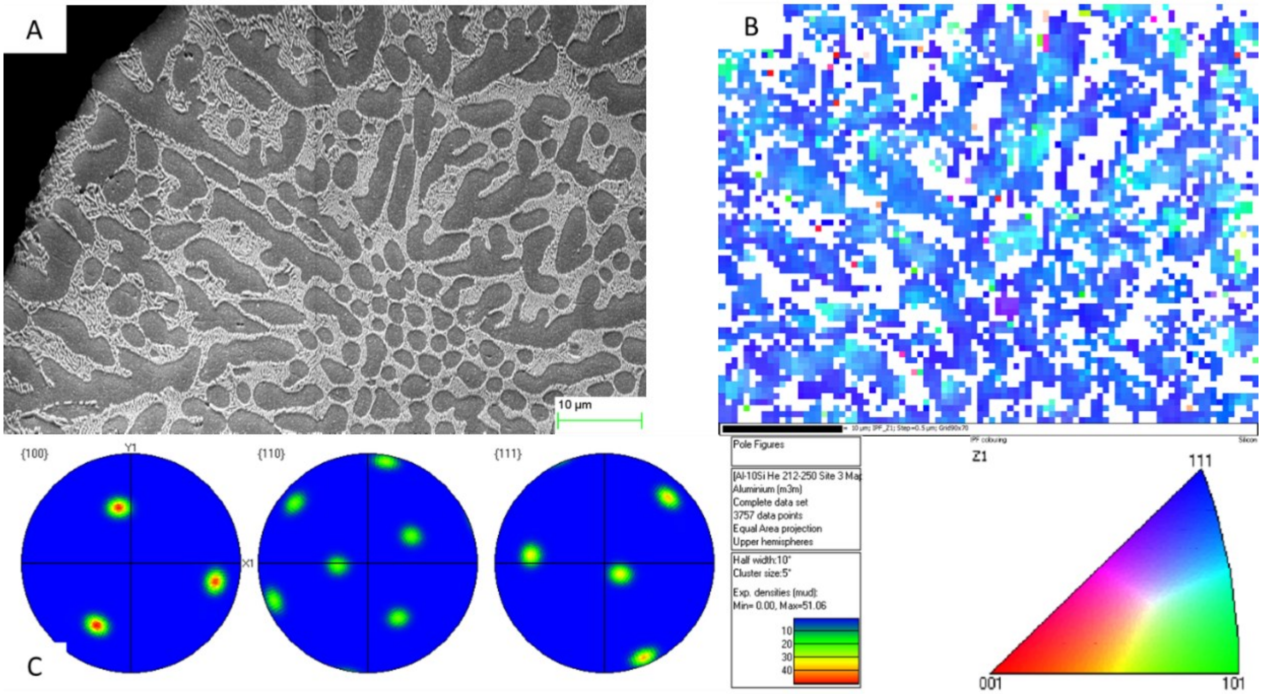

Figure 4-13: EBSD results for a He 212-250µm powder. A) FE-SEM image of the analyzed section of the powder. B) Z-axis crystallographic orientation overlaid onto the original image. C) Pole Figure data.

While the Al-10Si powders were found to have a single nucleation point from EBSD analysis, there were instances of multiple nucleation events as well. These were found from visual inspections of the powder surfaces. Figure 4-14 shows an example of a powder with multiple nucleation events on its surface.

These two results show that the Al-10Si alloy has both single and multiple nucleation events. Due to the limitations of the analysis method that was used, it could not be determined which one was more prevalent within the alloy. Investigating the number of primary nucleation sites should be investigated in future work, ideally with the use of X-Ray micro-tomography.

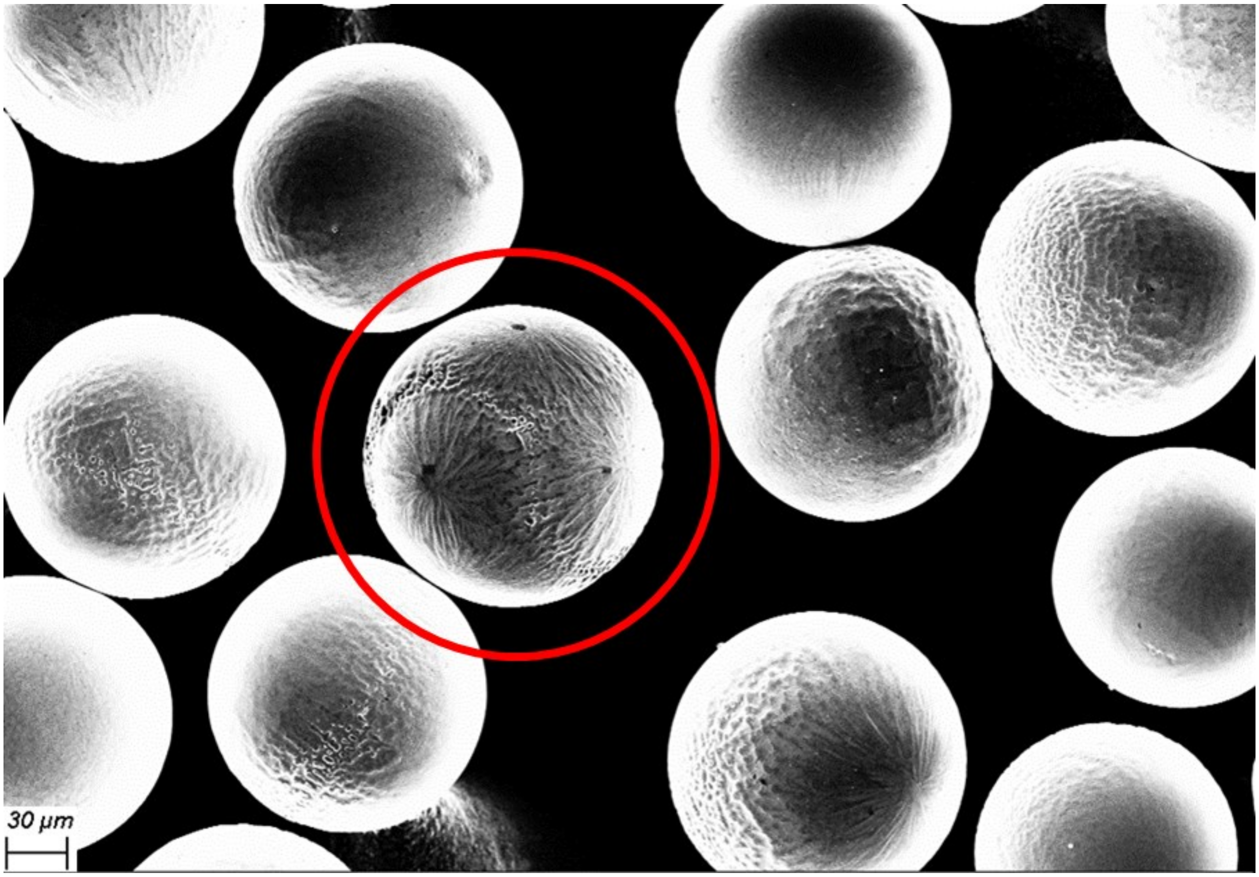

Figure 4-14: FE-SEM image of an Al-10Si powder with multiple primary nucleation sites. Ar 125-150µm sample.

### 4.3.2 **α-Al Growth**

The next aspect to be examined was the growth of the primary α-Al phase. This involved a characterization of the α-Al growth directions, along with a classification of other α-Al morphologies that were present within the microstructure.

#### ***4.3.2.1 <100> Growth***

The first growth direction to be categorized was the <100> growth of the α-Al primary dendrite arms. This <100> growth was defined by the primary arms having a 4-fold symmetry around the nucleation point, causing them to be spaced at 90° from one another. An image of this <100> growth can be seen in Figure 4-15.

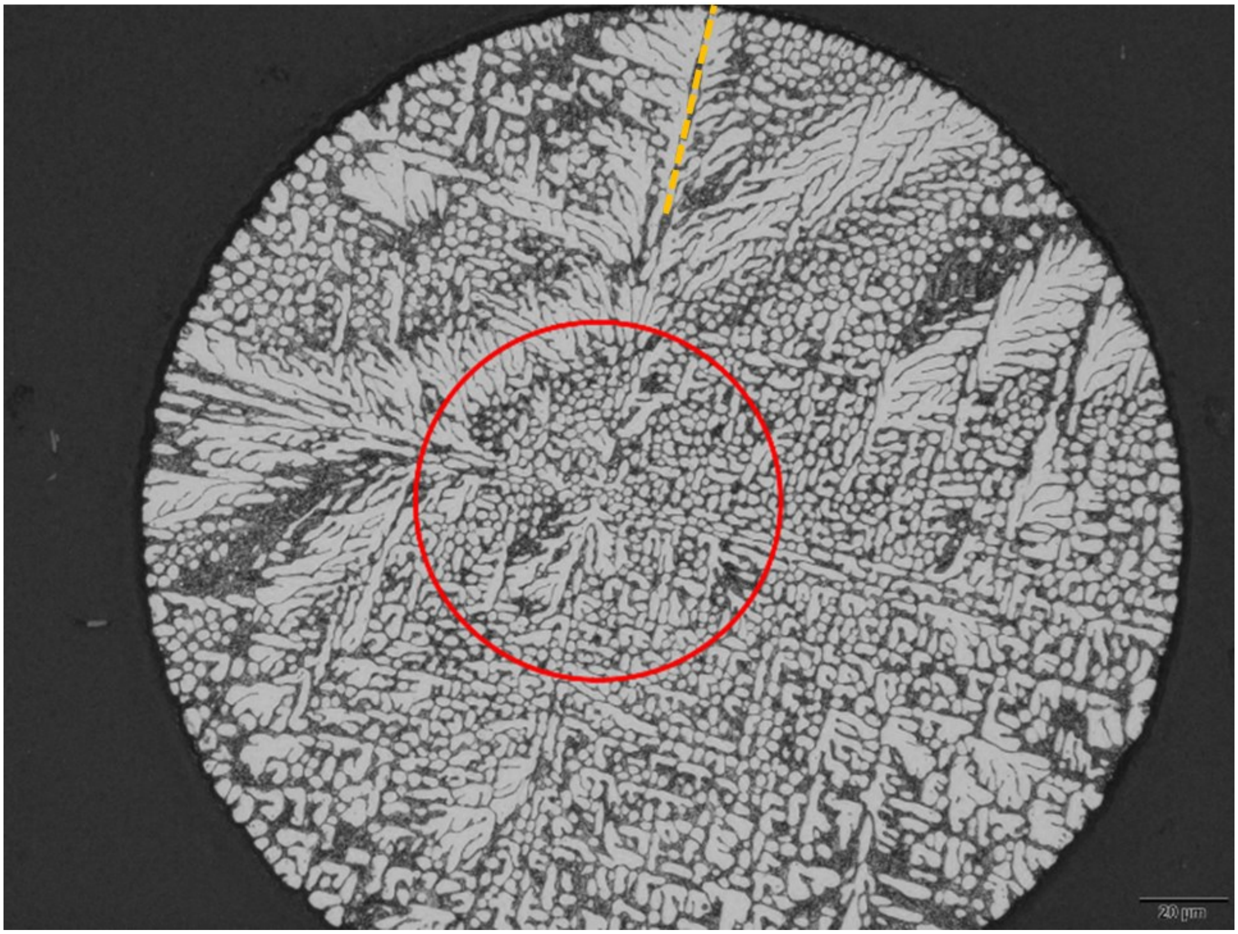

Figure 4-15: OM image of the <100> growth morphology. With the nucleation point being located at the center of the highlighted region. The yellow dotted line highlights a twinned primary dendrite arm. He 212-250μm sample.

The reason this was considered <100> growth was due to the 4-fold symmetry and 90° primary arm orientation. These characteristics relate to the <100> family of growth. To confirm these findings, EBSD analysis was conducted to determine the orientation of growth. From examining the results in Figure 4-16, it was found that the orientation of the primary arms related to the <100> direction, as they aligned exactly with the indexed <100> pole figures. This confirms that this morphology represented <100> growth.

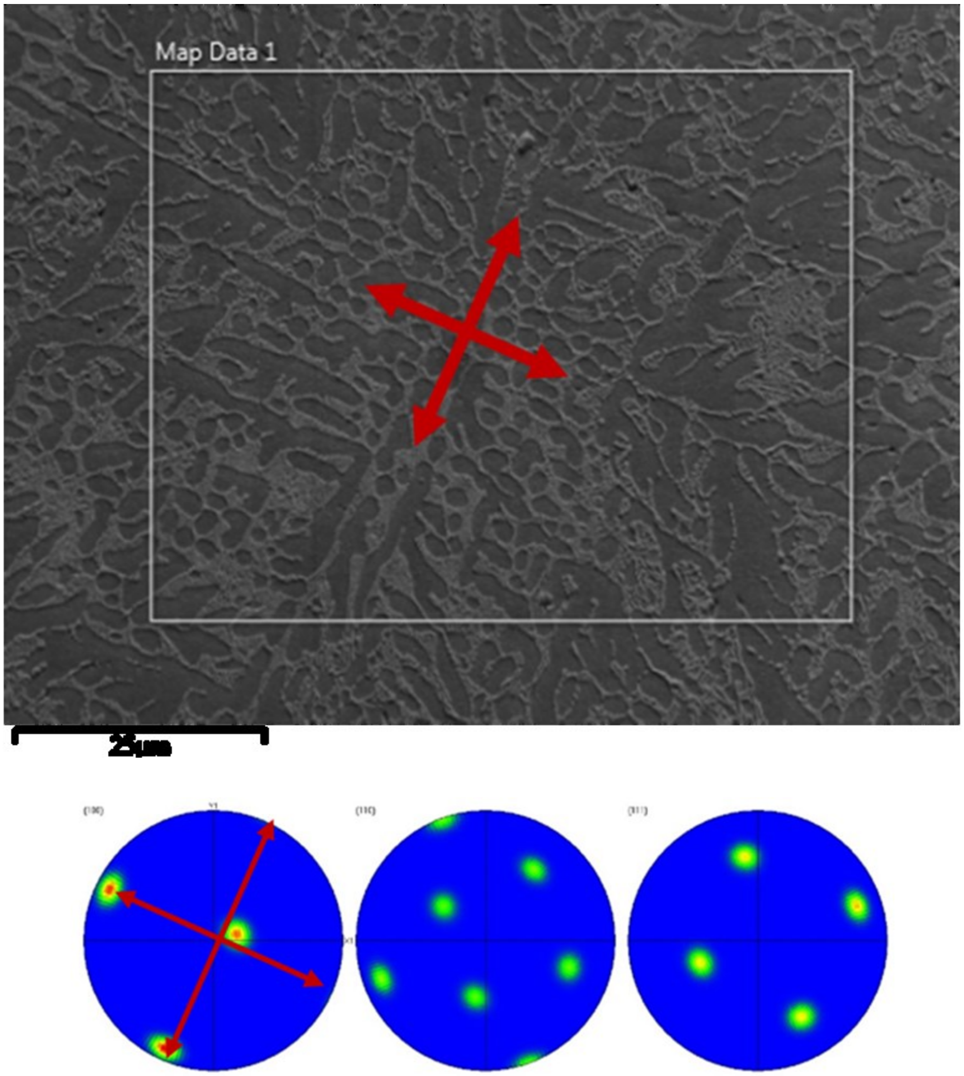

Figure 4-16: EBSD analysis of the <100> growth morphology. Top image shows a FE-SEM image of the analyzed region, with the four arrows showing the growth direction the primary arms. Bottom image shows the pole figures with the primary arm orientation overlaid on the <100> pole figure. He 212-250µm sample.

Looking at past work done with Al alloys this <100> growth is very common. FCC materials, like Al, inherently want to grow in the <100> direction [11].

Looking at Figure 4-15 at the region with the yellow dotted line there appears to be some twinning of the primary α-Al arms. The occurrence of twinning appeared to be inconsistent, almost as if it would stop and start as the primary arms grew. While this may be a 2D effect it was regularly seen when analyzing the Al-10Si alloy, which could signify an oscillation between twinned and untwined growth during solidification.

#### 4.3.2.2 <110> Growth

The second identified growth morphology was the <110> growth of the primary α-Al arms. Here a distinct 6-fold symmetry around the nucleation point was seen, causing the primary arms to be spaced at 60° from one another. An image of this <110> growth can be seen in Figure 4-17.

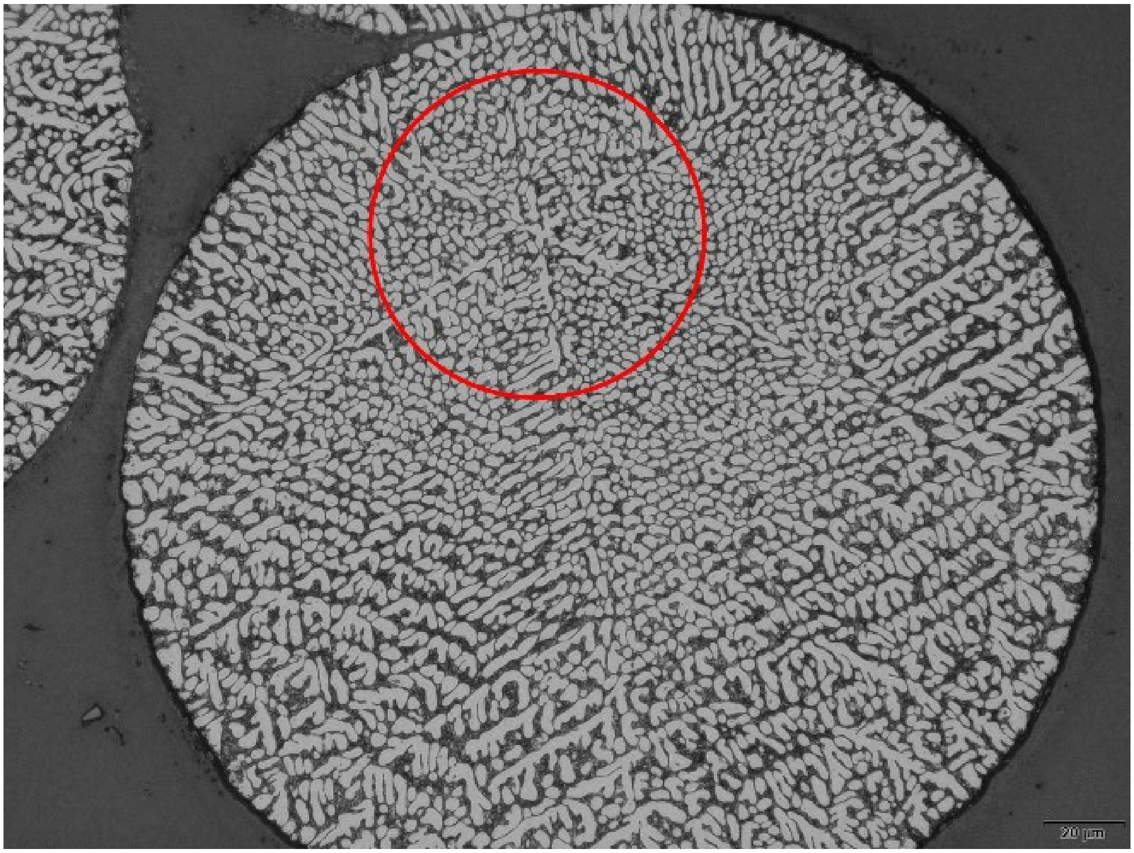

Figure 4-17: OM image of the <110> growth morphology. With the nucleation point being located at the center of the highlighted region. He 212-250µm sample.

The reason this morphology was considered to grow in the <110> direction was that this 6-fold symmetry and 60° arm orientation was indicative of the <110> family of growth. To confirm this, EBSD analysis was conducted to determine the orientation of growth. Examining the results in Figure 4-18 it was found that the orientation of the primary arms related to the <110> direction, as they aligned exactly with the indexed <110> pole figures.

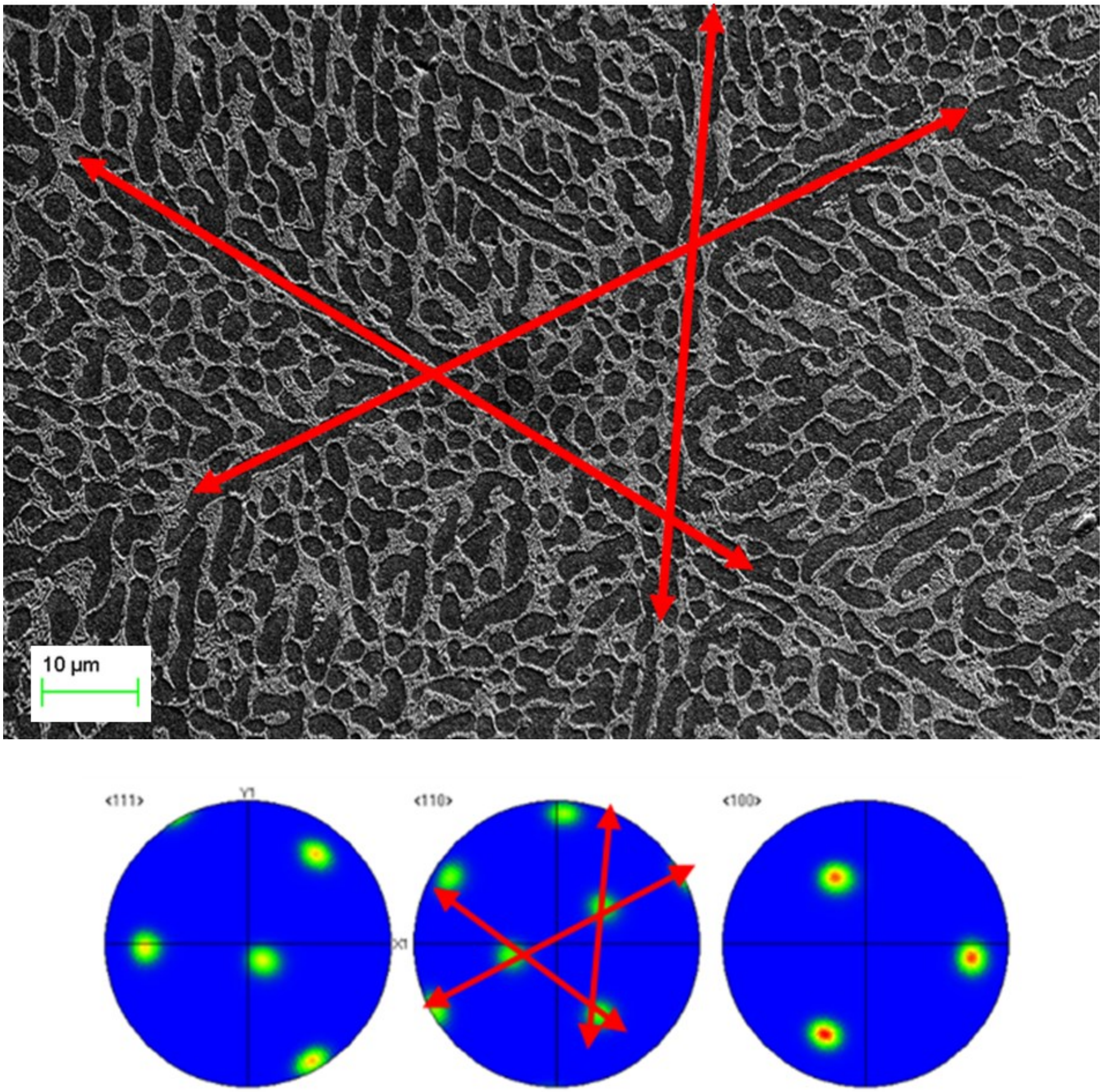

Figure 4-18: EBSD analysis of the <110> morphology. Top image shows a FE-SEM image of the analyzed region, with the six arrows showing the growth direction of the primary arms. Bottom image shows the pole figures with the primary arm orientation overlaid on the <110> pole figure. He 212-250µm sample.

Although FCC materials like Al have a natural tendency to grow in the <100> direction, by varying the alloy composition or by changing the solidification conditions, shifts in the principal direction are possible. In the work done by Henry et al. [11] there was a noticeable amount of <110> growth for many types of aluminum alloys. Also <110> growth was seen in Al-Zn alloys that contained large concentrations of Zn [12] .

#### *4.3.2.3 <100> to <110> Transition*

While the previous sections identified the two growth directions of the primary α-Al arms, the understanding as to why each type of growth occurred remained unidentified, as it was difficult to explain why there was <100> growth instead of <110> growth and vice-versa. In an attempt to address this deficiency, the following section focused on examining this growth transition from <100> to <110>.

Previous work on the <100> to <110> growth transition in Al alloys had attributed it to an increase in solute composition. This effect was shown using a Bridgman set-up by Frideli et al. [12] where they examined an Al-Zn alloy. At low Zn contents, below 25wt%, they found that <100> growth would dominate. However, as the Zn composition increased the growth direction would shift: first to growth in the <320> direction at Zn contents between 25 to 55wt%, before finally shifting to <110> growth when the Zn content was above 55wt%. It was hypothesized that increasing the Zn content would increase the amount of solute present within the alloy. This would in turn increase the solute pile-up and the surface tension anisotropy at the solidification front, eventually causing the surface tension anisotropy to direct the growth of the Al in the <110> direction.

However, this description of the <100> to <110> transition is likely not applicable for the Al-10Si alloy, as its solute is fixed.

Previous work with IA Al alloys examined these shifts in the growth direction, for both Al-Cu [13] and Al-Fe [14] alloys. However, for those alloys it was found that the shift in growth direction would occur directly from <100> to <111>, with no intermediary <110> growth being observed.

While the previous work with IA could not explain the observed <110> growth in Al-10Si, it did provide some intriguing results as to why growth shifted from the <100> direction. In the work with IA Al-Cu alloy, it was found that <111> growth became more prominent at smaller particle sizes, and when helium gas was used instead of argon [13]. This result suggested that transitions from <100> growth, in Al alloys, can result from an increase in the rate of solidification.

This possible influence of the solidification conditions could be mechanistically explained by atom attachment kinetics. While the role of kinetics is relatively low in metallic alloys, its influence will increase as the growth rate increases. If the growth rate is fast enough, the influence of atom attachment kinetics can even dominate over the contribution of the surface tension anisotropy [11]. As such, the start of non-<100> growth could indicate that the solidification conditions are rapid enough for atom attachment kinetics to influence growth.

To examine if <110> growth was dependent on the solidification conditions the proportion of the Al-10Si powders that displayed <110> growth was determined. This was done by conducting a visual analysis of the microstructure to determine the percentage of <110> growth that was observed at each particle size range. The results of this analysis were plotted as a function of the experimental conditions in Figure 4-19.

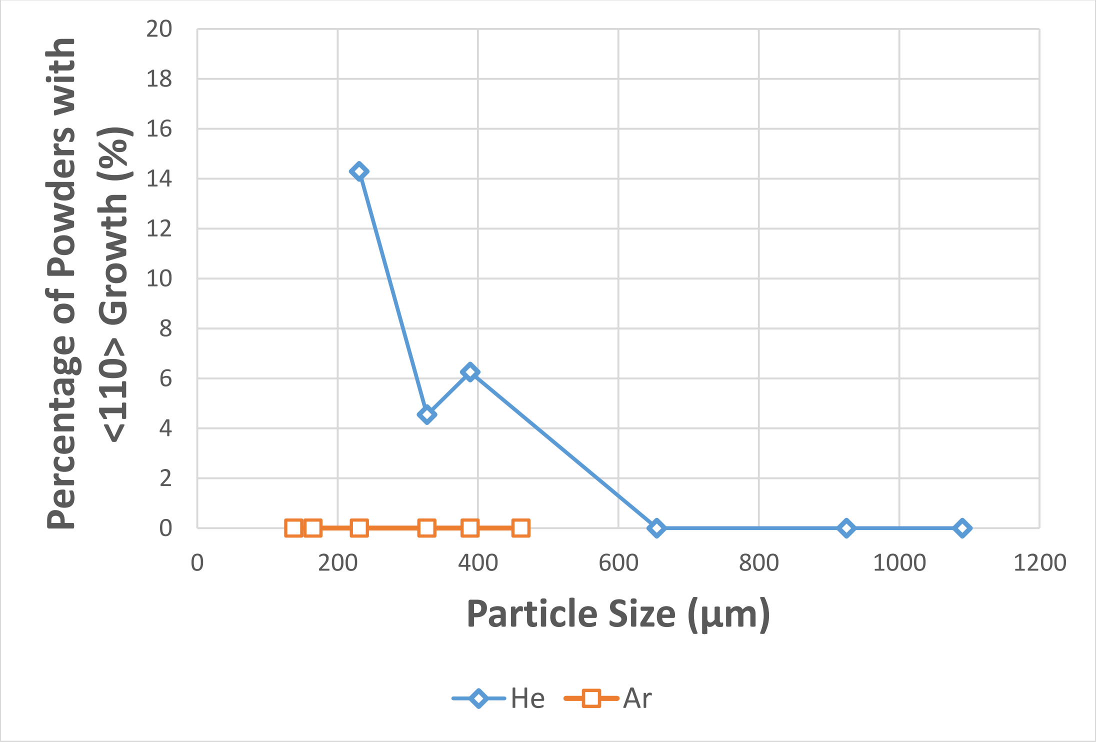

Figure 4-19: Percentage of powders that displayed <110> growth, within a specific particle size range, plotted as a function of the experimental conditions.

Figure 4-19 shows that very little <110> growth was found in the Al-10Si alloy. But it also showed this <110> growth only occurred at the finest particle sizes that were atomized in helium. This result indicates that a decrease in the particle size, and the use helium instead of argon, increases the chances of <110> growth. While this does not confirm that atom attachment kinetics played a role, it does suggest, like the result with the IA Al-Cu alloy [13], that the cooling rate and the undercooling do affect this growth transition.

#### *4.3.2.4 Seaweed Growth*

While the growth morphology of the α-Al phase was dominated by the growth direction, there was another morphology that was observed, which was labelled as a "seaweed" type of growth. This seaweed morphology was characterized by a branched structure that grew outwards from the primary arms, at an angle below 90°. An example of this seaweed growth can be seen in Figure 4-20.

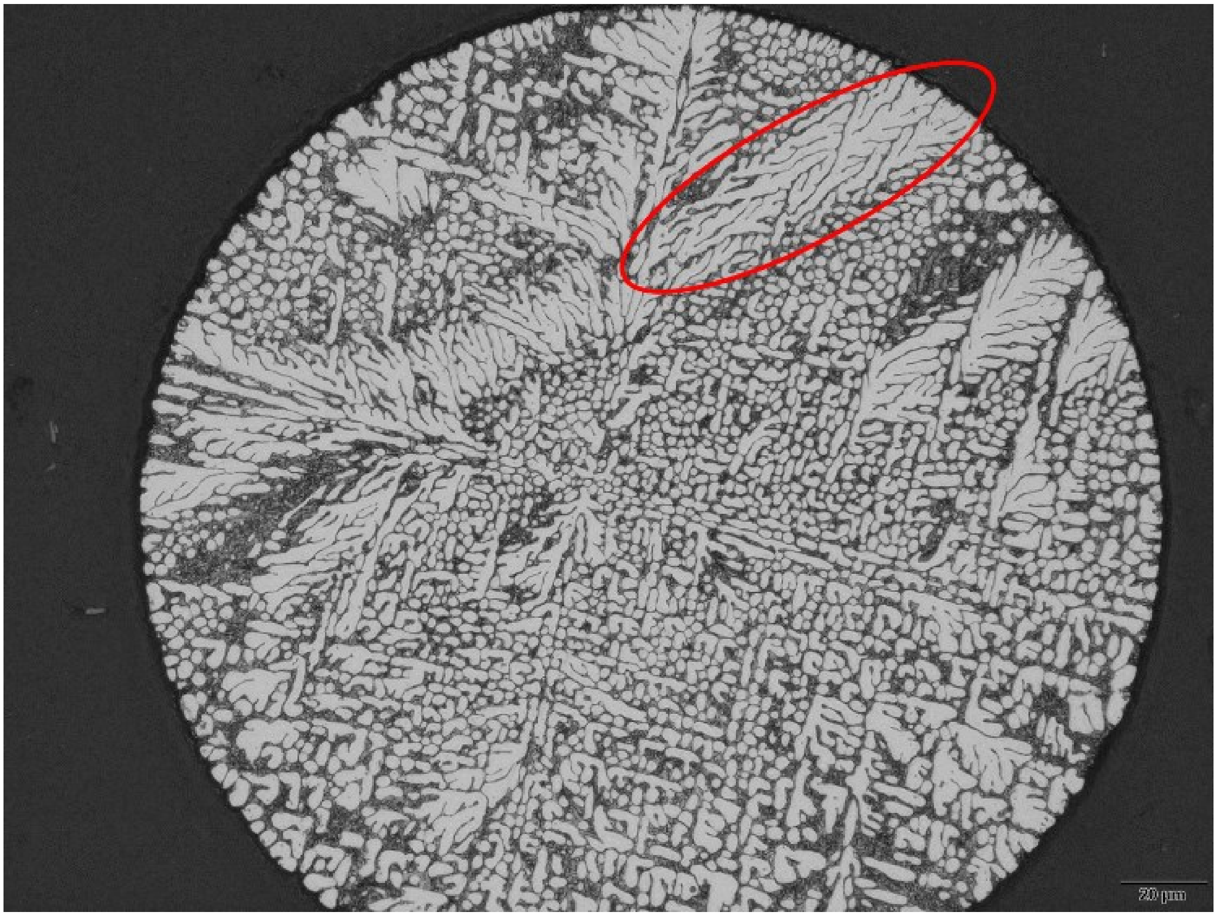

Figure 4-20: OM image outlining the Seaweed growth of α-Al phase. He 212-250μm sample.

During seaweed growth the growing dendrite will bend away from the primary arm and split, causing it to grow in a "zig-zag" fashion. While it is known that the seaweed structure will grow with this morphology, the mechanism behind it is still not well understood.

Friedli et al. [12] considered this zig and zagging of the arms to be a response to perturbations at the solidification front, caused by the solute field of another arm and/or by thermal fluctuations during solidification. The concept was that these perturbations caused the growing arm to switch sides and take an alternative growth direction. In their work with directionally solidified Al-Zn alloys, this switching mechanism was attributed to the surface tension anisotropy at the solidification front; where the rejected solute forced the growing α-Al phase to bend, switch sides and form this seaweed structure.

Work by Cai et al. [73] also found this seaweed growth when examining a directionally solidified Al-Cu alloy. Here they considered its formation to be due a combination of the surface tension anisotropy at the solidification front, along with the melting and remelting of the sample during directional solidification.

However, these explanations for seaweed growth came from works that dealt with slow growth velocities. As such, they did not consider the impact of rapid solidification. Work done by Assadi et al. [74] with $N_{51}Al_{49}$ alloys found that at higher growth velocities seaweed growth was possible; where the formation of the seaweed structure was attributed to the increasing role of atom attachment kinetics.

This rationalization was expanded on by Mullis et al. [75] by examining the transition to seaweed growth during the solidification of a deeply undercooled pure metallic melt. Here they found, via phase-field modelling, that increasing the undercooling led to the formation of a seaweed structure. As undercooling increased the dendrite growth velocity would also increase and promote the onset of dendrite tip splitting. Essentially the growth velocity controls the perturbations at the solidification front, and thus controls the side-branching during dendrite growth. If the growth velocity increases it causes the side-branching to move closer to the dendrite tip. Eventually, this side-branching gets too close to the tip causing it to bend, split and form a seaweed structure.

Mullis considered this shift in the perturbations at the solidification front to be a competition between the surface tension anisotropy and the atom attachment kinetics; where the influence of kinetics became more dominant at higher growth velocities [75].

Due to the complexity of both mechanisms it is difficult to identify what single factor caused this onset of seaweed growth in the Al-10Si alloy, as such further comparisons to past work were made.

In the work of Friedli et al. [12] the seaweed structure was found to grow in the <320> direction. To determine if the seaweed growth of the Al-10Si alloy was the same, EBSD analysis was conducted to determine the growth orientation of the seaweed structure. From EBSD results, see Figure 4-21, there is no indication that the Al-10Si seaweed structure grew in the <320> direction, as neither the primary nor the secondary arms line up with the indexed <320> pole figures. This demonstrates that the seaweed structure in the Al-10Si alloy may not be the same as the seaweed structure observed in the Al-Zn alloy.

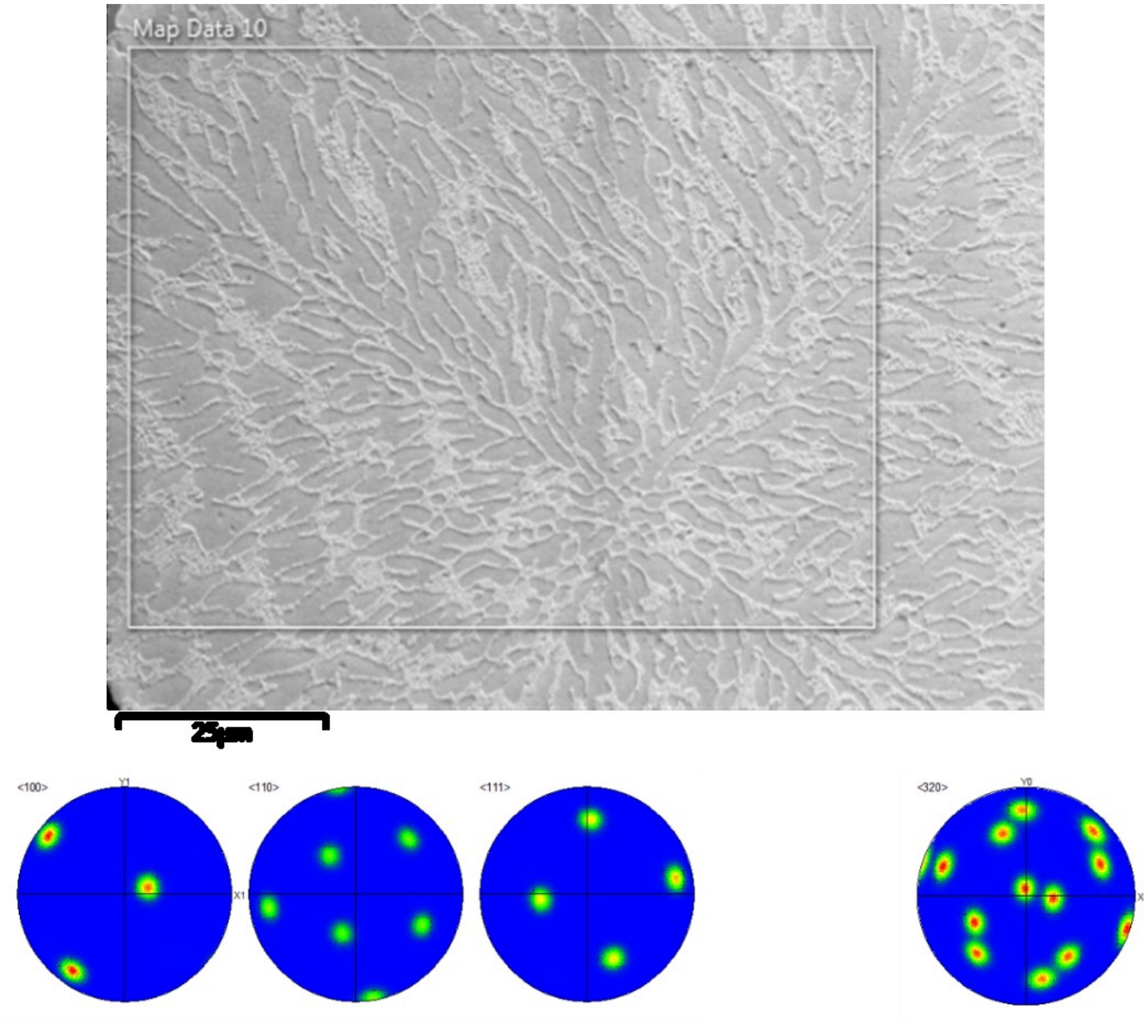

Figure 4-21: EBSD analysis on the seaweed structure of the α-Al secondary arms. Top image shows a FE-SEM image of the analyzed region. Bottom image shows the pole figures. He 212-250µm sample.

Thus, the explanation for seaweed growth, postulated by Friedeli, can be ruled out and the role of the solidification conditions was examined next. If those conditions did influence the formation of the seaweed structure, it would suggest that atom attachment kinetics played a role.

To relate the solidification conditions to this seaweed growth, a visual analysis was conducted to determine the number of powders, within a particle size range, that displayed seaweed growth. This analysis was done for between 7 to 13 powders at each particle size range. The results of this visual analysis were plotted as a function of the experimental conditions in Figure 4-22.

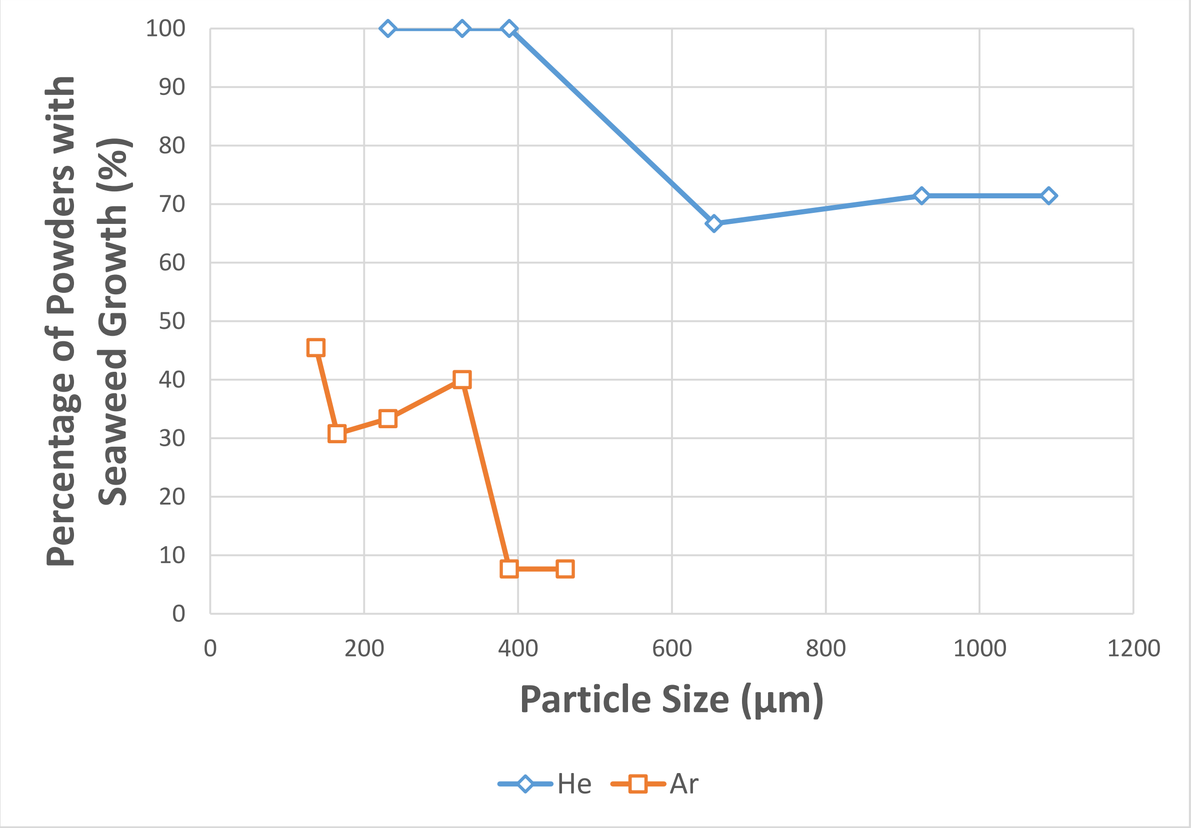

Figure 4-22: Percentage of powders that displayed seaweed growth, within a specific particle size range, plotted as a function of the experimental conditions.

From Figure 4-22, both experimental conditions were shown to noticeably influence the growth of the seaweed structure; where decreasing the particle size and using helium (instead of argon) will make seaweed growth more prevalent. These results indicate that the solidification conditions do in fact control the formation of the seaweed structure. Moreover, these results indicate that this growth of the seaweed structure might be caused by the increasing role of atom attachment kinetics, due to an increase in the α-Al dendrite growth velocity.

## 4.4 SECONDARY AL+ SI EUTECTIC STRUCTURE GROWTH

In this section, the influence of rapid solidification on the growth of the eutectic structure is examined. This examination involved a classification of the eutectic Si growth morphologies, an estimation of the local eutectic solidification conditions and a mapping that combined these two classifications.

### 4.4.1 Eutectic Si Growth Morphologies

Past work on the characterization of eutectic growth has mainly focused on the size and distribution of the Si phase, and not on the Si morphology. While Si spacing can be related to conditions of eutectic growth, it is an inadequate method to describe the Si growth morphology [35]. As the Si spacing only contains indirect morphological information that cannot explain the shift in growth mode behavior [35].

With this being the case new methods were used to characterize these shifts in the growth morphology. These methods involved the development of qualitative and quantitative techniques that used 2D and 3D images of the eutectic structure.

While the qualitative analysis was able to provide some useful insight, the results of the quantitative analysis were inconclusive. While it was not included in this section the results of this quantitative analysis can be found in Appendix I.

#### *4.4.1.1 2D Si Morphology Analysis*

The first qualitative method involved the visual characterization of the Si growth morphologies using 2D images of the eutectic structure. To do this analysis, 2D SEM images of the eutectic structure were characterized into four groups, based on the observed Si morphology.

The first grouping of the Si morphology related to a “Globular” Si morphology, shown in Figure 4-23, where the Si was rounded, refined and compact.

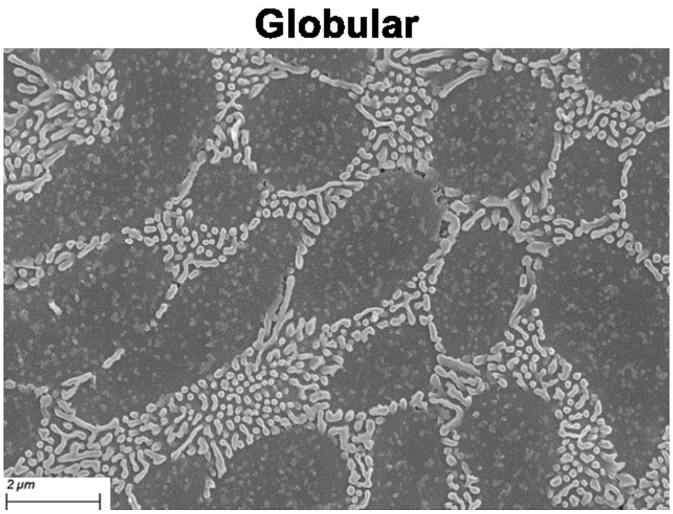

Figure 4-23: FE-SEM image of the "Globular" Si morphology. He 212-250µm sample.

The second grouping related to a “Fibrous” Si morphology, shown in Figure 4-24, where the Si had both rounded and sharp features, along with an elongated shape.

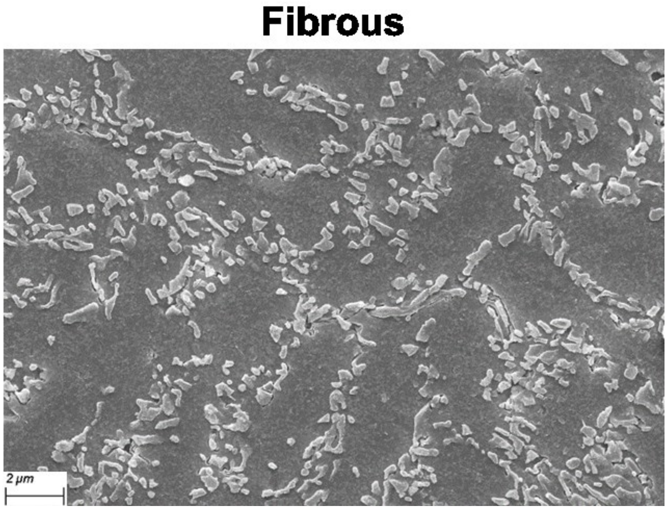

Figure 4-24: FE-SEM image of the "Fibrous" Si morphology. Ar 125-150µm sample.

The third grouping related to a “Globular + Fibrous” Si morphology, shown in Figure 4-25, which was a combination of rounded + non-elongated Si and sharp + elongated Si. This represented a transition morphology between the Globular Si and Fibrous Si.

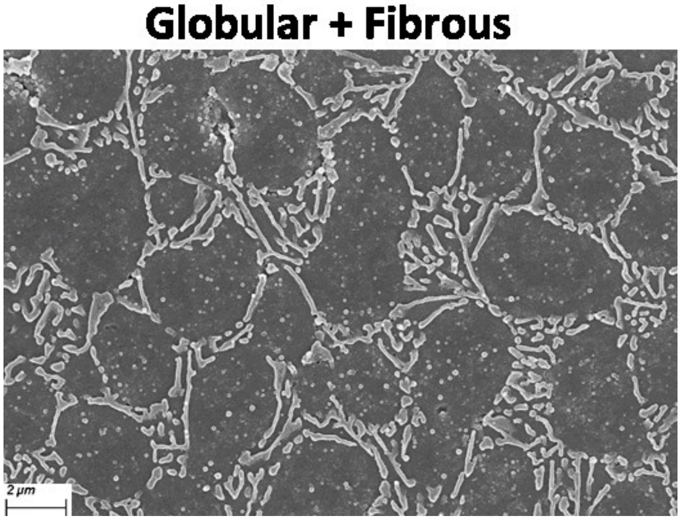

Figure 4-25: FE-SEM image of the "Globular + Fibrous" Si morphology. He 300-355μm sample.

While the fourth grouping related to a “Flaky” Si morphology, shown in Figure 4-26, where the Si was quite blocky, elongated and not rounded.

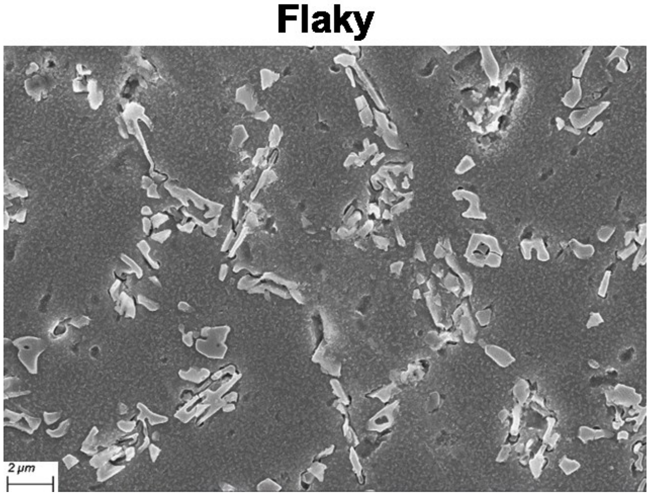

Figure 4-26: FE-SEM image of the "Flaky" Si morphology. Ar 300-355μm sample.

This qualitative analysis was done for each examined particle size range of the Al-10Si alloy, with 20 to 30 images being analyzed for each particle size range.

From the visual analysis, the globular type Si was ascribed as the most refined morphology, with the fibrous Si and the flaky Si being considered progressively less refined. This classification of the Si morphology was validated in Figure 4-27 where it was shown that the Si spacing would decrease as the morphology shifted from flaky → fibrous → globular + fibrous → globular. It shows that this qualitative Si morphology characterization was related to the local growth conditions of the eutectic structure.

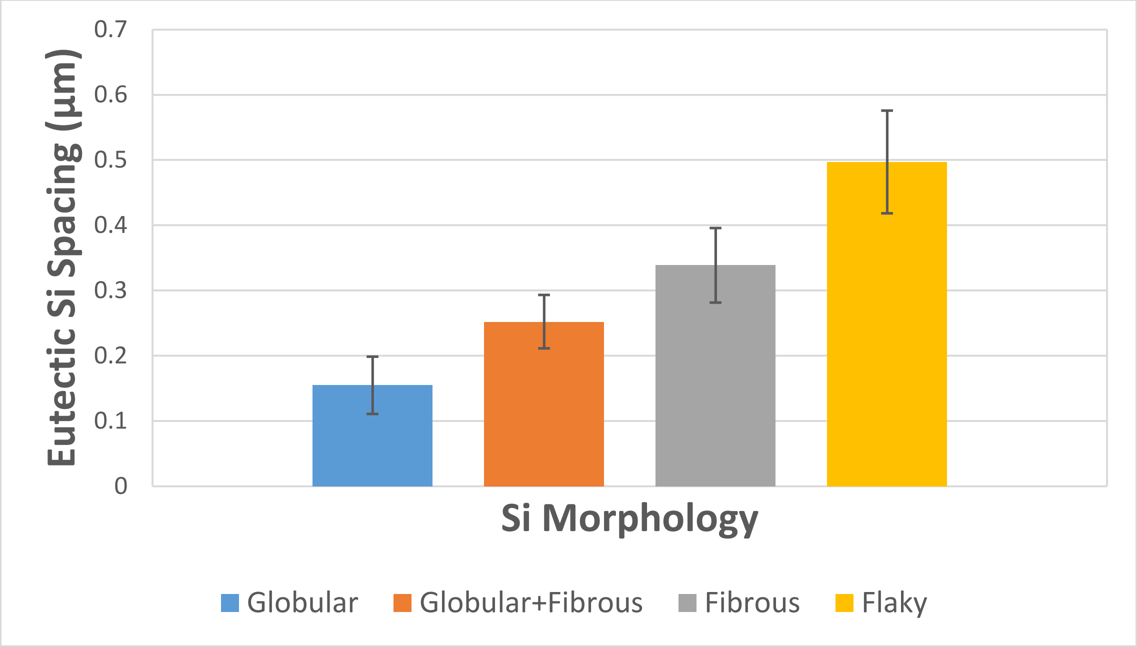

Figure 4-27: Average eutectic Si spacing for each 2D Si morphology grouping.

###### 4.4.1.1.1 Eutectic Si Morphology Distribution

The results from this 2D qualitative analysis were tabulated and plotted as pie charts, to provide a visual distribution of the Si morphology, as a function of the particle size. This was performed on the Al-10Si alloy that had been atomized in helium (Figure 4-28) and in argon (Figure 4-29).

From these figures we can see that as the particle size decreases there is a transition in the Si morphology from fibrous → globular, with an intermediate globular + fibrous morphology forming, too.

It was noted that there was a noticeable improvement in the refinement when using helium versus argon as the atomization gas. Amongst the three particle size ranges shared by the two atomization gases (212-250µm, 300-355µm and 355-423µm), the helium atomized powders had a larger portion of the Si morphology that was either globular or globular + fibrous.

The tabulation of the Si morphology indicated that the Si will become more refined as the particle size decreases, and when using helium instead of argon. This is consistent with previous results from Section 4.2.1.1, where similar trends were seen with respect to the eutectic nucleation undercooling.

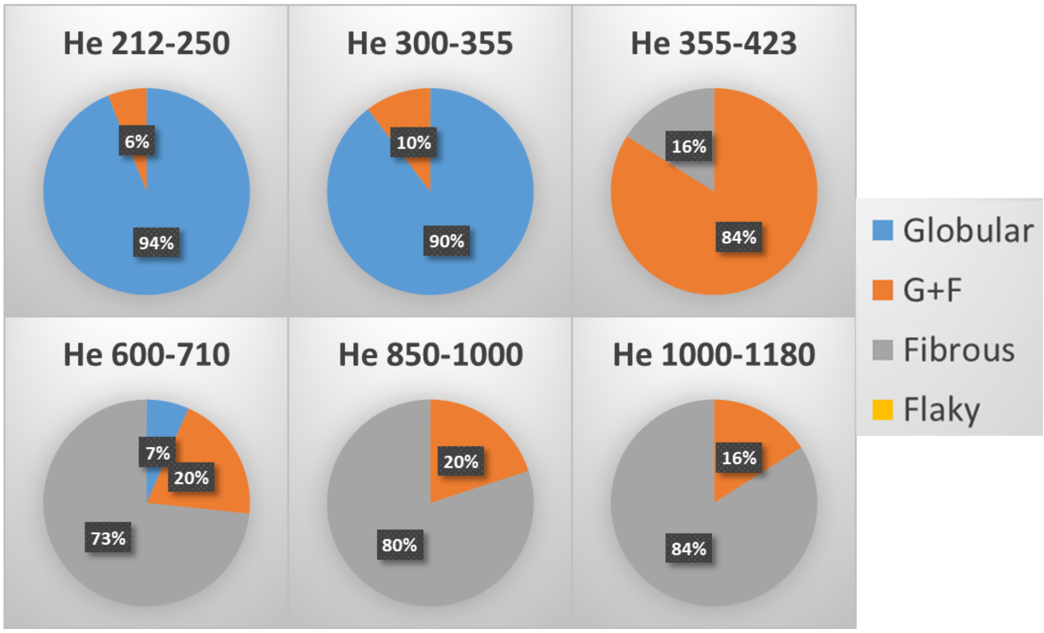

Figure 4-28: Breakdown of the 2D Si morphology, as a function of the particle size, for Al-10Si powders atomized in helium.

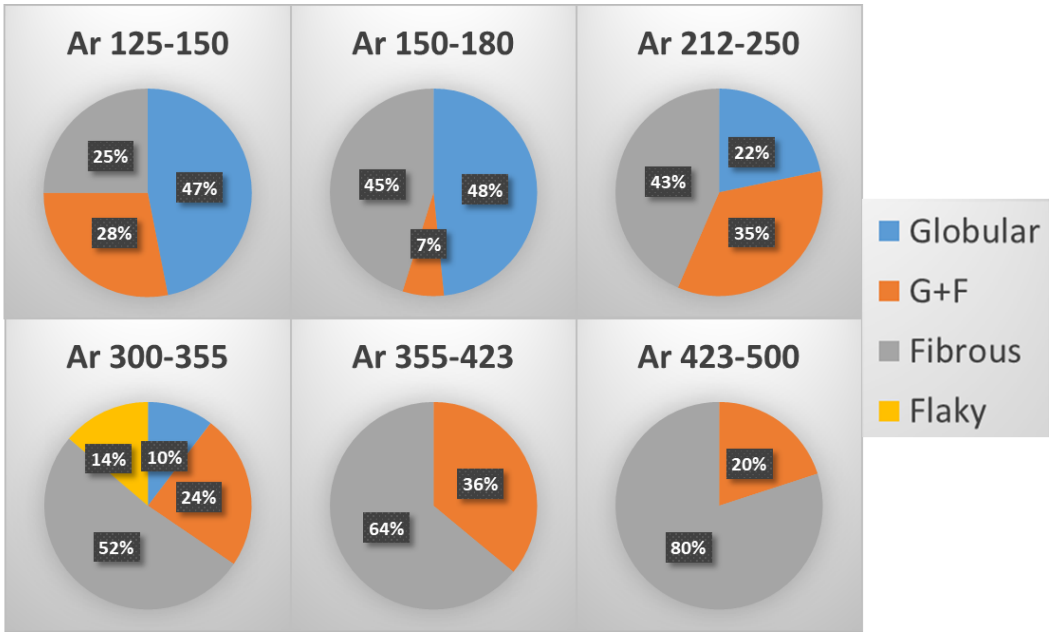

Figure 4-29: Breakdown of the 2D Si morphology, as a function of the particle size, for Al-10Si powders atomized in argon.

### 4.4.1.1.2 Eutectic Si Morphology and Eutectic Nucleation Point

The results from Section 4.4.1.1 were also used to determine the dominant Si morphology at the eutectic nucleation point. The location of eutectic nucleation was considered to be the region in the powder that had the smallest eutectic spacing, as the smallest eutectic spacing refers to the highest local eutectic growth rate and largest undercooling.

Between 4 to 6 powders were examined at each particle size, with 4 to 8 different locations being analyzed within each powder.

The criterion for the dominant Si morphology at the nucleation point was not solely based on what morphology had the most tallies and instead was based on the distribution of the tallies. For example, for the dominant Si morphology to be considered either globular or fibrous, all of the tallies had to be either globular or fibrous. If the tallies were split between various morphologies, then the dominant Si morphology was considered to be globular + fibrous, instead. This criterion was used due to the limited number of powders that were examined. As 4 to 6 powders were felt not sufficient to strongly propose that one morphology dominated, unless all tallies were of a specific morphology. The results are shown in Table 4-2.

Table 4-2: Dominant Si morphology at the point of nucleation, for each particle size.

| **He** | **212-250µm** | **300-355 µm** | **355-423 µm** | **600-710 µm** | **850-1000 µm** | **1000-1180 µm** |
|---|---|---|---|---|---|---|
| Globular | llll | llll | | ll | | |
| Globular/Fibrous | | | lllll | lll | ll | lll |
| Fibrous | | | | l | l | ll |
| Flaky | | | | | | |
| | ***Globular*** | ***Globular*** | ***G+F*** | ***G+F*** | ***G+F*** | ***G+F*** |
| **Ar** | **125-150 µm** | **150-180 µm** | **212-250 µm** | **300-355 µm** | **355-423 µm** | **423-500 µm** |
| Globular | llllll | lllll | llll | ll | | |
| Globular/Fibrous | | | l | ll | llll | lll |
| Fibrous | | l | | ll | l | lll |
| Flaky | | | | | | |
| | ***Globular*** | ***G+F*** | ***G+F*** | ***G+F*** | ***G+F*** | ***G+F*** |

From Table 4-2 a dominant globular morphology was seen only for the finest particle size atomized in argon and the two finest particle sizes atomized in helium. With the rest of the examined particle size ranges showing a dominant globular + fibrous morphology.

In terms of the experimental conditions, it was found that as the particle size became coarser the Si morphology would change from globular to globular + fibrous. This result was expected as greater refinement is expected as the particle size decreases. However, from these results there was not a clear influence of the atomization gas on the Si morphology. This is thought to be due to overlapping stages of the Si morphology transition [35], which makes it difficult to strongly distinguish between globular and fibrous morphologies.

#### *4.4.1.2 3D Si Morphology Analysis*

The second qualitative method involved the visual characterization of the Si growth morphologies using 3D images of the eutectic structure. To conduct this analysis SEM images of deeply etched eutectic microstructures were used in combination with a previous categorization of the 3D Si morphology from the work of Hosch et al. [35].

Hosch et al. [35] had categorized the lamella → rod Si transition into two distinct stages, an initial stage that involved the formation of Si rods from broken-up Si plates, along with a second stage that involved the onset of out-of-plane Si rod growth from in-plane Si rods.

Upon further examination it was found that this transition of the 3D Si morphology could be further subdivided into five smaller transitions that related to the shape of the eutectic Si. These five Si shape transitions are listed below, where the "refinement" of the morphology increases going from left to right:

Plates → Skeletal Plates → In-Plane Rods → Out-of-Plane Rods → Fibrous.

A schematic representation of these smaller transitions in the Si morphology is shown in Figure 4-30 using images of the eutectic from the work of Hosch et al. [35]. In this figure the first main stage of the lamella → rod transition occurs between the skeletal plate Si morphology and the in-plane rod Si morphology, while the second main stage of the lamella → rod transition occurs between the in-plane rod Si morphology and out-of-plane rod Si morphology.

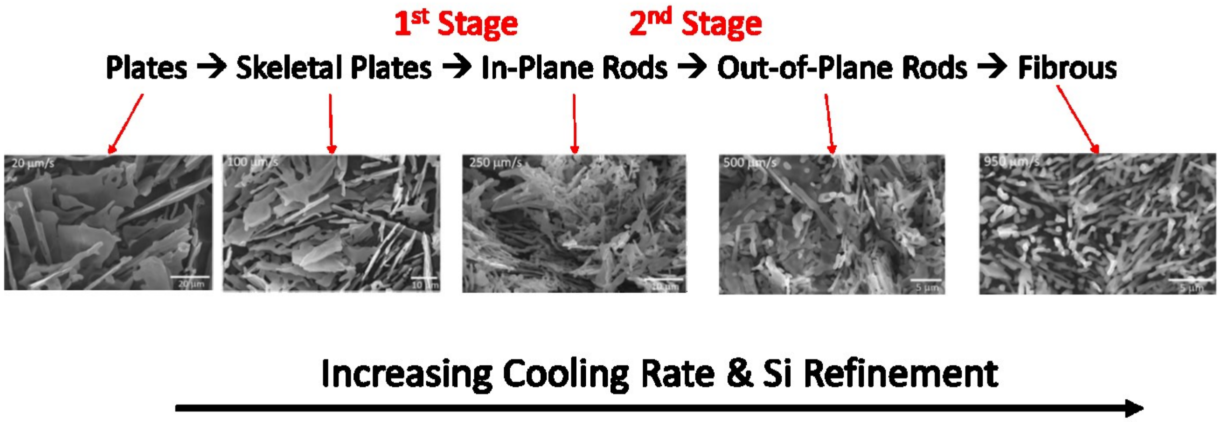

Figure 4-30: Transition of the 3D Si morphology, in an Al-13Si alloy, as a function of both cooling rate and Si refinement *[35]*.

Using these definitions, the Si morphologies of the IA Al-10Si alloy were categorized, where these categorizations was performed for all the examined particle sizes that were atomized in both helium or argon. For each particle size range between 8 to 10 images were examined.

From this 3D analysis, the 3D Si growth morphologies, of the IA Al-10Si alloy, were found to fall into three distinct groupings, based on the particle size and the atomization gas. These results are shown schematically in Figure 4-31.

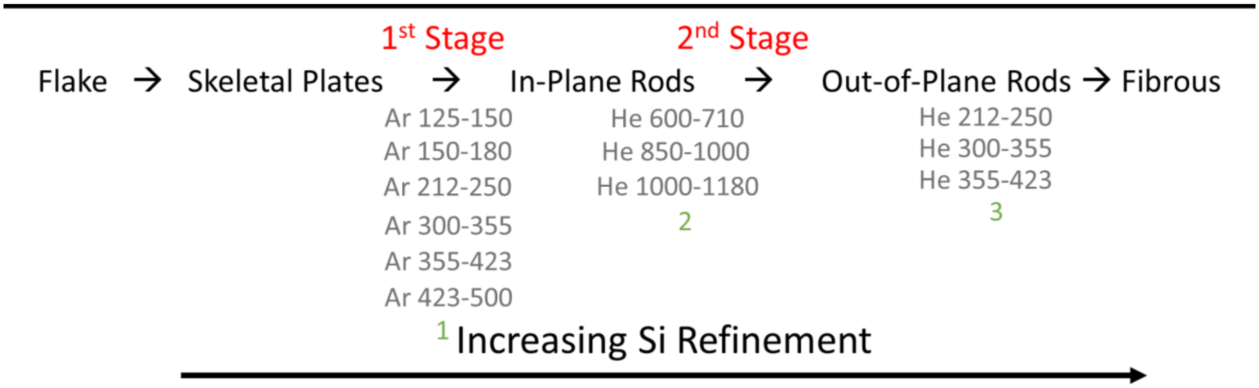

Figure 4-31: Classification of the 3D Si growth morphology, for the Al-10Si alloy, as a function of the particle size and the atomization gas.

The first grouping was the eutectic Si growth morphology that was seen in all the examined Al-10Si powders that were atomized in argon. In this grouping, a combination of skeletal Si plates and various in-plane Si rods was observed. This type of morphology indicates an Al-Si eutectic structure that was undergoing the first stage of the lamella → rod transition, where the Si plates were beginning to breakup into skeletal plates and in-plane rods. A characteristic example of this Si morphology grouping can be seen in Figure 4-32.

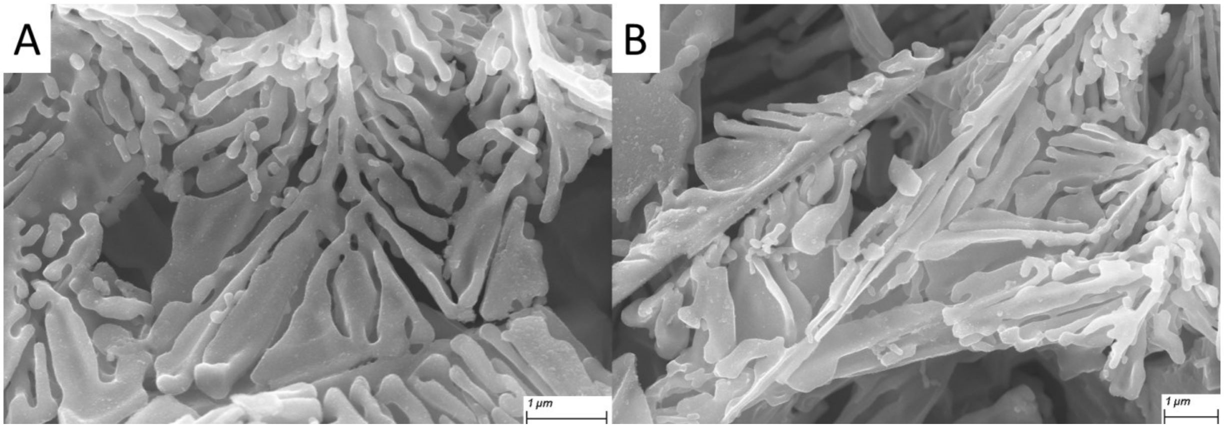

Figure 4-32: FE-SEM images outlining the characteristic Si morphology of the first stage of the lamella → rod transition. A) Formation of in-plane Si rods and elongated plates. B) Remnants of skeletal Si plates, along with some Si rods. Ar 125-150μm sample.

The second grouping of the eutectic Si morphology consisted of Al-10Si powders that were atomized in helium, specifically powders with particle sizes of 600-710μm, 850-1000μm and 1000-1180μm. Here the Si morphology primary consisted of in-plane Si rods, with occasional skeletal Si plates also being present. This morphology was indicative of an Al-Si eutectic that was still undergoing the first stage of the lamella → rod transition. However, it was noted that the system was on a cusp of reaching the second stage, where out-of-plane Si rod growth begins. A characteristic example of this Si morphology grouping can be seen in Figure 4-33.

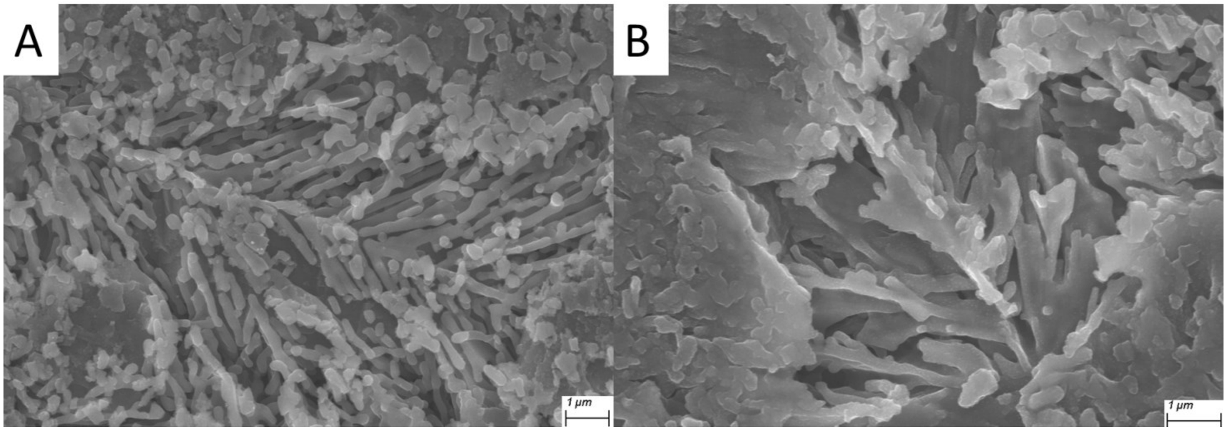

Figure 4-33: FE-SEM images outlining the characteristic Si morphology of the second 3D Si morphology grouping. A) Domination of in-plane Si rod growth. B) Presence of skeletal Si growth, showing that the Si has still not fully transformed into rods. He 1000-1180µm sample.

The third morphology grouping of the eutectic Si morphology consisted of the three finest particle size ranges that were atomized in helium. Specifically, the particle size ranges of 212-250µm, 300-355µm and 355-423µm. Here no skeletal plate growth of the Si was observed, as instead only rod like Si growth was observed. While most of this rod growth was in-plane, there were instances of out-of-plane growth or at least the onset of out-of-plane growth. This indicates that this Si morphology grouping was experiencing the onset of the second stage of the lamella → rod transition. A characteristic example of this Si morphology grouping can be seen in Figure 4-34.

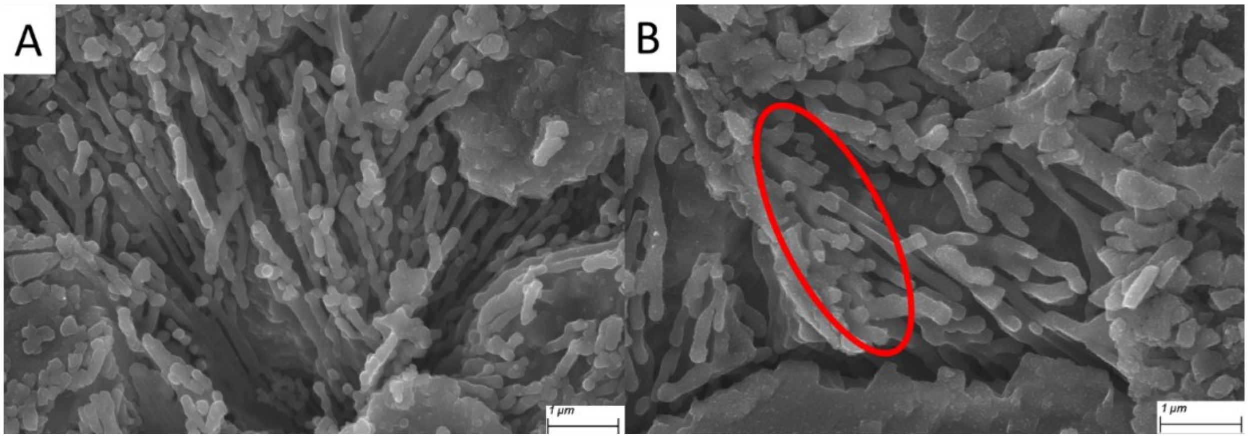

Figure 4-34: FE-SEM images outlining the typical Si morphology of the third 3D Si morphology grouping. A) Fully transformed Si rod growth. B) Highlighted region shows the onset of out-of-plane Si rod growth. Image A: He 300-355µm sample. Image B: He 355-423µm sample.

This 3D characterization indicated that the Si growth morphology will become more refined as the particle size decreases, and when helium is used instead of argon as the atomization gas.

Between the two experimental conditions, the atomization gas appears to play the dominant role. This is because every sample that was atomized in helium had a more refined Si morphology than the samples that were atomized in argon. Such a result is consistent with previous results from Section 4.2.1.1, where a dominating influence of the atomization gas was seen for the eutectic nucleation undercooling.

These findings also indicate that the lamella → rod transition of Si growth is gradual and occurs in slightly overlapping stages. This observation in in agreement with the previous work that has been performed on eutectic morphology transitions [35].

#### *4.4.1.3 Comparison of 2D vs. 3D Si Morphology Analysis*

In this section a comparison is made between the 2D and the 3D characterizations of the Si morphology, where the 2D Si morphology groupings were correlated to relevant 3D Si morphologies.

Examination of the "Globular" Si morphology, found that in 3D the Si was not globular at all. Instead, this globular morphology was a combination of in-plane and out-of-plane Si rod growth. It seems then that the 2D "Globular" designation is related to the thin and rounded nature of the Si rods themselves and not the overall structure. A visual comparison between the 2D and 3D growth morphology of the globular Si can be found in Figure 4-35A.

For the "Globular + Fibrous" Si morphology again no globular type of Si was observed in 3D. Instead, the globular + fibrous morphology was observed to be a combination of thin Si rods and elongated skeletal Si plates. It appears that the 2D morphology was again related to the thickness of the Si arms, rather than the overall structure. A visual comparison between the 2D and 3D growth morphology of the globular + fibrous Si can be found in Figure 4-35B.

The "Fibrous" Si morphology designation was confirmed as accurate as there was both rod and fibrous Si growth observed in 3D. However, the Si morphology designation did not characterize the remnant skeletal plate structure of the Si, nor was it able to distinguish between the in-plane and out-of-plane rod growth of the Si. A visual comparison between the 2D and 3D growth morphology of the fibrous Si is presented in Figure 4-35C.

The last identified 2D Si morphology was a “Flaky” Si. While this morphology was rare (found only in the 300-355µm sample that was atomized in argon), this identified morphology designation was confirmed as accurate from the results of the 3D analysis, as the flaky 2D Si morphology represented a skeletal plate Si growth in 3D. A visual comparison between the 2D and 3D growth morphology of the flaky Si is presented in Figure 4-35D.

Overall, the 2D Si morphology is shown to be related to the size, thickness and spacing of the formed Si (whether it be rod or plate like), making the 2D characterization an adequate method to describe the morphological refinement of the Si phase. However, the 2D characterization cannot describe the overall structure of the Si, nor can it discern subtle transitions in the growth morphology. This deficiency means it misses some important stages of the lamella → rod transition. As such, it was found that a combination of the 2D and 3D analysis is necessary to provide the best overall characterization of the Si growth morphology.

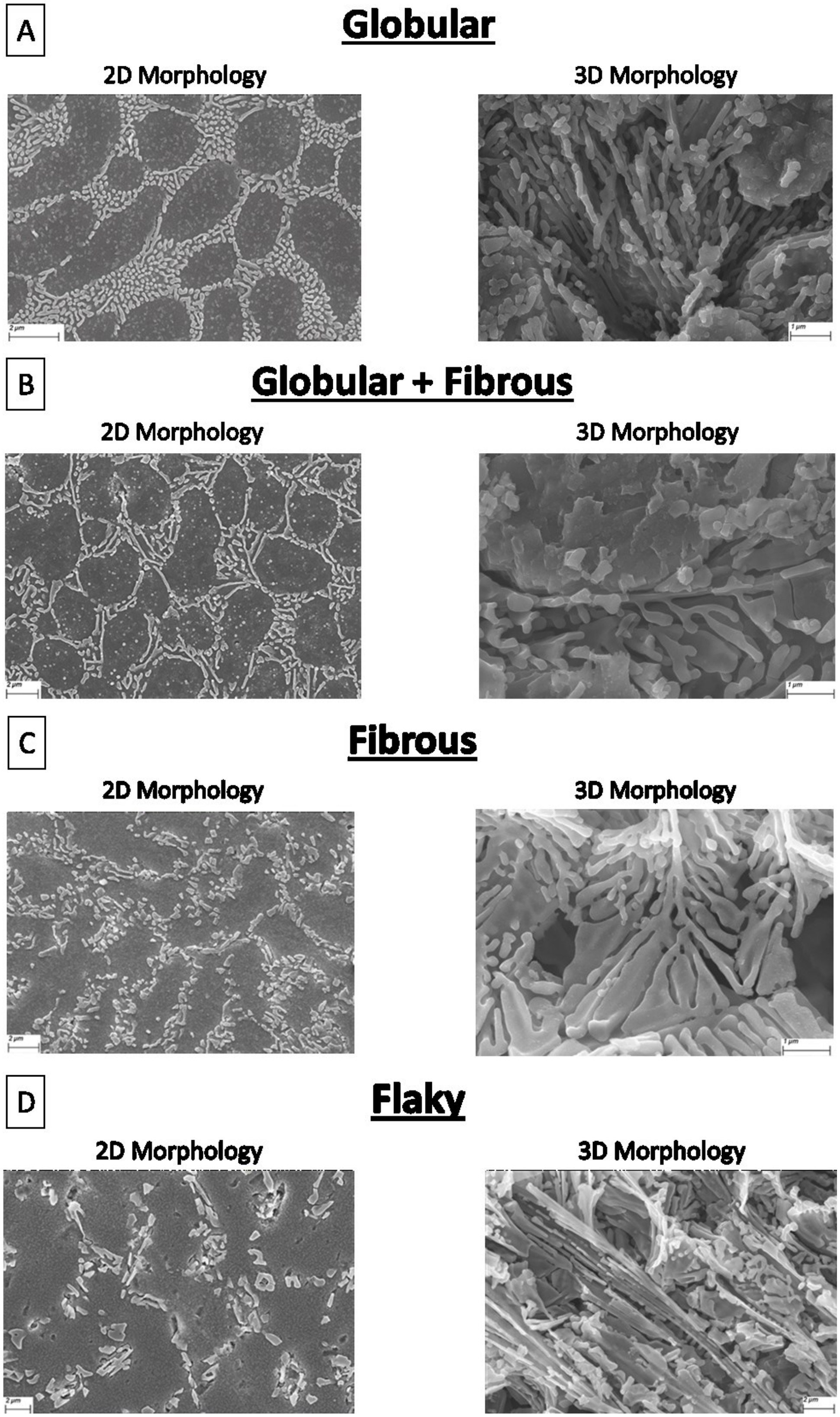

Figure 4-35: FE-SEM images comparing the 2D & 3D Si growth morphologies.

### 4.4.2 **Growth Conditions of the Eutectic Si Phase**

The qualitative characterization of the Si growth morphology, from Section 4.4.1, suggested that the local eutectic solidification conditions influenced the Si growth morphology. To evaluate this, methods were developed in to estimate the local eutectic solidification conditions. The estimation of these local eutectic solidification conditions is presented in this section.

#### *4.4.2.1 Local Growth Velocity & Undercooling*

The first set of local solidification conditions to be estimated were the local eutectic growth velocities and the local eutectic undercoolings.

Fundamentally, the growth of any eutectic is controlled by two main factors:

1. Solute diffusion, and,
2. Capillarity forces

These factors will determine the growth and spacing of the eutectic structure [76]. Using this knowledge Jackson & Hunt [77] developed the Jackson-Hunt model, which related the interphase spacing of the eutectic to various local solidification conditions. The developed Jackson-Hunt relationships are given below [28]:

$$\lambda_{eut}^{2} v^{*} = \frac{A_R}{A_C} D_l \tag{4-3}$$

$$\Delta T_{eut} = 2\sqrt{\frac{A_R A_C}{D_l}}\sqrt{v^{*}} \tag{4-4}$$

$$\lambda_{eut} \Delta T_{eut} = 2A_R \tag{4-5}$$

Where $\lambda_{ext}$ is the lamellar spacing of one of the eutectic phases, $v^{*}$ is the local eutectic growth velocity, $A_R$ & $A_C$ are material parameter constants, $D_l$ the diffusion coefficient of the liquid phase, and $\Delta T$ is the local eutectic undercooling.

While this proved to be a powerful tool, a limitation with this model was that it could only describe eutectic growth at low growth velocities. To solve this the Trivedi-Magnin-Kurz (TMK) model for eutectic growth was developed by Trivedi et al. [78]. This model took a more general approach to the solidification of the eutectic, allowing for theoretical predictions to be made at larger velocities. However, an issue with the TMK model was that it considers the maximum velocity, that can be experienced during eutectic growth, to be the velocity where non-equilibrium effects begin to take place at the solid-liquid interface. While this assumption is reasonable when examining the growth of regular eutectics, it is not accurate when describing the growth of irregular eutectics (like Al-Si). The reason is that these non-equilibrium effects at the S/L interface will heavily influence the formation and growth the eutectic structure if it is irregular.

As such, a model that could describe eutectic growth at high velocities, while also considering the non-equilibrium effects at the S/L interface, was required. A model that met these conditions was given in a paper by Gunduz et al. [79] in the form of a modified Jackson-Hunt approach. This modified model described eutectic growth using a solution of the solute diffusion equation where the boundary conditions accounted for the interfacial energies and the non-equilibrium effects at the S/L interface.

Moreover, this approach used a dimensionless parameter (φ) to describe the relationship of the various lamellae that form during irregular eutectic growth. Where φ was the ratio between the average and the extremum eutectic spacings and was used as an adjustment parameter. The calculation of this φ parameter (which is a dimensionless scalar based on the microstructure) can be seen below:

$$\varphi = \frac{\lambda_a}{\lambda_e} = \frac{\lambda_m + \lambda_M}{2\lambda_e} \qquad (4\text{-}6)$$

Where the $\lambda_a$ is the average spacing of the eutectic, $\lambda_e$ is the extremum spacing and the $\lambda_m$ and $\lambda_M$ represent the minimum and maximum spacings respectively. A schematic example of these spacings can be seen Figure 4-36.

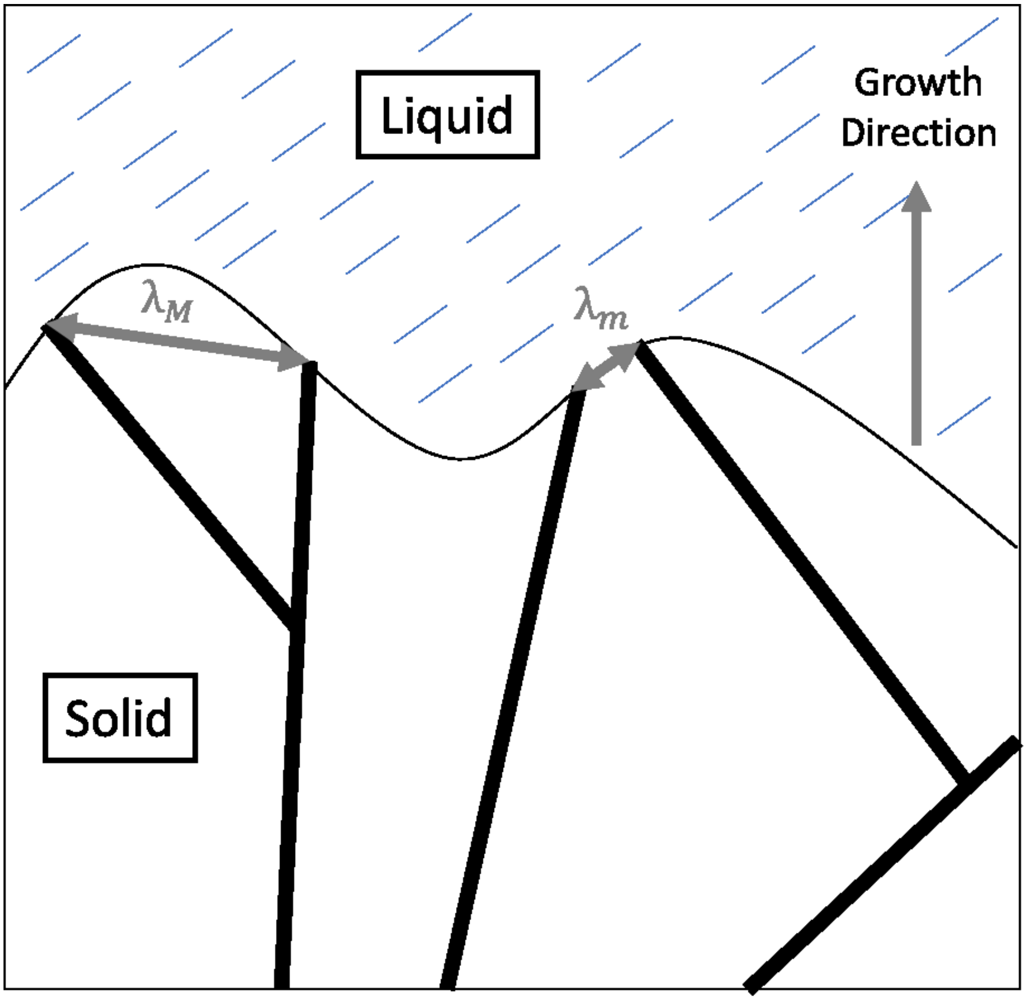

Figure 4-36: Schematic outlining the irregular eutectic growth in Al-Si. The black regions represent the Si phase and the white regions represent the Al matrix. $\lambda_m$ shows the disappearance of Si lamellae while $\lambda_M$ shows the branching of Si lamellae.

With this modified Jackson-Hunt model the local undercooling and growth velocity of the eutectic could be described, using equations below:

$$\Delta T_{eut} = (1+\varphi^2)\frac{K_2}{\lambda} \tag{4-7}$$

$$v^* = \frac{K_2\varphi^2}{K_1\lambda^2} \tag{4-8}$$

$$K_1 = \left(\frac{mC_o}{D}\right)\left(\frac{P}{f_\alpha f_\beta}\right) \quad \& \quad K_2 = 2m\left(\frac{\Gamma_\alpha \sin\theta_\alpha}{f_\alpha m_\alpha} + \frac{\Gamma_\beta \sin\theta_\beta}{f_\beta m_\beta}\right) \tag{4-9}$$

Where P is a function of the volume fractions ($P = 0.335(f_\alpha f_\beta)^{1.65}$) and the $K_1$ & $K_2$ are material parameter constants. The values and names of each of the used material properties for $K_1$ and $K_2$ can be found in Table 4-3.

Table 4-3: Data used for the modified Jackson-Hunt calculations *[61] [79] [80]*.

| Parameter Symbol | Parameter Value | Unit | Parameter Name |
|---|---|---|---|
| $\boldsymbol{D}$ | 4.3E-09 | $m^2s$ | Diffusion Coefficient |
| $\boldsymbol{C_o}$ | 87.7 | $wt\%$ | Length of weighted eutectic tie-line |
| $\boldsymbol{m_\alpha}$ | 7.5 | $K.wt\%$ | α-phase liquidus slope |
| $\boldsymbol{m_\beta}$ | 17.5 | $K.wt\%$ | β-phase liquidus slope |
| $\boldsymbol{\Gamma_\alpha}$ | 1.96E-07 | $K.m$ | Gibbs-Thompson coefficient α |
| $\boldsymbol{\Gamma_\beta}$ | 1.70E-07 | $K.m$ | Gibbs-Thompson coefficient β |
| $\boldsymbol{\theta_\alpha}$ | 30 | θ | Angle of α-phase |
| $\boldsymbol{\theta_\beta}$ | 65 | θ | Angle of β-phase |
| ***Teut*** | 850.2 | $K$ | Eutectic temperature |
| ***Ceut*** | 0.126 | ~ | Eutectic composition |
| $\boldsymbol{\Phi}$ | 2.3 | ~ | Extremum condition parameter |
| $\boldsymbol{f_\alpha}$ | 0.873 | ~ | α-phase fraction |
| $\boldsymbol{f_\beta}$ | 0.127 | ~ | β-phase fraction |

To validate this modified Jackson-Hunt approach the results were compared to past work with Al-Si alloys. This comparison involved a plotting of the eutectic Si spacing versus the local growth velocity and is shown in Figure 4-37. By examining this figure, it was found that the results for the IA Al-10Si alloy match well with the previous work with Al-Si alloys, as similar trends between the Si spacing and the local growth velocity were observed.

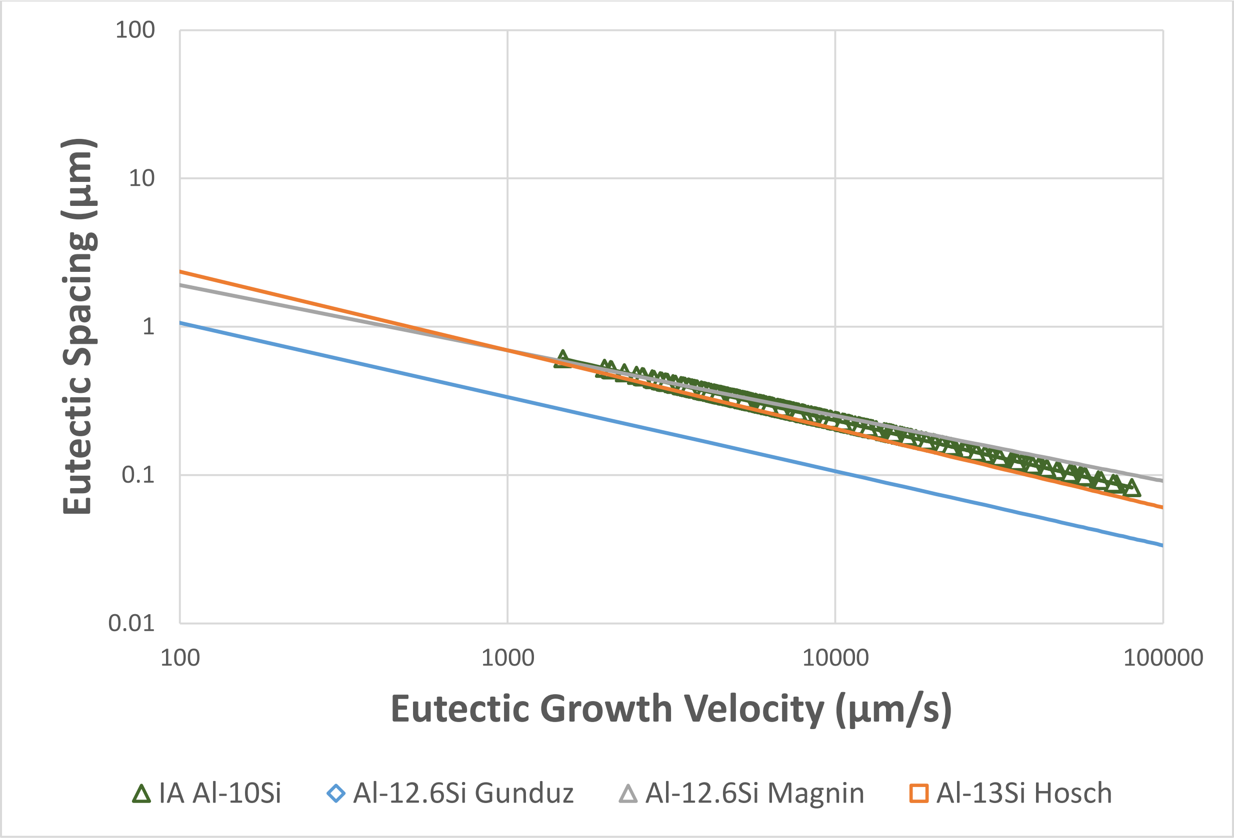

Figure 4-37: Validation of the modified Jackson-Hunt approach through the comparison of the Si spacing versus eutectic growth velocity relationship *[35] [79] [80]*.

#### *4.4.2.2 Local Eutectic Cooling Rate & Thermal Gradient*

The second set of local solidification conditions to be estimated were the local eutectic cooling rates and local eutectic thermal gradients.

This estimation relied on a previously developed thermal analysis by Garcia et al. [81]. That described the 1D unidirectional solidification of metal castings and involved a thermal energy balance at the solidification front that described the displacement and transport of heat. For the model Garcia neglected the influence of convection, the changes in volume due to differing densities and superheat in the liquid.

To better relate this analysis to what is observed in IA, Spinelli et al. [82] extended it to radial coordinates (from Cartesian) to better describe the solidification of a spherical powder. The derived expression from the modified thermal analysis is shown below:

$$k_t \left(\frac{dT}{dr}\right)_{r=r_f} = L\rho_L \left(\frac{dr_f}{dt}\right) \tag{4-10}$$

Where k is the thermal conductivity of the liquid, L is the latent heat of fusion, $\rho_L$ is the density of the liquid, dr is the incremental solid layer as solidification advances and $r_f$ is the radius of the freezing solidification front [82].

The right-hand side of this thermal analysis equation represents the latent heat given off by the portion of the solidification front that freezes. This heat must be balanced by the conductive heat transfer at the front (left-hand side of the equation) for solidification to proceed. A schematic of this thermal balance is shown in Figure 4-38 from work of Spinelli et al. [82].

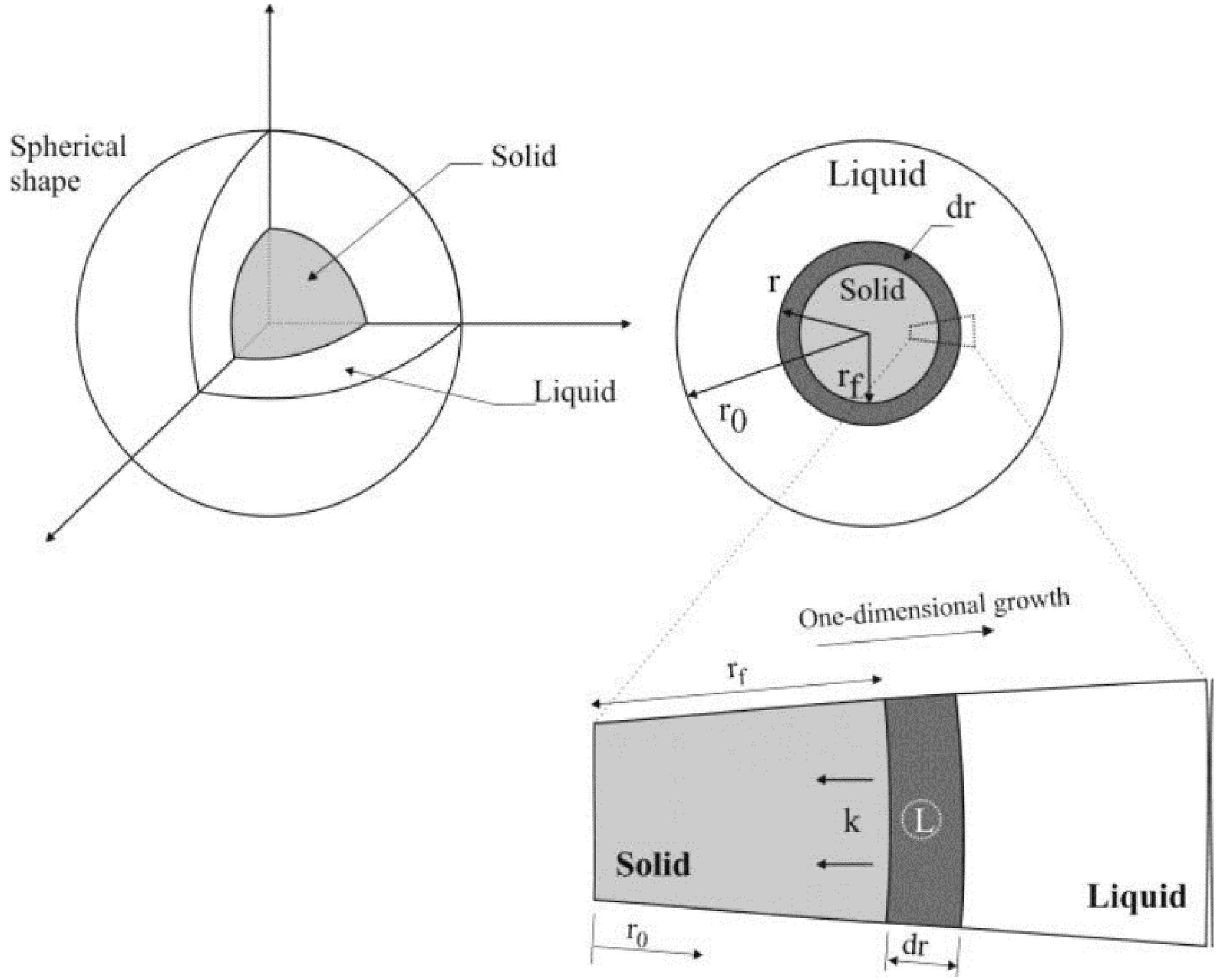

Figure 4-38: Schematic representation of the 1D thermal energy balance at the eutectic solidification front, in radial coordinates *[82]*.

Examining Equation 4-10 the $\left(\frac{dT}{dr}\right)_{r=r_f}$ term can also be expressed as the local thermal gradient ($G_{eut}$), while the $\left(\frac{dr_f}{dt}\right)$ term, can be expressed as the local growth velocity ($v^*$). Using these definitions, the thermal balance may be re-written as:

$$k_L G_{eut} = Ldv^* \tag{4-11}$$

Based on Equation 4-11 a relationship between the eutectic growth velocity and the eutectic cooling rate ( $CR_{eut} = G_{eut}v^*$) can be made:

$$CR_{eut} = C_1 {v^*}^2 \tag{4-12}$$

$$C_1 = \frac{L\rho_L}{k_L} \tag{4-13}$$

Where $CR_{eut}$ is the local eutectic cooling rate and $C_1$ is a material constant parameter.

Using Equation 4-12 the local eutectic cooling rate can be estimated with the local growth velocity and the material constant parameter $C_1$. This $C_1$ was calculated using the Al-10Si material properties from Table 4-4.

Table 4-4: Al-Si material properties used for eutectic cooling rate estimation *[83]*.

| Parameter Symbol | Parameter Value | Unit | Parameter Name |
|---|---|---|---|
| $\boldsymbol{L}$ | 397300 | $J.Kg$ | latent heat of fusion |
| $\boldsymbol{\rho_L}$ | 2650 | $Kg.m^{-1}$ | density of the liquid |
| $\boldsymbol{k_L}$ | 70 | $W.m^{-1}K^{-1}$ | thermal conductivity of the liquid |

To determine if $C_1$ accurately related the eutectic cooling rate to the growth velocity Reyes et al. [84] experimentally determined the $C_1$ by fitting a $CR_{eut}$ versus ${v^*}^2$ plot [82]. From this fit it was found that the experimentally determined $C_1$ was $1.6\ x\ 10^7 Ksm^{-2}$, which was in good agreement with the theoretical value of $1.5\ x\ 10^7 Ksm^{-2}$ [64]. This indicates that the material constant parameter, $C_1$, can accurately describe the relationship between the eutectic cooling rate and the eutectic growth velocity.

The estimation of the eutectic cooling rate also permitted an estimation of the local thermal gradient. This can be done by rearranging Equation 4-12 to make it in terms of the $G_{eut}$:

$$G_{eut} = \frac{v^*}{CR_{eut}} \tag{4-14}$$

### 4.4.3 Al-10Si Eutectic Growth Map

With the developed methods from Sections 4.4.1 and 4.4.2 it was now possible to map the transitions in the Si morphology, as a function of the local eutectic solidification conditions. For this mapping, the Si morphology was plotted as a function of the local growth velocity, and the inverse local thermal gradient. These axes were chosen as perpendicular lines on this plot would represent the local eutectic cooling rate, making it possible to clearly quantify the transitions in the Si morphology. The eutectic growth map for the Al-10Si alloy can be seen in Figure 4-39.

In Figure 4-39, it was found that the local solidification conditions of the eutectic determine the Si morphology, as the refinement of the Si morphology was found to improve as the $v^*$ and the $CR_{eut}$ increased. At high $v^*$ and $CR_{eut}$ a globular Si morphology would be induced, and as the $v^*$ and $CR_{eut}$ decreased the Si morphology would transition from globular to fibrous to flaky. The critical cooling rates for these transitions, from flaky → fibrous, fibrous → globular + fibrous and the globular + fibrous → globular, were at ~60 K/s, ~350 K/s, and ~1200 K/s respectively.

This growth map also examined the influence of the atomization gas on the Si morphology. When comparing the two gases it seems that while using argon can provide a refined globular Si, a larger proportion of the globular Si was made up of samples that were atomized in helium. This demonstrates that the atomization gas will influence the probability that a particular eutectic morphology will form.

Overall, this eutectic growth map is a useful way to categorize the influence of eutectic solidification on the Si morphology, as transitions in the morphology can be related to specific local (and determinable) eutectic growth conditions.

The importance of understanding these transitions is discussed further in Section 4.5, where these shifts in morphology will be related to the mechanical properties of the Al-10Si alloy.

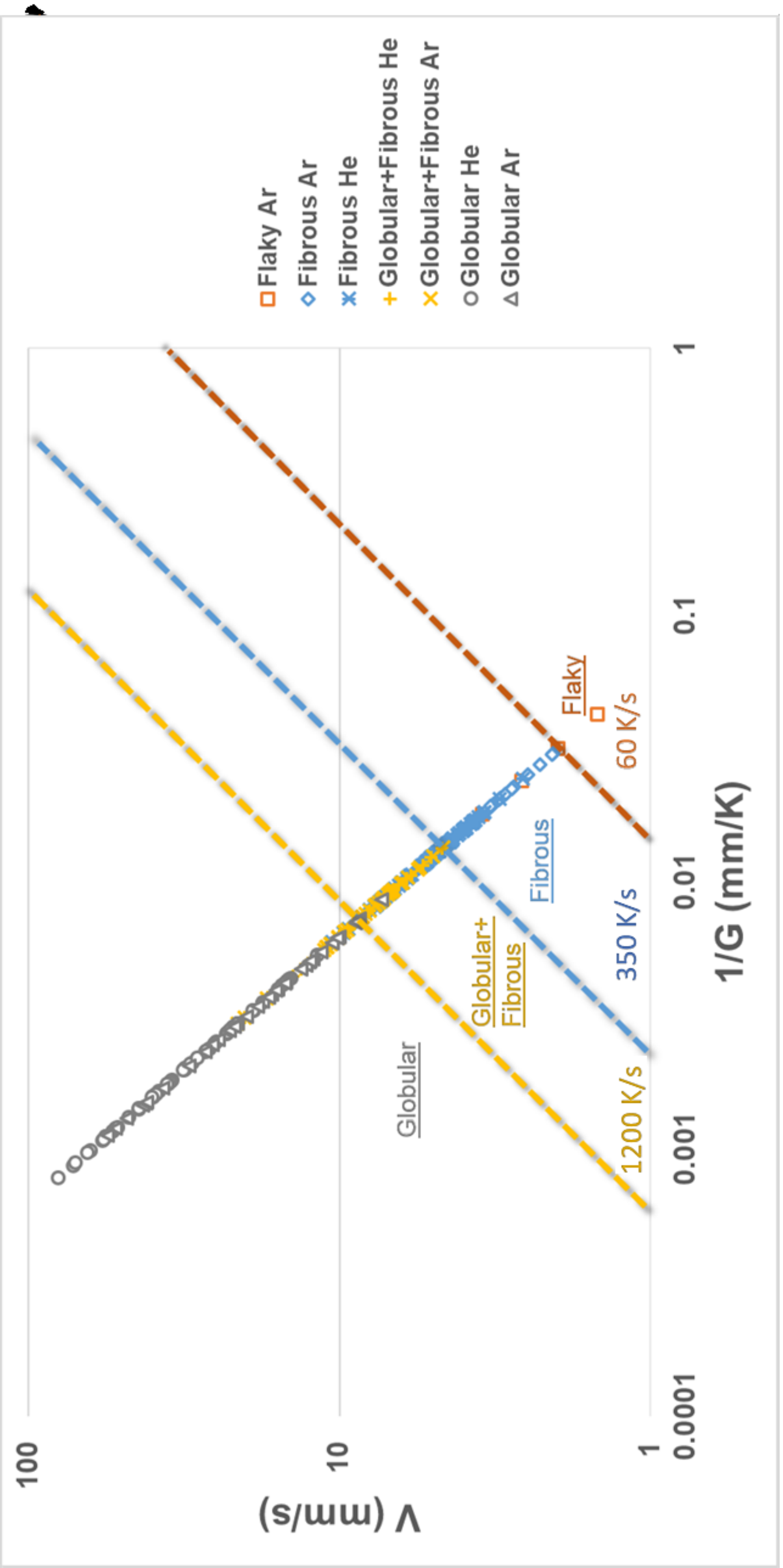

Figure 4-39: Al-10Si eutectic growth map.

## 4.5 INFLUENCE OF AL-10SI MICROSTRUCTURE ON HARDNESS

From Section 4.2.3, it was found that the experimental conditions of IA could not explain the variations in the hardness of the alloy and it was suggested that some other underlying factor caused this trend. It was thought that one possible cause for this variation could be the microstructure of the Al-10Si alloy. So, the previously quantified aspects of the microstructure were related to the hardness of the alloy to determine if they, influenced the mechanical properties. The results of this analysis is presented in this section.

### 4.5.1 **Influence of Microstructural Refinement**

The first aspect of the microstructure to be examined was the influence of microstructural refinement; specifically, the length-scale refinement of the α-Al phase and the eutectic Si phase.

### *4.5.1.1 Hall-Petch Relationship*

To determine if the refinement of either phase influenced the hardness of the alloy a method was developed that used a "Hall-Petch" type of relationship.

The Hall-Petch relation is used to describe the strengthening of a material as the grain size decreases [85]:

$$\sigma_y = \sigma_i + \frac{k_y}{\sqrt{D_g}} \qquad (4\text{-}15)$$

Where $\sigma_y$ is the yield strength, $\sigma_i$ is a materials constant for the starting stress for dislocation movement, $k_y$ is the strengthening coefficient and $D_g$ is the average grain diameter.

The defining characteristic of the Hall-Petch is the inverse linear relationship between the strength ($\sigma_y$) and the grain size ($D_g$).

In this work we use the Hall-Petch relation and attempt to expand its application from grain boundary strengthening to the strengthening of an Al-10Si alloy, related to the interphase spacing of both the α-Al and the eutectic Si phases.

If a clear inverse linear relationship was seen it could be inferred that this interphase spacing helped strengthen the material. However, if it was found that there was not an inverse linear relationship, then the interphase spacing could not be said to help strengthen the material.

#### 4.5.1.2 *α-Al Dendrite Cell Spacing*

Using the outlined "Hall-Petch" method the α-Al dendrite cell spacing measurements were compared to the alloy hardness in Figure 4-40.

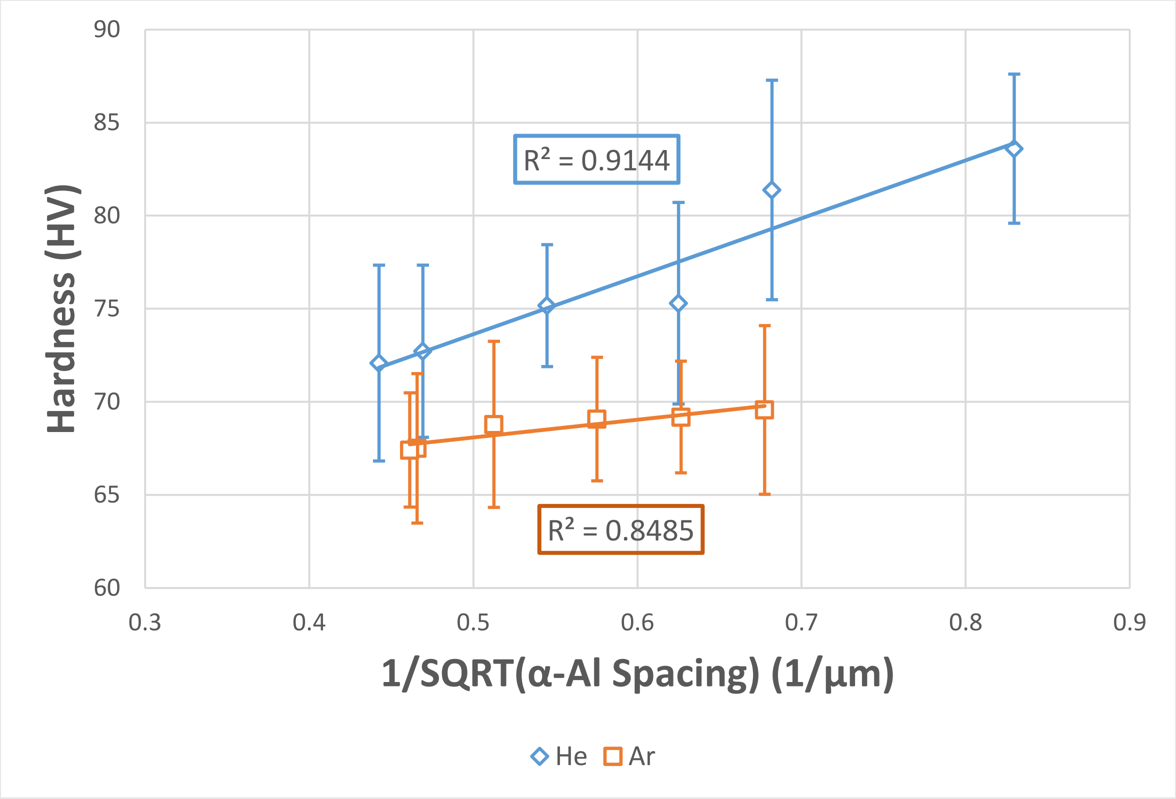

Figure 4-40: "Hall-Petch" type plot of the hardness and the α-Al dendrite cell spacing.

Examining this figure, a linear relationship between the hardness and the α-Al spacing is only observed when looking at the argon samples and the helium samples separately. If the two sets of data were combined this inverse linear relationship would not be present. This means that there is not a simple "Hall-Petch" relationship, indicating that a reduction in spacing of the α-Al phase, alone, cannot explain the variations in the measured hardness.

#### 4.5.1.3 *Eutectic Si Spacing*

Next the influence of the length-scale refinement of the eutectic structure was examined by comparing the eutectic Si spacing measurements to the hardness via the "Hall-Petch" relationship in Figure 4-41.

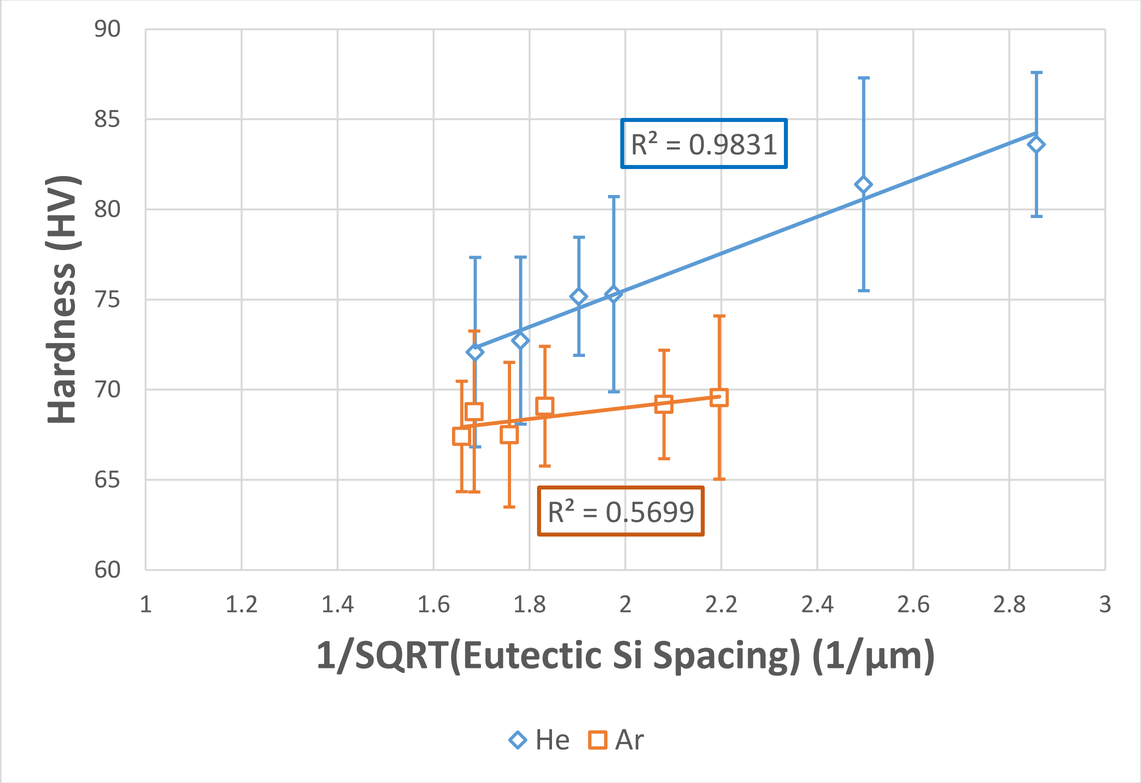

Figure 4-41: "Hall-Petch" type plot of the hardness and the eutectic Si spacing.

Examining this figure, a linear relationship between the hardness and the eutectic Si spacing is only observed when examining the argon samples and the helium samples separately. If the two sets of data were combined, then a simple inverse linear relationship does not occur. The result indicates that there is not a simple "Hall-Petch" relationship, indicating that a reduction in spacing of the eutectic Si, alone, cannot explain the variations in the measured hardness.

### 4.5.2 Influence of α-Al Morphology

With the length-scale refinement of each phases being ruled out the next factor to be examined was the influence of the α-Al morphology. This was done by determining the α-Al dendrite cell spacing as a function of the observed α-Al morphology. If the α-Al spacing, of each morphology, was similar then it could be inferred that the morphology did not play a role, as the results from Section 4.5.1.2 showed that the α-Al Spacing did not help strengthen the Al-10Si alloy. However, if the spacings were different, it would suggest that this morphology did in fact affect the hardness.

As outlined in Section 4.3 there were two α-Al growth morphologies, a <100> growth and a <110> growth. Since it was not possible to confirm the growth direction of every powder using EBSD, the classification of these morphologies was done visually using concepts of symmetry. For a morphology to be categorized as <100> growth a clear 4-fold symmetry had to be present, and for a morphology to be categorized as <110> growth a clear 6-fold symmetry was required. If either type of symmetry was not clear, then the morphology was considered to be a <100>/<110> growth morphology.

From this analysis it was found that α-Al morphology in the Al-10Si alloy could be categorized as either <100> or <100>/<110>. Using these groupings, the α-Al spacing was plotted as a function of the particle size, for both helium and argon samples, in Figure 4-42 and Figure 4-43 respectively.

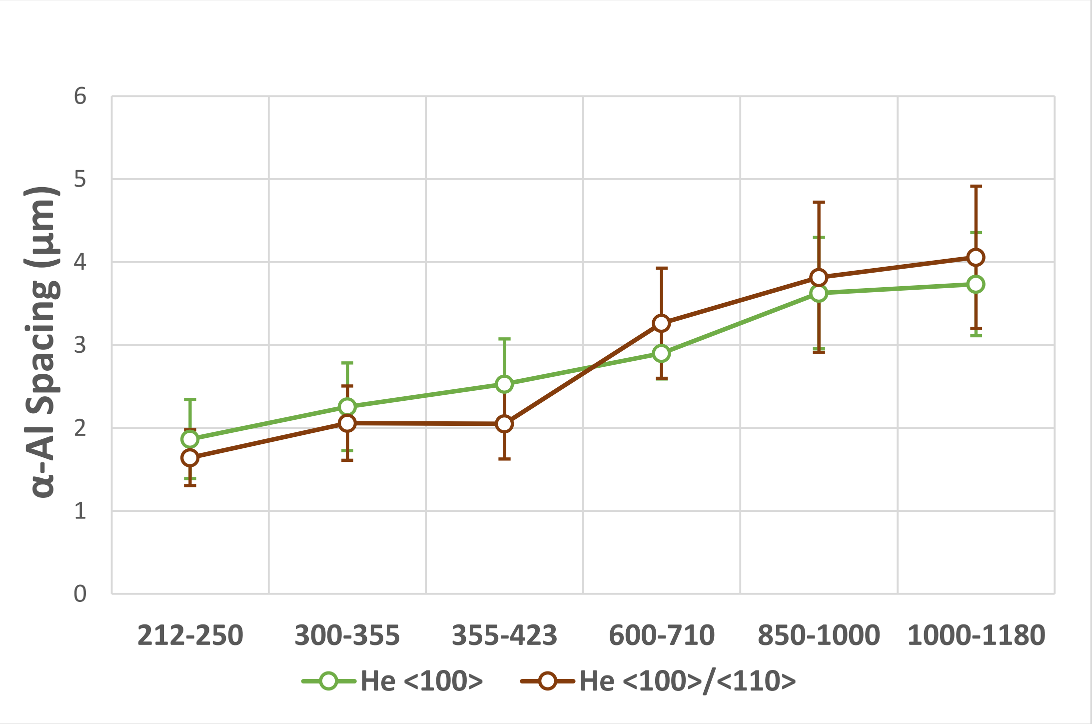

Figure 4-42: α-Al spacing and morphology for the helium IA Al-10Si alloy.

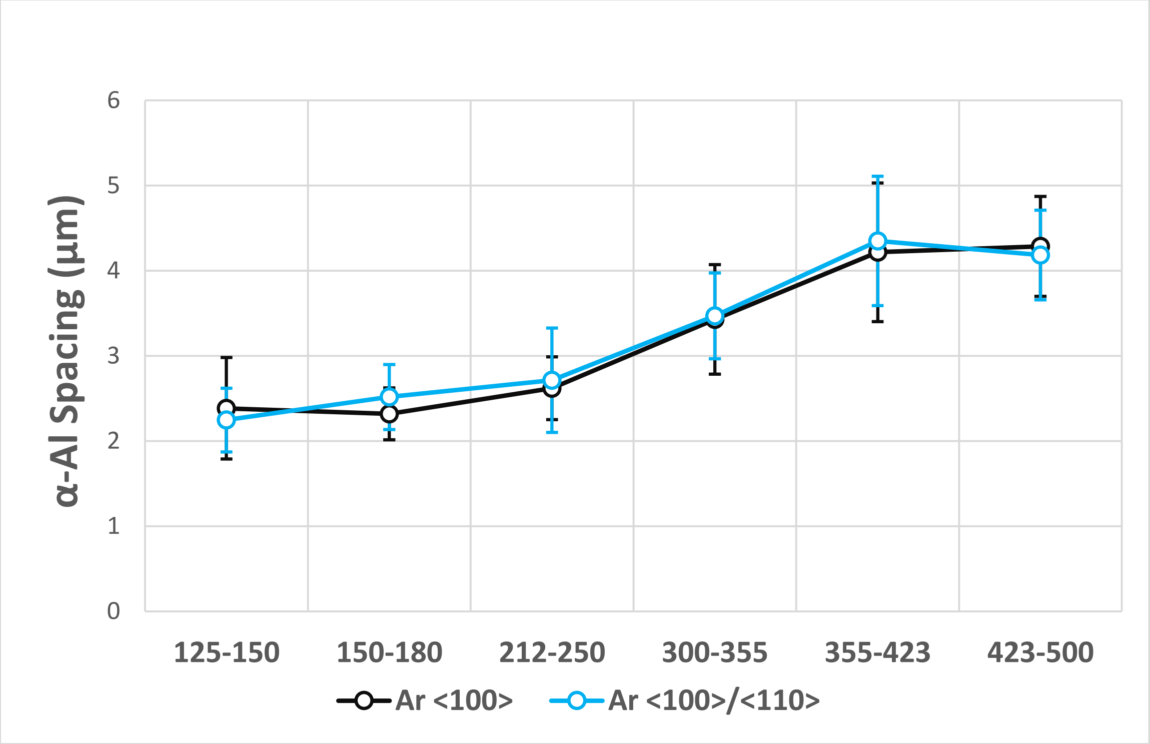

Figure 4-43: α-Al spacing and morphology for the argon IA Al-10Si alloy.

From either plot no discernable difference in α-Al spacing, between the two morphologies, was observed. This, coupled with the results from Section 4.5.1.2, suggest that the α-Al morphology does not influence the hardness of the Al-10Si alloy.

### 4.5.3 **Influence of Eutectic Si Morphology**

With the other aspects of the Al-10Si microstructure proving inconclusive, this left the Si growth morphology as the last remaining characteristic. While this was the case it was difficult to directly relate the Si morphology to the hardness, since the hardness measurements were macro in scope and could measure the hardness of specific regions or morphologies. So, an initial correlation had to be made, with some factor, before the hardness could be related to the Si morphology.

The most reasonable factor to do this with was the eutectic nucleation undercooling, as it precluded eutectic growth and acted as a driving force for its solidification. This influence of the eutectic undercooling on the Si growth morphology had been found in previous work by Prukkanon et al. [67]. and Zhang et al. [86] where they mentioned that the modification of the Al + Si eutectic structure was achieved only after a sufficient amount of undercooling.

To conduct this comparison the eutectic nucleation undercooling was plotted as a function of the hardness in Figure 4-44.

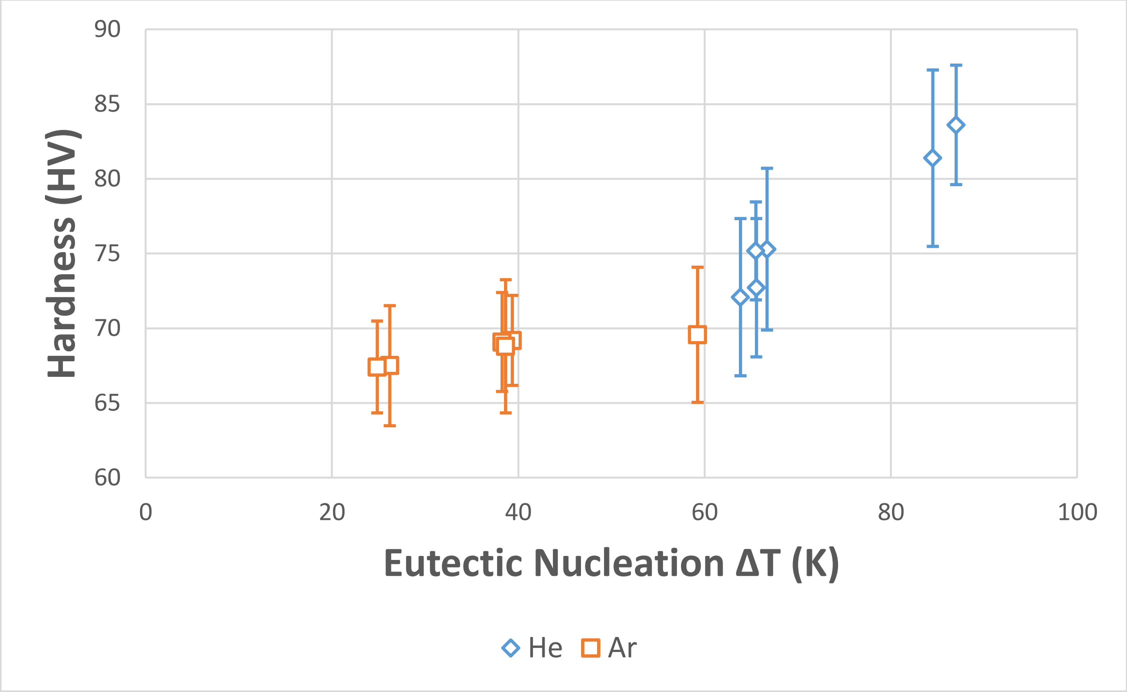

Figure 4-44: Vickers hardness as a function of the eutectic nucleation undercooling.

Examining Figure 4-44, a clear trend is observed. Where an increase in the eutectic nucleation undercooling leads to an increase in the hardness. This indicates that the eutectic nucleation undercooling seems to influence the hardness of the Al-10Si alloy.

However, a further examination of Figure 4-44 brings up some questions regarding this trend. One question is: "Why is there an initial plateau in the relationship where increases in undercooling do not improve the hardness?" Conversely. "Why is there a sudden jump in the hardness after a certain amount eutectic undercooling?" These questions suggest that there might be another underlying cause(s).

The remaining microstructural feature that still needed to be related to the hardness was the Si morphology. So, it was proposed that there might be a relationship between the eutectic undercooling, the Si growth morphology and the hardness. To see if this was the case these factors were combined by overlaying the dominant Si morphology from Table 4-2 onto Figure 4-44. This combined figure is shown in Figure 4-45.

Before moving on to Figure 4-45 the dominant 2D Si morphology of the Ar 125-150µm sample needs to be discussed. In Table 4-2 the dominant morphology of that sample was tabulated as globular. However, from analysis of the 3D Si morphology this sample's morphology was found to be substantially less refined than the other 2D globular morphologies. Therefore, in Figure 4-45 this Ar 125-150µm sample was not considered to be globular and was instead considered to be globular + fibrous.

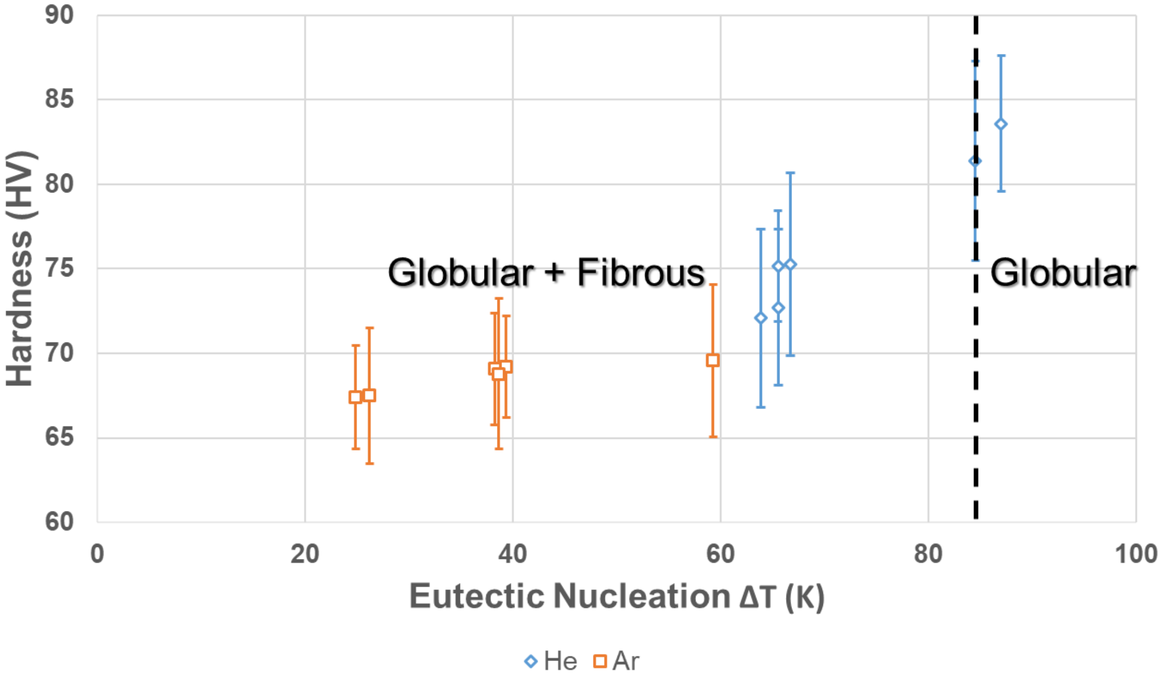

Figure 4-45: Influence of eutectic nucleation undercooling and 2D Si morphology on the Al-10Si alloy hardness.

In Figure 4-45 an underlying cause for the variations in hardness is perhaps clarified, as variations were found to be a function of the Si growth morphology; even though this growth morphology was not continuous in nature (which suggests that other strengthening mechanisms may be present and associated with the morphology changes).

It was noted that the highest hardness was achieved when the Si morphology was predominantly globular. And if this Si morphology became less refined, a noticeable reduction in the hardness was observed. This result demonstrated that the Si morphology is a very important factor that affects the hardness of the IA Al-10Si alloy.

Figure 4-45 also highlights the inadequacy of using a “length-scale” definition to describe the refinement of the eutectic structure. In the examined Al-10Si alloy, even though the Si interphase spacing was between 150nm to 400nm, a slight shift in the morphology noticeably affected the hardness, as the shift to a globular Si morphology improved the hardness by up to 24%. This result indicates that a length-scale definition of microstructural refinement cannot not adequately explain all improvements in the mechanical properties, and that the morphology of the phase must also be seriously considered.

## 4.6 WHAT PROCESSES CAN MODIFY THE EUTECTIC SI MORPHOLOGY?

In Section 4.5 it was found that the Si growth morphology was an important microstructural feature that affected the hardness of the Al-10Si alloy. While the transition in the Si morphology had been previously mapped, as a function of the local eutectic cooling rate, this eutectic cooling rate is not a directly controllable aspect during melt processing, as it is a function of both the growth velocity and the thermal gradient. While this cooling rate is not directly controllable, various processing techniques can impose different growth velocities and thermal gradients, making them somewhat controllable. With this in mind, a new mapping of the Si morphology was conducted in terms of these local eutectic growth conditions.

The goal of this mapping was to identify the specific local solidification conditions that brought about the globular Si morphology and to use these identified conditions to determine what production methods could achieve this morphology. This mapping of the Si morphology via the local eutectic growth velocity and the local eutectic thermal gradient are given in Figure 4-46 and in Figure 4-47 respectively.

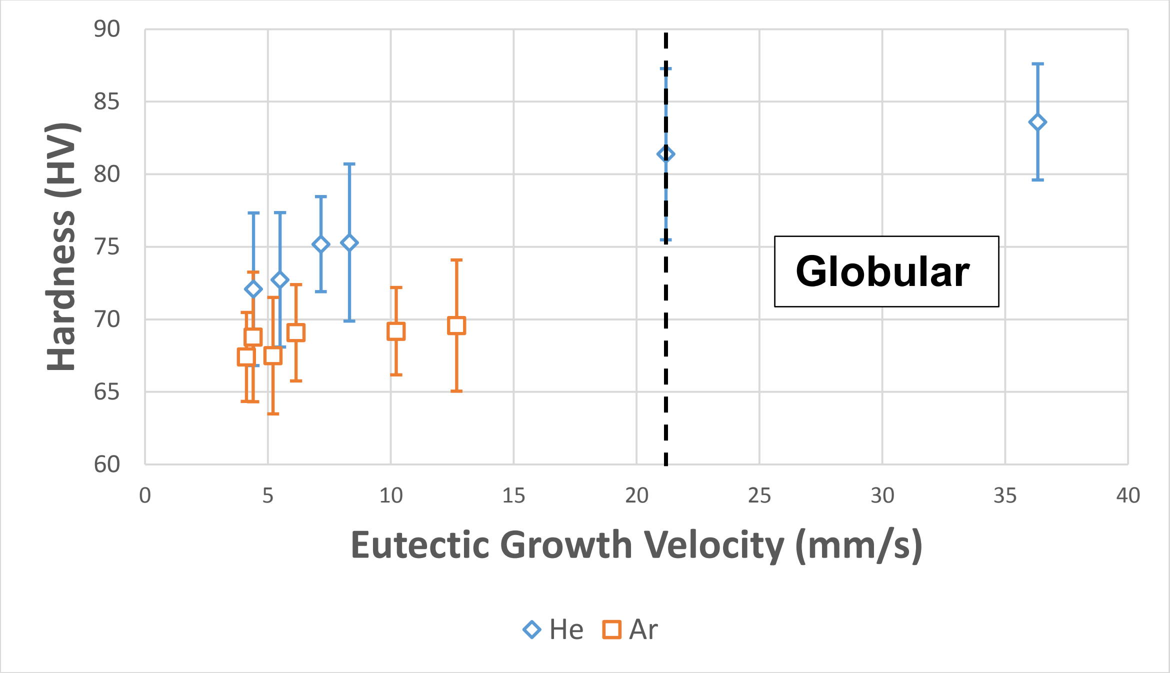

Figure 4-46: Influence of the local eutectic growth velocity on the Si morphology and the hardness of the Al-10Si alloy

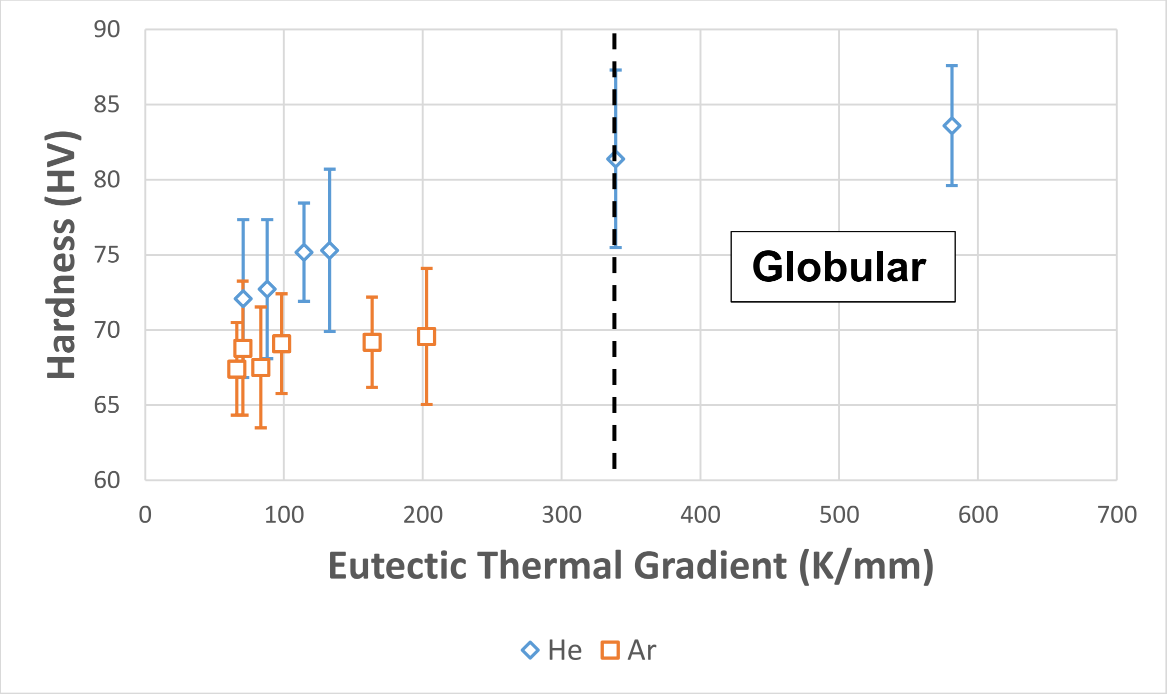

Figure 4-47: Influence of the local eutectic thermal gradient on the Si morphology and the hardness of the Al-10Si alloy.

Examining Figure 4-46 and Figure 4-47, relatively large local eutectic growth velocities (~20 mm/s) and large local eutectic thermal gradients (~300 K/mm) are required for the desired globular Si morphology to form.

Using conventional casting processes (like shape, die, & sand casting), these growth velocities and thermal gradients are not possible. As typically, these casting processes can only achieve macro growth velocities of ~10 mm/s [87] [88] [89] and macro thermal gradients of ~10 K/mm [89].

Although conventional casting cannot reach these required solidification conditions, it was found that other processes can, specifically additive manufacturing. In additive manufacturing macro growth velocities of up to ~1000 mm/s and macro thermal gradients of up to ~1000 K/mm are possible [90] [91]. Given that this morphology is the key to improving the mechanical properties, this work recommends that additive manufacturing facilities should adjust their process conditions to invoke this globular Si morphology in hypoeutectic Al-Si alloys.

While the mapping done in this section only examined the local solidification conditions of the eutectic it is a straightforward means to identify what processes can achieve the desired solidification conditions/morphology. Extending this analysis out to describe more macro solidification conditions of the Al-10Si alloy should be conducted in future work.

# 5 CONCLUSIONS

In this work a rapidly solidified Al-10Si alloy, produced by Impulse Atomization, was analyzed. Here it was observed that the Al-10Si alloy had the expected two-phase microstructure; consisting of a primary α-Al phase and a secondary Al + Si eutectic structure. However, the morphology of these phases (particularly the Si eutectic) was found to noticeably shift as the solidification conditions changed.

The growth of the primary α-Al phase was found to have two distinct growth directions: a <100> growth and a <110> growth. In addition, the formation of a “seaweed” α-Al structure was observed. The transition in growth from <100> to <110>, along with the propensity for seaweed growth, was found to become more prominent as solidification became more rapid. Suggesting that rapid solidification led to the observed shifts in the α-Al morphology and that atom attachment kinetics may be playing a role during this transition.

With respect to the secondary Al + Si eutectic structure, a characterization of the 2D and the 3D Si growth morphologies was conducted.

The 2D characterization sub-divided the Si morphology into four groupings: flaky, fibrous, globular + fibrous and globular; where the globular morphology was considered the finest morphology and the flaky morphology was considered the coarsest morphology. This transition in the morphology was mapped as a function of the local eutectic solidification conditions. In doing so it was found that the Si morphology would transition from a flaky → fibrous → globular + fibrous → globular structure as solidification became more rapid. The beginning of the flaky → fibrous, fibrous → globular + fibrous and the globular + fibrous → globular transitions occurred at local eutectic cooling rates of ~60 K/s, ~350 K/s, and ~1200 K/s respectively.

The results of the 3D characterization of the Si morphology identified the subtle shifts in the lamella → rod transition of the eutectic Si phase. As well, the 3D characterization found that the fineness of the Si would improve as the rate of solidification increased.

To link these changes in the microstructure to the mechanical properties the Vickers hardness of the Al-10Si alloy was measured. From a comparison between the alloy hardness and the microstructure it was found that neither the α-Al morphology, nor the length-scale refinement (of either phase) could explain the observed variations in the alloy hardness. Instead it was found that the factor affecting the alloy hardness was the Si morphology, as shifting to a globular Si improved the hardness by up to 24%. This indicated that control of the Si growth morphology was vital to maximize the mechanical properties and characteristics of hypoeutectic Al-Si alloys.

From a literature review it was found that the formation of a globular Si morphology should be possible when using other rapid solidification processes, like additive manufacturing. As such, it is recommended that these processes adjust their processing parameters to invoke a globular Si morphology when dealing with hypoeutectic Al-Si alloys.

# 6 FUTURE WORK

Based upon the results and findings of this thesis the following areas are suggested for future work:

### 1. *Influence of Impurities*

The influence of alloy impurities, on the formed microstructure, should be considered in more detail. While the Fe content was measured for the Al-10Si alloy, there was no analysis done to determine the content of other impurities. To conduct a more in-depth chemical/structural analysis it is suggested that a technique like High-Resolution Transmission Electron Microscopy (HRTEM) be used.

As well, no work was conducted on how these impurities were distributed within the alloy. It would be of interest to conduct more experiments with an IA Al-10Si alloys where the impurity content was altered (e.g. using 99.99 Al). Such testing would help quantify the influence of impurities on both the microstructure and the mechanical properties.

### 2. *Analysis of the α-Al phase via X-Ray Micro-Tomography*

A more in-depth analysis on the α-Al phase microstructure and morphology should be conducted. While, there were many morphologies of the α-Al phase that were found in this work, this quantification was limited to a 2D analysis and thus, was unable to quantify all aspects of its true 3D structure. To conduct this 3D analysis, the Al-10Si alloy would need to be analyzed via X-Ray Micro-Tomography. While difficult and expensive, this analysis would help enormously with the characterization of the α-Al phase. As it could:

1. Help characterize the presence of <100> and <110> growth, as a function of the experimental conditions.
2. Determine the number of primary nucleation sites within the alloy (as these results were found to be inconclusive).
3. Better quantify the influence of the solidification conditions on the transition in the growth direction and on the formation of the seaweed structure.

### *3. Influence of Scandium Addition*

Another aspect that should be examined further is the influence of alloy additions, specifically scandium (Sc). The interest with Sc arises from its noticeable strengthening effects in Al alloys and the open debate of how Sc refines the Si phase within the eutectic structure.

This proposed analysis could also explore how Sc addition and rapid solidification work in combination to refine the eutectic structure, as the existing research on Sc additions has only dealt with non-rapid solidification processes.

# REFERENCES

[1] Z. Li, A. Samuel, F. Samuel, C. Ravindran, S. Valtierra and H. Doty, "Parameters controlling the performance of AA319-type alloys Part 1. Tensile properties," *Materials Science and Engineering A,* vol. 367, pp. 96-110, 2004.

[2] F. Robles-Hernandez, J. Ramirez and R. Mackay, Al-Si Alloys: Automotive, Aeronautical and Aerospace Applications, Springer, 2017.

[3] T. Costa, M. Dias, L. Rocha and A. Garcia, "Effect of solution time in T6 heat treatment on microstructure and hardness of a directionally solidified Al-Si-Cu alloy," *Journal of Alloys and Compounds,* vol. 683, pp. 485-494, 2016.

[4] M. Makhlouf and G. H, "The aluminum-silicon eutectic reaction: mechanisms and crystallography," *Journal of Light Metals,* 2002.

[5] M. Warmuzek, "Introduction to Aluminum-Silicon Casting Alloys," in *Aluminum-Silicon Casting Alloys: Atlas of Microfractographs*, ASM International, 2004, p. 2.

[6] A. Hellawell, "The growth and structure of eutectics with silicon and germanium," *Progress in Materials Science,* vol. 15, pp. 1-78, 1970.

[7] M. Gupta and S. Ling, "Microstructure and mechanical properties of hypo/hyper-eutectic Al-Si alloys synthesized using near-net shape forming technique," *Journal of Alloys and Compounds,* vol. 287, pp. 284-294, 1999.

[8] S. Nikanorov, M. Volkov, V. Gurin, T. Burenkov, L. Derkachenko, B. Kardashev, L. Regel and W. Wilcox, "Structural and mechanical properties of Al-Si alloys obtained by fast cooling of a levitated melt," *Materials Science and Engineering A,* no. 390, pp. 63-69, 2005.

[9] E. Sjolaner and S. Seifeddine, *Journal of Materials Processing Technology,* vol. 210, pp. 1249-1259, 2010.

[10] M. Warmuzek, Aluminum-Silicon Casting Alloys: Atlas of Microstructures, Materials Park, Ohio: ASM International, 2016.

[11] S. Henry, T. Minghetti and M. Rappaz, "Dendrite Growth Morphologies in Aluminium Alloys," *Acta Metallurgica,* vol. 46, no. 18, pp. 6341-6443, 1998.

[12] J. Friedli, J. Fife, P. Di Napoli and M. Rappaz, "Dendritic Growth Morphologies in Al-Zn Alloys Part 1: X-ray Tomographic Microscopy," *Metallurgical and Materials Transactions A,* vol. 44A, pp. 5522-5531, 2013.

[13] M. Bedel, G. Reinhart, A. Bogno, C. Gandin, S. Jacomet, E. Boller, H. Nguyen-Thi and H. Henein, "Charaterization of dendrite morphologies in rapidly solidified Al-4.5 wt.%Cu droplets," *Acta Materialia,* vol. 89, pp. 234-246, 2015.

[14] J. Chen, U. Dahlborg, C. Bao, M. Calvo-Dahlborg and H. Henein, "Microstructure Evolution of Atomized Al-0.61 wt pct Fe and Al-1.90 wt pct Fe Alloys," *Metallurgical and Materials Transactions B,* vol. 42B, pp. 557-567, 2011.

[15] C. Wang and C. Beckermann, "Prediction of Columnar to Equiaxed Transition during Diffusion-Controlled Dendritic Alloy Solidification," *Metallurgical and Materials Transactions A,* vol. 25A, pp. 1081-1093, 1994.

[16] R. Trivedi, Y. Shen and S. Liu, "Cellular-to-Dendritic Transition during the Directional Solidifcation of Binary Alloys," *Metallurgical and Materials Transactions A,* vol. 34A, pp. 395-401, 2003.

[17] R. Spear and G. Gardner, "Dendrite Cell Size," *AFS Transactions,* vol. 71, pp. 209-215, 1963.

[18] W. Kurz and D. Fisher, Fundamentals of Solidification, Lausane: Trams. Tech. Publications, 1984.

[19] C. Caceres, C. Davidson, J. Griffiths and Q. Wang, "The Effect of Mg on the Microstructure and Mechanical Behavior of Al-Si-Mg Casting Alloys," *Met. and Mat. Transactions A,* vol. 30A, pp. 2611-2618, 1999.

[20] L. Ceschini, A. Morri, S. Toschi, S. Johansson and S. Seifeddine, "Microstructural and mechanical properties characterization of heat treated and overaged cast A354 alloy with various SDAS at room and elevated temperature," *Materials Science & Engineering A,* vol. 648, pp. 340-349, 2015.

[21] K. Nogita and A. Dahle, "Eutectic solidification in hypoeutectic Al-Si alloys: electron backscatter diffraction analysis," *Materials Chatacterization,* vol. 46, pp. 305-310, 2001.

[22] A. Dahle, K. Nogita, J. Zindel, S. McDonald and L. Hogan, "Eutectic Nucleation and Growth in Hypoeutectic Al-Si Alloys at Different Strontium Levels," *Metallurgical and Materials Transactions A,* vol. 32A, pp. 949-960, 2001.

[23] K. Nogita and A. Dahle, "Eutectic Solidification in hypoeutectic Al-Si alloys: electron backscatter diffraction analysis," *Materials Charaterization,* vol. 46, pp. 305-310, 2001.

[24] J. Campbell, "Discussion of "Effect of Strontium and Phosphorus on Eutectic Al-Si Nucleation and Formation of B-Al5FeSi in Hypoeutectic Al-Si Foundry Alloys"," *Metallurgical and Materials Transactions A,* vol. 40A, pp. 1009-1010, 2009.

[25] T. Ludwig, P. Schaffer and L. Arnberg, "Influence of Phosphorus on the Nucleation of Eutectic Silicon in Al-Si Alloys," *Metallurgical and Materials Transactions A,* vol. 44A, pp. 5796-5805, 2013.

[26] K. Nogita, A. Knuutinen, S. McDonald and A. Dahle, "Mechanisms of eutectic solidification in Al-Si alloys modifed with Ba, Ca, Y and Yb," *Journal of Light Metals,* vol. 1, pp. 219-228, 2001.

[27] Y. Cho, H.-C. Lee, K. Oh and A. Dahle, "Effect of Strontium and Phosphorus on Eutectic Al-Si Nucleation and Formation of B-Al5FeSi in Hypoeutectic Al-Si Foundry Aloys," *Metallurgical and Materials Transactions A,* vol. 39A, pp. 2435-2448, 2008.

[28] J. Dantzig and M. Rappaz, Solidification, Boca Raton: CRC Press, 2009.

[29] D. Hamilton and R. Seidensticker, *Journal of Applied Physics,* vol. 31, pp. 1165-1168, 1960.

[30] M. Shamsuzzoha and L. Hogan, *Journal of Crystal. Growth,* vol. 76, pp. 459-477, 1986.

[31] S. Lu and A. Hellawell, "The machanism of silicon modification in aluminum-silicon alloys: Impurity induced twinning," *Metallurgical Transactions A,* vol. 18, no. 10, pp. 1721-1733, 1987.

[32] D. Porter and K. Easterling, Phase Transformations in Metals and Alloys, CRC Press LLC, 1992.

[33] M. Kitamura, S. Hosoya and Sunagawa, "Re-investigation of the re-entrant corner effect in twinned crystals," *Jornal of Crystal Growth,* vol. 47, no. 1, pp. 93-99, 1979.

[34] I. Sunagawa and T. Yasuda, *Jounral of Crystal Growth,* vol. 65, p. 43, 1983.

[35] T. Hosch, L. England and R. Napolitano, "Analysis of the high growth-rate transition in Al-Si eutectic solidification," *Journal of Materials Science,* vol. 44, pp. 4892-4899, 2009.

[36] S. Hegde and K. Prabhu, "Modification of eutectic silicon in Al-Si alloys," *Journal of Materials Science,* vol. 43, pp. 3009-3027, 2008.

[37] H. Guthy, "Evolution of the Eutectic Microstructure in Chemically Modified and Unmodified Aluminum Silicon Alloys," Worcester Polytechnic Institute, 2002.

[38] S. Alkahtani, E. Elgallad, M. Tash, A. Samuel and F. Samuel, "Effect of Rare Earth Metals on the Microstructure of Al-Si based Alloys," *Materials,* vol. 45, no. 9, pp. 1-13, 2016.

[39] M. Kim, "Electron Back Scattering Diffractionf (EBSD) Analysis of Hypereutectic Al-Si Alloys Modified by Sr and Sc," *Metals and Materials International,* vol. 13, no. 2, pp. 103-107, 2007.

[40] M. Kim, Y. Hong and H. Cho, "The Effects of the Microstructure and Mechanical Properties of Hypo-Eutectic Al-Si Alloys," *Metals and Materials International,* vol. 10, no. 6, pp. 513-520, 2004.

[41] D. Herlach, P. Galenko and D. Holland-Moritz, Metastable Solids from Undercooled Melts, Germany: Elsevier, 2007.

[42] B. Thall and B. Chalmers, *Journal of the Institue of Metals,* vol. 77, p. 79, 1950.

[43] S. Flood and J. Hunt, "Modification of Al-Si eutectic alloys with Na," *Metal Science,* vol. 15, no. 7, pp. 287-294, 1981.

[44] H. V. Guthy, "Evolution of the Eutectic Microstructure in Chemically Modified and Unmodified Aluminum Silicon Alloys," Worcester Polytechnic Institute, 2002.

[45] S. Lu and A. Hellawell, *Journal of Crystal Growth,* vol. 73, p. 316, 1985.

[46] C. Levi and R. Mehrabian, "Microstructures of Rapidly Solidified Aluminum Alloy Submicron Powders," *Metallurgical Transactions A,* vol. 13A, pp. 13-23, 1982.

[47] E. Lavernia and T. Srivatsan, "The rapid solidification processing of materials: science, principles, technology, advances and applications," *Journal of Materials Science,* vol. 45, pp. 287-325, 2010.

[48] D. Herlach and D. Matson, Solidification of Containerless Undercooled Melts, Weinheim, Germany: Wiley-VCH, 2012.

[49] A. Ilbagi, H. Henein, J. Chen, D. Herlach, R. Lengsdorf, C.-A. Gandin, D. Tourret and A. Garcia-Escorial, "Containerless Solidification and Charaterization of Industrial Alloys (NEQUISOL)," *Journal of Physics: Conference Series,* vol. 327, pp. 1-19, 2011.

[50] D. Tourret, C.-A. Gandin, T. Volkmann and D. Herlach, *Acta Materialia,* vol. 59, p. 4665, 2011.

[51] H. Henein, V. Uhlenwinkel and U. Fritsching, Metal Sprays and Spray Deposition, Cham, Switzerland: Springer International Publishing, 2017.

[52] A. Freyberg, H. Henein, V. Uhlenwinkel and M. Bucholz, *Metallurgical and Materials Transactions B,* vol. 33B, pp. 243-253, 2003.

[53] H. Henein, "Single fluid atomization through the application of impulses to a melt," *Materials Science and Engineering A,* no. 326, pp. 92-100, 2002.

[54] R. V.Bargen, *Modelling & Experimental Evaluation of the Draining Behaviour of Molten Metals in the Impulse Atomization Process,* Edmonton, Alberta: University of Alberta, 2005.

[55] H. Henein, A. Ilbagi and C.-A. Gandin, "Quantitative analysis of alloy structure solidified under limited diffusion conditions," in *Solidification of Containerless Undercooled Melts*, Wiley-VCH, 2011, pp. 21-28.

[56] J. Wiskel, H. Henein and E. Maire, "Solidification of Aluminum Alloys Using Impulse Atomization: Part 1: Heat Transfer analysis of an atomized droplet," *Canadian Metallurgical Quarterly,* vol. 41, no. 1, pp. 97-110, 2002.

[57] P. Khatibi and H. Henein, "Estimation of droplet solidification temperature in rapid solidification using in-situ measurements," *Canadian Metallurgical Quarterly,* vol. 56, no. 1, pp. 76-84, 2017.

[58] M. Pierantoni, M. Gremaud, P. Magnin, D. Stoll and W. Kurz, "The Coupled Zone of Rapidly Solidified Al-Si Alloys in Laser Treatment," *Acta Metallurgica et Materialia,* vol. 40, no. 7, pp. 1637-1644, 1992.

[59] A. L. Genau, "Microstructural development in Al-Si powder during rapid solidification," Iowa State University, Ames, Iowa, 2004.

[60] R. Trivedi, F. Jin and I. Anderson, "Dynamical evolution of microstructure in finely atomized droplets of Al-Si alloys," *Acta Materialia,* vol. 51, pp. 289-300, 2003.

[61] Y. Kalay, L. Chumley, A. I and R. Napolitano, "Charaterization of Hypereutectic Al-Si Powders Solidified under Far-From Equilibrium Conditions," *Metallurgical and Materials Transactions A,* vol. 38A, pp. 1452-1457, 2007.

[62] A. Brunner, "The Effect of Hydrogen on the Rapid Solidification of Al-5wt%Si," University of Alberta, Edmonton, 2013.

[63] P. Anyalebechi, "Effects of alloying elements and solidification conditions on secondary dendrite arm spacing in aluminium alloys," *TMS,* pp. 217-233, 2004.

[64] J. Spinelli, W. Hearn, A.-A. Bogno and H. Henein, "A General Formulation of Eutectic Silicon Morphology and Processing History," *Light Metals 2018,* pp. 381-387, 2018.

[65] K. Oswalt and M. Misra, *AFS Transactions,* vol. 88, pp. 845-862, 1980.

[66] P. Anyalebechi, T. Rouns and R. Sanders, *Light Metals 1991,* no. TMS 1990, pp. 821-850, 1991.

[67] W. Prukkanon, N. Srisukhumbowornchai and C. Limmaneevichitr, "Modification of hypoeutectic Al-Si alloys with scandium," *Jornal of Alloys and Compounds,* vol. 477, pp. 454-460, 2009.

[68] H. Jones, in *Rapid Solidification of Metals and Alloys*, London, The Institution of Metallurgists, 1983, pp. 40-43.

[69] G. Armstrong and H. Jones, Solidification and Casting of Metals, London: Metals Society, 1979.

[70] A.-A. Bogno, H. Henein and M. Gallerneault, "Design and Processing Conditions of Hypoeutectic Al-Cu-Sc Alloys for Maximum Benefit of Scandium," *Light Metals 2018,* pp. 1609-1616, 2018.

[71] A. Ilbagi and H. Henein, "3D Quantitative Characterization of Rapidl Solidified Al-36 Wt Pct Ni," *Metallurgical and Materials Transactions A,* vol. 45A, pp. 2152-2160, 2014.

[72] H. Henein, V. Buchoud, R.-R. Schmidt, C. Watt, D. Malakov, C.-A. Gandin, G. Lesoult and V. Uhlenwinkel, "Droplet Solidification of Impulse Atomized Al-0.61Fe and Al-1.9Fe," *Canadian Metallurgical Quarterly,* vol. 49, no. 3, pp. 275-292, 2010.

[73] B. Cai, J. Wang, A. Kao, K. Pericleous, A. Phillion, R. Atwood and P. Lee, "4D synchrotron X-ray tomographic quantification of the transition from cellular to dendrite growth during directional solidification," *Acta Materialia,* vol. 117, pp. 160-169, 2016.

[74] H. Assadi, M. Oghabi and D. Herlach, *Acta Materialia,* vol. 57, pp. 1639-1647, 2009.

[75] A. Mullis, K. Dragnevski and R. Cochrane, "The transition from the dendrite to the seaweed growth morphology during the solidification of deeply undercooled metallic melts," *Materials Science & Engineering A,* Vols. 375-377, pp. 157-162, 2004.

[76] W. Kurz and R. Trivedi, "Eutectic Growth under Rapid Solidification Conditions," *Metallurgical Transactions A,* vol. 22A, pp. 3051-3057, 1991.

[77] K. Jackson and J. Hunt, *Trans. Am. Inst. Min. Engineers,* vol. 236, p. 1129, 1966.

[78] R. Trivedi, P. Magnin and W. Kurz, "Theory of Eutectic Growth Under Rapid Solidification Conditions," *Acta Materialia,* vol. 35, pp. 971-980, 1987.

[79] M. Gunduz, H. Kaya, E. Cadirli and A. Ozmen, "Interflake spacings and undercoolings in Al-Si irregular eutectic alloy," *Materials Science and Engineering ,* vol. 369, pp. 215-229, 2004.

[80] P. Magnin, J. Mason and R. Trivedi, "Growth of Irregular Eutectics and the Al-Si System," *Acta Metallurgica et Materialia,* vol. 39, no. 4, pp. 469-480, 1991.

[81] A. Garcia, T. Clyne and M. Prates, "Mathematical Model for the Unidirectional Solidification of Metals: II. Massive Molds," *Metallurgical Transactions B,* vol. 10B, pp. 85-92, 1979.

[82] J. Spinelli, A. Bogno and H. Henein, "Two-Zone Microstructures in Al-18Si Alloy Powders," *Metallurgical and Materials Transactions A,* vol. 49, no. 2, pp. 550-562, 2018.

[83] Z. Zhang, X. Bian, Y. Wang and X. Liu, "Refinement and thermal analysis of hypereutectic Al-25%Si alloy," *Transactions o Nonferrous Metals Society of China,* vol. 11, no. 3, pp. 374-377, 2001.

[84] R. Retes, T. Bello, R. Kakitani, T. Costa, A. Garcia, N. Cheung and J. Spinelli, "Tensilt properties and related microstructures aspects of hypereutectic Al-Si alloys directionally solidified under different melt superheats and transient heat flow conditions," *Materials Science and Engineering A,* vol. 685, pp. 235-243, 2017.

[85] W. D. Callister Jr. and D. G. Rethwisch, Fundamentals of Materials Science and Engineering: An Integrated Approach, Hoboken: John Wiley & Sons, 2008.

[86] W. Zheng, Y. Liu, J. Yang, J. Dang, X. Hong and Z. Du, "Effect o Sc content on the microstructure of As-Cast Al-7wt%Si alloys," *Materials Charaterization,* vol. 66, pp. 104-110, 2012.

[87] S. Ji, H. Yang, X. Cui and Z. Fan, "Macro-heterogeneities in microstructures, concentrations, defects and tensile propertie of die cast Al-Mg-Si alloys," *Materials Science and Technology,* vol. 33, no. 18, pp. 2223-2233, 2017.

[88] G. Kumar, S. Hedge and K. Prabhu, "Heat transfer and solidification behaviour of modified A357 alloy," *Journal of Materials Processing Technology,* vol. 183, pp. 152-156, 2007.

[89] M. Paliwal and I.-H. Jung, "The evolution of growth morphology in Mg-Al alloys depending on the cooling rate during solidification," *Acta Materialia,* vol. 61, pp. 4848-4860, 2013.

[90] R. Dehoff, M. M. Kirka, W. J. Sames, H. Bilheux, A. Tremsin, L. Love and S. Babu, "Site specific control of crystallographic grain orientation through electron beam additive manufacturing," *Materials Science and Technology,* vol. 31, no. 8, pp. 931-938, 2015.

[91] H. Wei, T. Mukherjee and T. DebRoy, "Grain Growth Modeling for Additive Manufacturing of Nickel Based Superalloys," *Proceedings of the 6th International Conference on Recrystallization and Grain Growth,* pp. 265-269, 2016.

[92] A. Prasad and H. Henein, "Droplet cooling in atomization sprays," *Jornal of Materials Sciences,* no. 43, pp. 5930-5941, 2008.

# APPENDICES

## APPENDIX A: FE CONTENT ANALYSIS RESULTS

This appendix outlines the Fe content analysis that was conducted on the IA Al-10Si alloy by Cambridge Materials Testing Ltd.

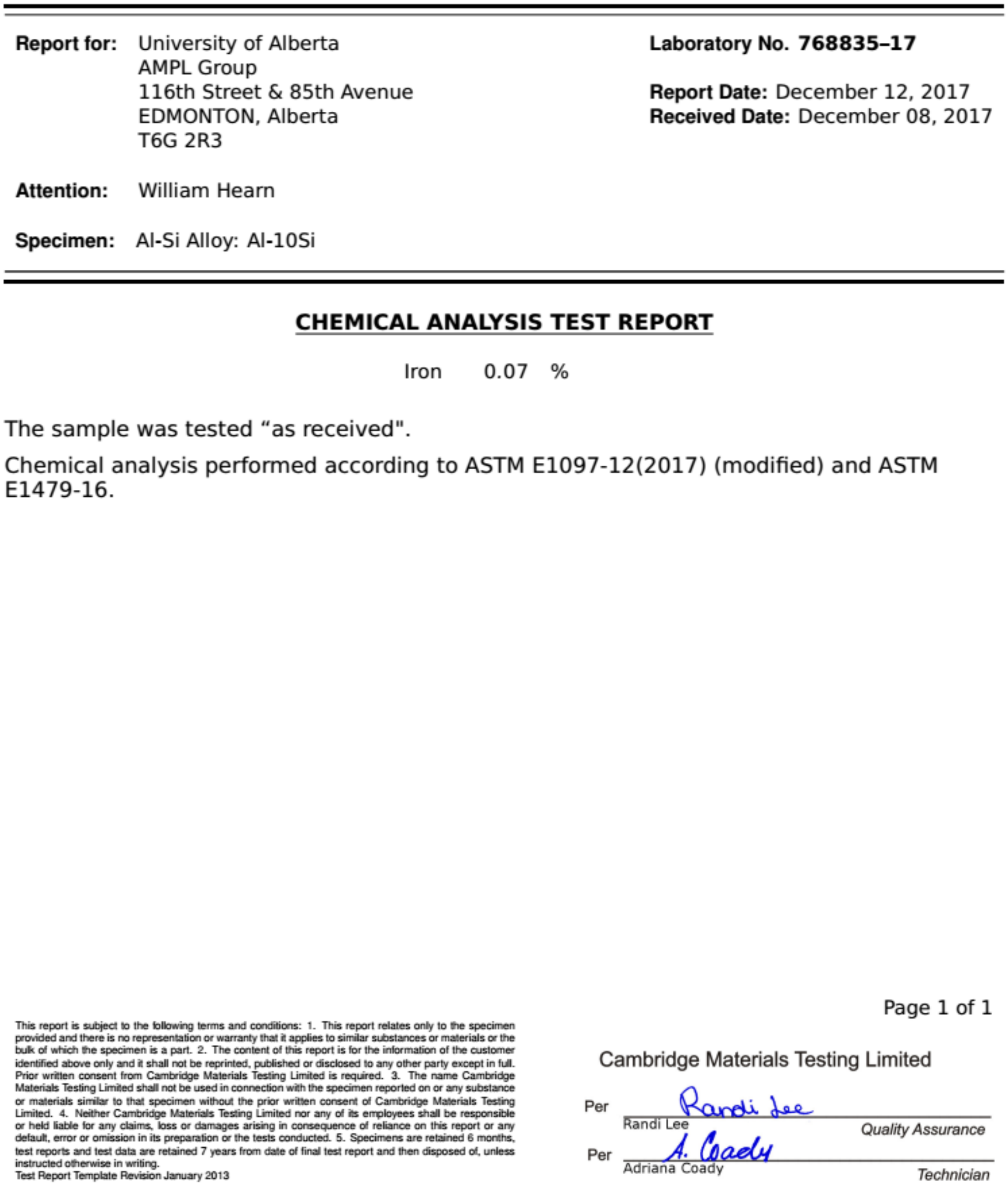

**Report for:** University of Alberta
AMPL Group
116th Street & 85th Avenue
EDMONTON, Alberta
T6G 2R3

**Laboratory No. 768835–17**

**Report Date:** December 12, 2017
**Received Date:** December 08, 2017

**Attention:** William Hearn

**Specimen:** Al-Si Alloy: Al-10Si

**CHEMICAL ANALYSIS TEST REPORT**

Iron 0.07 %

The sample was tested “as received".

Chemical analysis performed according to ASTM E1097-12(2017) (modified) and ASTM E1479-16.

Page 1 of 1

This report is subject to the following terms and conditions: 1. This report relates only to the specimen provided and there is no representation or warranty that it applies to similar substances or materials or the bulk of which the specimen is a part. 2. The content of this report is for the information of the customer identified above only and it shall not be reprinted, published or disclosed to any other party except in full. Prior written consent from Cambridge Materials Testing Limited is required. 3. The name Cambridge Materials Testing Limited shall not be used in connection with the specimen reported on or any substance or materials similar to that specimen without the prior written consent of Cambridge Materials Testing Limited. 4. Neither Cambridge Materials Testing Limited nor any of its employees shall be responsible or held liable for any claims, loss or damages arising in consequence of reliance on this report or any default, error or omission in its preparation or the tests conducted. 5. Specimens are retained 6 months, test reports and test data are retained 7 years from date of final test report and then disposed of, unless instructed otherwise in writing.
Test Report Template Revision January 2013

Cambridge Materials Testing Limited

Per Randi Lee
Randi Lee *Quality Assurance*

Per A. Coady
Adriana Coady *Technician*

# APPENDIX B: AREA FRACTION TO EUTECTIC FRACTION CONVERSION

This appendix presents the procedure that was used to convert the area fraction into the weight fraction.

Before conducting the conversion, the amount of Al and Si present within the eutectic structure must be found. To determine this a tie-line calculation was conducted at the eutectic point:

$$f_{\alpha_{Eut}} = \frac{C_{Eut} - C_l}{C_s - C_l} \qquad (0\text{-}1)$$

Where $f_{\alpha_{Eut}}$ is the fraction of Al within the eutectic, $C_{Eut}$ is the eutectic composition, $C_l$ is the composition of the liquid and $C_s$ is the composition of the solid. This determination assumed that no undercooling took place during solidification.

The $C_s$, $C_{Eut}$ and $C_l$ values at the eutectic temperature, for the Al-10Si alloy, were 1.65%, 12.6% and 100% respectively [92] and are shown schematically in Figure 0-1. Using these values, the fraction of Al and Si in the eutectic was found to be 88.9% and 11.1% respectively.

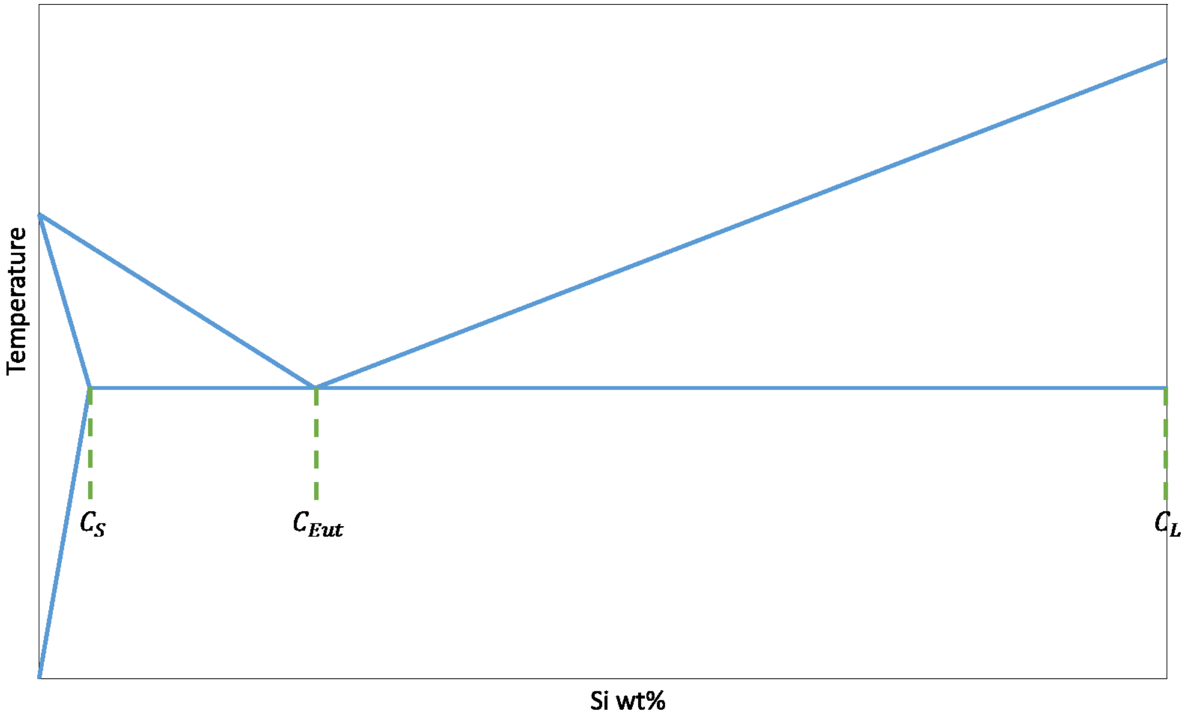

Figure 0-1: Schematic of the Al-Si phase diagram that outlines the compositions used to determine the amount of Al and Si that is present within the eutectic structure.

With these values, along with the densities and measured area fraction, the weight fraction could be calculated using the relationship below:

$$f_E = \frac{A_{Eut}(\rho_{Al} f_{\alpha_{Eut}} + \rho_{Si} f_{Si_{Eut}})}{\left(A_{Eut}(\rho_{Al} f_{\alpha_{Eut}} + \rho_{Si} f_{Si_{Eut}})\right) + (100 - A_{Eut})\rho_{Al}} \qquad (\ 0\text{-}2\ )$$

Where $f_E$ is the eutectic weight fraction, $A_{Eut}$ is the eutectic area fraction, $\rho_{Al}$ is the density of Al, $\rho_{Si}$ is the density of Si and $f_{Si_{Eut}}$ is fraction of Si within the eutectic. This determination assumed that there was no super saturation of Si in Al above the maximum solid solubility at equilibrium (1.65wt%).

The values for the Al & Si densities were 2710 $kgm^{-3}$ and 2330 $kgm^{-3}$ respectively [85].

# APPENDIX C: EQUILIBRIUM AND GUILLIVER-SCHEIL EUTECTIC FRACTION ESTIMATIONS

This appendix outlines the calculations used for the equilibrium and the Guilliver-Scheil estimations of the eutectic fraction.

To conduct the equilibrium estimation a tie-line calculation is done at the eutectic temperature:

$$f_E = 1 - \left(\frac{C_o - C_l}{C_s - C_l}\right) \qquad (\,0\text{-}3\,)$$

Where $f_{eut}$ is the eutectic fraction, $C_o$ is the nominal composition of the alloy (10wt% Si), $C_s$ is the composition of the solid (1.65wt%) and $C_l$ is the composition of the liquid (12.6wt%). The location of these composition on the Al-Si phase diagram can be seen schematically in Figure 0-2.

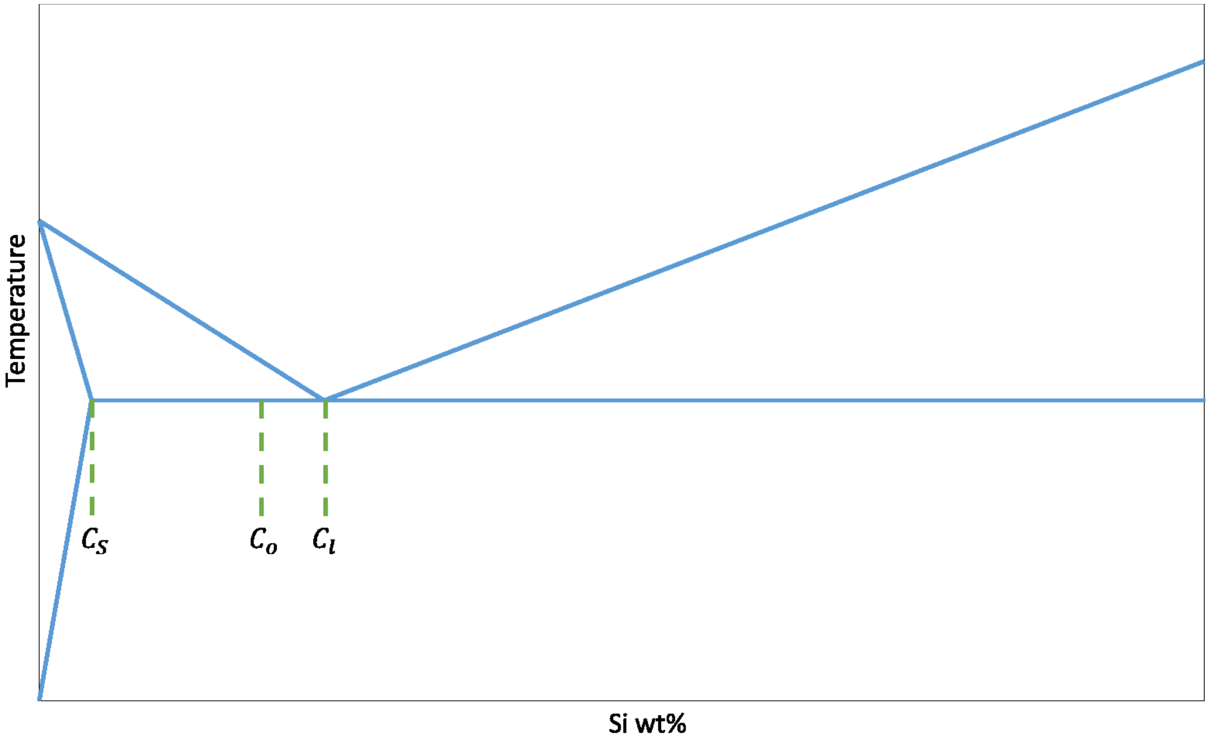

Figure 0-2: Schematic of the Al-Si phase diagram outlining the compositions used for the tie-line and Guilliver-Scheil estimations of the eutectic fraction.

Using these values, the equilibrium eutectic fraction was calculated:

$$f_E = 1 - \left(\frac{10 - 12.6}{1.65 - 12.6}\right) = \mathbf{76.3\%}$$

To conduct the Guilliver-Scheil estimation the Guilliver-Scheil model, representing the liquid fraction at the eutectic temperature, was used:

$$F_E = \left(\frac{C_l}{C_o}\right)^{\frac{1}{k-1}} \tag{0-4}$$

$$k = \frac{C_s}{C_l} \tag{0-5}$$

Where $F_E$ is the eutectic weight fraction, $C_o$ is the initial alloy composition (10 wt.%), $C_l$ is the amount of liquid present, $C_s$ is the amount of solid present and k is the partition coefficient.

Using these values, the Guilliver-Scheil eutectic fraction was calculated:

$$k = \frac{C_s}{C_l} = \frac{1.65}{12.6} = 0.131$$

$$F_E = \left(\frac{12.6}{10}\right)^{\frac{1}{0.13-1}} = \mathbf{76.6}\%$$

## APPENDIX D: EUTECTIC NUCLEATION UNDERCOOLING ESTIMATION

The developed method to estimate the eutectic nucleation undercooling was a trial and error approach that used a measured eutectic fraction, the Guilliver-Scheil micro segregation model and the extensions of the solidus and liquidus lines.

Typically, Guilliver-Scheil is used to determine the solid fraction, however in the context of this method it was used in a slightly different manner.

Since this method considered the growth of the primary α-Al phase to stop immediately after the eutectic structure nucleates, all remaining liquid in the melt should turn into eutectic. Meaning that the liquid fraction and the eutectic fraction are one in the same.

As such the Guilliver-Scheil equation was modified to calculate the liquid fraction, and in turn the eutectic fraction:

$$F_E = \left(\frac{C_l}{C_o}\right)^{\frac{1}{k-1}} \qquad (\text{0-6})$$

$$k = \frac{C_s}{C_l} \qquad (\text{0-7})$$

Where $F_E$ is the eutectic weight fraction, $C_o$ is the initial alloy composition (in terms of wt% Si), $C_l$ is the amount of liquid present, $C_s$ is the amount of solid present and k is the partition coefficient.

Starting with a guess of the eutectic nucleation temperature ($T_E'$), at the eutectic temperature, the theoretically expected eutectic fraction, at this $T_E'$, was calculated using the modified Guilliver-Scheil expression in equation 7-6.

This theoretically expected eutectic fraction, at the guessed $T_E'$, was then compared to the experimentally measured eutectic fraction using the criterion below:

$$\Delta T_E \; Criterion = \left(\frac{abs\left(F_{E,Calc} - F_{E,Exp}\right)}{F_{E,Exp}}\right) < \; 0.002 \qquad (\text{0-8})$$

Where $F_{E,Calc}$ is the Guilliver-Scheil calculated eutectic fraction and $F_{E,Exp}$ is the experimentally measured eutectic fraction.

If this criterion was not met, then the guessed $T_E'$ was incorrect. If so the method would be repeated at a new $T_E'$ that was 0.05°C less than the previous $T_E'$. This trial and error approach would continue until the expected eutectic fraction and the experimentally measured eutectic fraction matched one another. A schematic of this method can be seen in Figure 0-3.

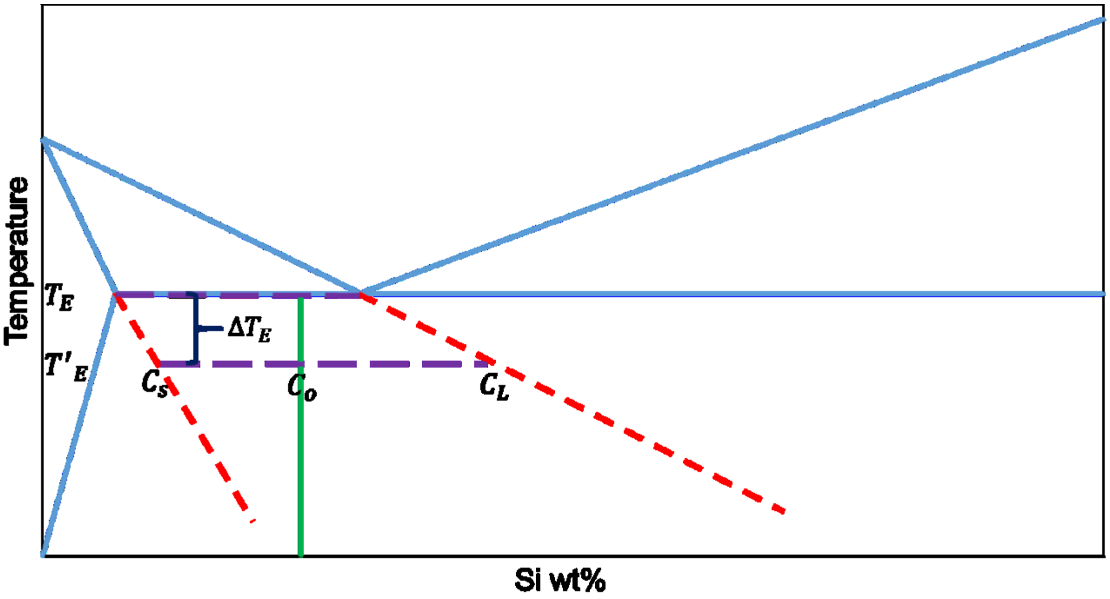

Figure 0-3: Schematic of the eutectic nucleation undercooling estimation method. The red dotted lines represent the meta-stable extensions of the solidus and liquidus. The solid green line represents the Co of the examined alloy (10wt% Si). $T_E'$ is the eutectic nucleation temperature.

Once the experimental and the measured eutectic fractions matched it meant that the guessed $T_E'$ was correct. As such this $T_E'$ could be considered the temperature where eutectic nucleation occurred and could be used to determine the eutectic nucleation undercooling:

$$\Delta T_E = T_E - T_E' \tag{0-9}$$

Where $\Delta T_E$ is the eutectic nucleation undercooling, $T_E'$ is the temperature where eutectic nucleation occurred and $T_E$ is the eutectic temperature.

# APPENDIX E: EUTECTIC NUCLEATION UNDERCOOLING ESTIMATION MATLAB CODE

This appendix displays the developed MATLAB code that was used to estimate the eutectic nucleation undercooling.

```
%% Estimation of Eutectic Nucleation Undercooling
clear; clc;

%% Counters
counter = 0;

%% User Input
Co = 10; %intial composition of hypoeutectic alloy [wt%]
liquidus_temperature = 868; %value of liquidus line at chosen composition [K]

eutectic_fraction_measured = 38.43426921; %eutectic fraction in terms of
percentage

%% Values for Eutectic Undercooling Calculation
temperature_eutectic = 850.8; %eutectic temperature [K]

%% Caculate Theoretical Eutectic Fraction & Estimate Eutectic Undercooling

temperature_eutectic_nucleation = 850.8; %intial guess of eutectic
temperature in Kelvin
Cl_intial = 12.6;
Cs_intial = 1.55;
eutectic_fraction_calculated = ((Cl_intial/Co)^(1/((Cs_intial/Cl_intial)-
1)))*100;

eutectic_fraction_comparison = abs(eutectic_fraction_calculated-
eutectic_fraction_measured)/eutectic_fraction_measured;

while eutectic_fraction_comparison > 0.0002
    temperature_eutectic_nucleation = temperature_eutectic_nucleation - 0.05;

    Cl_eutectic = (-0.0973)*temperature_eutectic_nucleation + 96.473;
    Cs_eutectic = (-0.0342)*temperature_eutectic_nucleation + 29.848;

    eutectic_fraction_calculated =
((Cl_eutectic/Co)^(1/((Cs_eutectic/Cl_eutectic)-1)))*100;
    eutectic_fraction_comparison = abs(eutectic_fraction_calculated-
eutectic_fraction_measured)/eutectic_fraction_measured;
end

eutectic_undercooling =  temperature_eutectic -
temperature_eutectic_nucleation;
```

## APPENDIX F: AL-10SI MATERIAL DATA SHEET FOR THERMAL MODEL

This appendix lists the Al-10Si materials data used for the thermal model input .txt file.

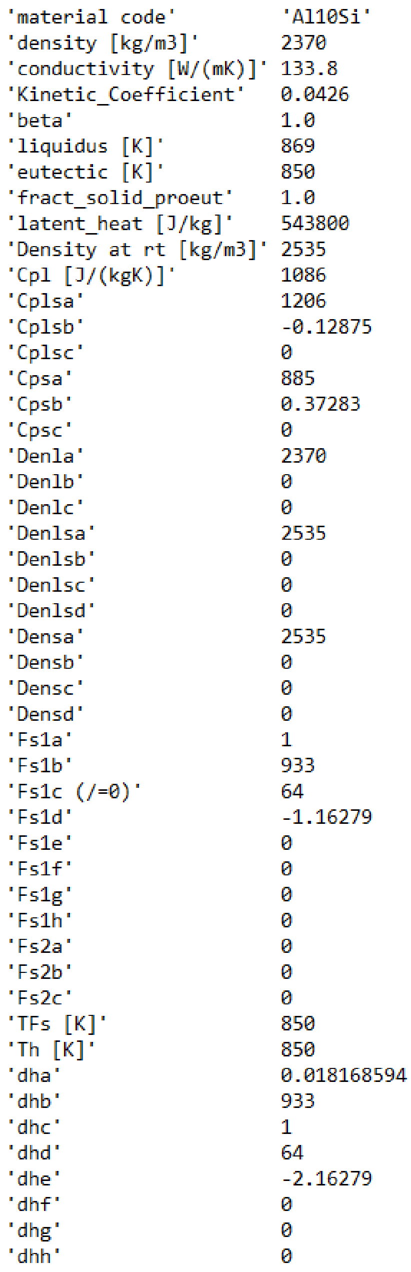

```
'material code'         'Al10Si'
'density [kg/m3]'       2370
'conductivity [W/(mK)]' 133.8
'Kinetic_Coefficient'   0.0426
'beta'                  1.0
'liquidus [K]'          869
'eutectic [K]'          850
'fract_solid_proeut'    1.0
'latent_heat [J/kg]'    543800
'Density at rt [kg/m3]' 2535
'Cpl [J/(kgK)]'         1086
'Cplsa'                 1206
'Cplsb'                 -0.12875
'Cplsc'                 0
'Cpsa'                  885
'Cpsb'                  0.37283
'Cpsc'                  0
'Denla'                 2370
'Denlb'                 0
'Denlc'                 0
'Denlsa'                2535
'Denlsb'                0
'Denlsc'                0
'Denlsd'                0
'Densa'                 2535
'Densb'                 0
'Densc'                 0
'Densd'                 0
'Fs1a'                  1
'Fs1b'                  933
'Fs1c (/=0)'            64
'Fs1d'                  -1.16279
'Fs1e'                  0
'Fs1f'                  0
'Fs1g'                  0
'Fs1h'                  0
'Fs2a'                  0
'Fs2b'                  0
'Fs2c'                  0
'TFs [K]'               850
'Th [K]'                850
'dha'                   0.018168594
'dhb'                   933
'dhc'                   1
'dhd'                   64
'dhe'                   -2.16279
'dhf'                   0
'dhg'                   0
'dhh'                   0
```

# APPENDIX G: LIMITED VARIABILITY OF THE AVERAGE SOLIDIFICATION COOLING RATE WITH THE INPUTTED $\Delta T_P$

In this appendix the limited variability of the average solidification cooling rate, with the inputted $\Delta T_p$, is shown.

For each examined particle size range the average solidification cooling rate was found, using the thermal model, at various $\Delta T_p$ inputs, ranging between 0K to 30K. These results were plotted in Figure 0-4.

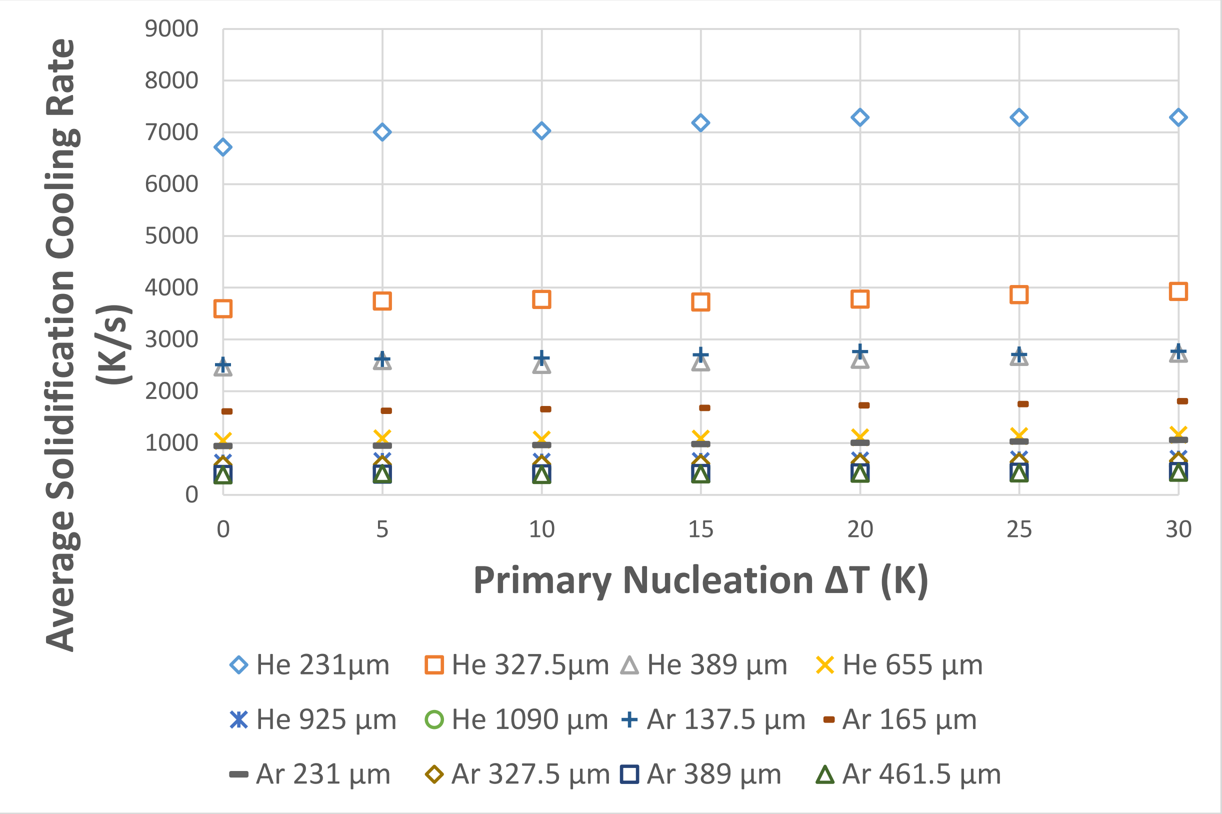

Figure 0-4: Influence of the $\Delta T_p$ on the calculated average coarsening cooling rate.

Examining Figure 0-4 there was only an 8 to 13% variation in the average solidification cooling rate as the $\Delta T_p$ changes. This result shows the limited variability of the average solidification cooling rate with the $\Delta T_p$. As such any estimations of the solidification cooling rate were carried out using a $\Delta T_p = 0$. This limited variability of the cooling rate, with respect to the inputted $\Delta T_p$, was also found by Prasad et al. [92] when using the thermal model to estimate the cooling rate for an AA6061 alloy.

## APPENDIX H: AVERAGE SOLIDIFICATION COOLING RATE ESTIMATION MATLAB CODE

This appendix displays the developed MATLAB code that was used to estimate the average solidification cooling rate.

```
%% Estimation of Average Solidification Cooling Rate
clear; clc;

%% Counters
counter = 0;
%SDAS_vector = zeros(458);
%counter_vector = zeros(458);
%count_above_eutectic = 0;
%% User Input

Co = 10; %intial composition of hypoeutectic alloy [wt%]
liquidus_temperature = 868; %value of liquidus line at chosen composition [K]

eutectic_fraction_measured = 44.60680634; %eutectic fraction in terms of
percentage
SDAS_measured = 0.000005106159817; %secondary dendrite arm spacing [m]
droplet_diameter = 1090; %mean droplet diameter [microns]

atomization_gas = 'h'; %used atomization gas
intial_gas_temperature = 295; %intial temperature of the gas during
atomization
intial_melt_temperature = 1023; %intial temperature of the melt [K]
stop_temperature = 500; %fixed

%% .txt file Inputs

time_step = 0.00001; %fixed value
intial_velocity = 0.5; %fixed
quit_function = 'q'; %fixed

%% Values for Eutectic Undercooling Calculation

temperature_eutectic = 850.8; %eutectic temperature [K]

%% Values for Primary Undercooling Calculation

k = 0.13; %partition coefficient Al-10Si
gibbs_thompson_coefficient_Al = 0.000000196; % [Km]
gibbs_thompson_coefficient_Si = 0.00000017; % [Km]
surface_energy = (Co*gibbs_thompson_coefficient_Si + (100-
10)*gibbs_thompson_coefficient_Al)/100;
m = 5.25; %liquidus slope [K/wt%]
latent_heat = 397000; % latent heat of solidification J/kg
lnDo = -15.494-0.39095*Co+0.027572*(Co^2);
QR = 3328-335.8*Co+19.34*(Co^2);
```

```
%% Caculate Theoretical Eutectic Fraction & Estimate Eutectic Undercooling

temperature_eutectic_nucleation = 850.8; %intial guess of eutectic
temperature in Kelvin
Cl_intial = 12.6;
Cs_intial = 1.55;
eutectic_fraction_calculated = ((Cl_intial/Co)^(1/((Cs_intial/Cl_intial)-
1)))*100;

eutectic_fraction_comparison = abs(eutectic_fraction_calculated-
eutectic_fraction_measured)/eutectic_fraction_measured;

while eutectic_fraction_comparison > 0.0002
    temperature_eutectic_nucleation = temperature_eutectic_nucleation - 0.05;

    Cl_eutectic = (-0.0973)*temperature_eutectic_nucleation + 96.473;
    Cs_eutectic = (-0.0342)*temperature_eutectic_nucleation + 29.848;

    eutectic_fraction_calculated =
((Cl_eutectic/Co)^(1/((Cs_eutectic/Cl_eutectic)-1)))*100;
    eutectic_fraction_comparison = abs(eutectic_fraction_calculated-
eutectic_fraction_measured)/eutectic_fraction_measured;
end

eutectic_undercooling =  temperature_eutectic -
temperature_eutectic_nucleation;

%% Non-Iteration Thermal Model for Cooling Rate and Recalescence Temperature

% Intial Guess of Primary Nucleation Temperature
primary_nucleation_temperature = liquidus_temperature; %intial guess of
temperature where intial phase nucleates
primary_undercooling = liquidus_temperature - primary_nucleation_temperature;
%intial guess of undercooling temperature

% Writing variables for Input File
fid = fopen('input.txt','wt');

fprintf(fid, '%d\n', primary_undercooling);
fprintf(fid, '%s\n', atomization_gas);
fprintf(fid, '%d\n', intial_gas_temperature);
fprintf(fid, '%d\n', droplet_diameter);
fprintf(fid, '%d\n', time_step);
fprintf(fid, '%d\n', intial_melt_temperature);
fprintf(fid, '%d\n', stop_temperature);
fprintf(fid, '%d\n', intial_velocity);
fprintf(fid, '%s\n', quit_function);

fclose(fid);

% Saving Thermal.exe file
[status, result] = system(['Thermal.exe<', 'input.txt']);

fid = fopen('logout.txt','wt');
```

```
fprintf(fid, '%s', result);
fclose(fid);

% Recalescence Temperature
recalescence_temperature = liquidus_temperature;

%Determine Cooling Rate using time.txt file
timetxt = readtable('time.txt');
[mm,nn] = size(timetxt); %determine number of columns
mm = mm/2;

timetxt_counter = 1;

%Read time.txt file
while timetxt_counter < mm
    tttt = timetxt(timetxt_counter,1); %read specific line from table where
cooling rate is
    ttt = table2array(tttt); %convert table values into an array
    tx = cell2mat(ttt); % convert to char array
    T_temp = str2num(tx(15:23));
    T_temp = T_temp + 273;
    t_temp = str2num(tx(2:7));
    T_comparison = abs(T_temp-
recalescence_temperature)/recalescence_temperature;
    T_eutectic_comparison = abs(T_temp-
temperature_eutectic_nucleation)/temperature_eutectic_nucleation;

    if T_comparison < 0.001
        t_recalescence = t_temp;
        Temperature_rec = T_temp;
    end

    if T_eutectic_comparison < 0.001
        t_eutectic = t_temp;
        Temperature_eut = T_temp;
    end

    timetxt_counter = timetxt_counter +1;
end

cooling_rate = (-1)*(Temperature_rec-Temperature_eut)/(t_recalescence-
t_eutectic);
```

# APPENDIX I: QUANTITATIVE SI MORPHOLOGY CHARACTERIZATION

This appendix will outline the developed quantitative technique that was used to characterize the Si growth morphology.

### Methodology

Previous work by Hosch [35] and Costa [3] found that shape descriptors were an effective way to quantitatively analyze a microstructure. As they could provide a numerical value to describe a specific shape. So, it was thought that the use of these shape descriptors could help characterize the eutectic Si morphology of the impulse atomized Al-10Si alloy. For this analysis the specific shape descriptors that were used were the aspect ratio and the circularity.

The circularity is a dimensionless shape factor that relates a particle's surface area (S) to its perimeter (P):

$$Circularity = \frac{4\pi S}{P^2} \qquad (0\text{-}10)$$

Essentially the circularity helps determine the "roundness" of a particle on a scale of 0 to 1, with 1 being perfectly round and 0 being not round at all.

The aspect ratio is also a dimensionless shape factor, but it represents the ratio between the largest dimension of a particle and the smallest dimension (that is perpendicular to its maximum). This shape descriptor also helps determine the "roundness", where the closer the aspect ratio is to 1 the more circular it is. A representation of the aspect ratio can be seen in Figure 0-5.

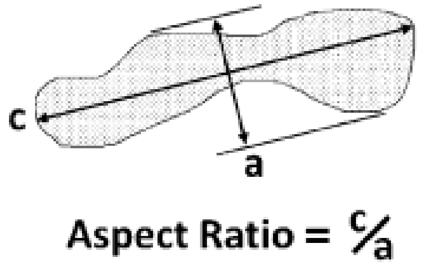

Figure 0-5: Schematic of the Aspect Ratio *[35]*.

To conduct this shape descriptor analysis a combination of SEM images, ImageJ software and MATLAB software was used. Initially a SEM image of the eutectic structure would be opened with the ImageJ program. Using ImageJ, the Si phase, in the image, would become isolated from the surrounding Al matrix using binary image contrast. This isolated Si phase would have its circularity and aspect ratio measured by the ImageJ program, with these results being outputted as an excel file. This outputted file would then be organized and refined using a MATLAB script to conduct the quantitative analysis. The MATLAB script used in this analysis can be found in Appendix J.

**Results**

The average aspect ratio and average circularity (per particle) were both plotted as a function of the particle size in Figure 0-6 and Figure 0-7, respectively. Examining these figures, both shape descriptors show no noticeable trend to either experimental condition. Also, the standard deviations of these shape descriptors were so large that no meaningful comparisons could be made anyways. Showing that this type of quantitative analysis, using an average shape descriptor value, was inadequate to understand the Si morphology.

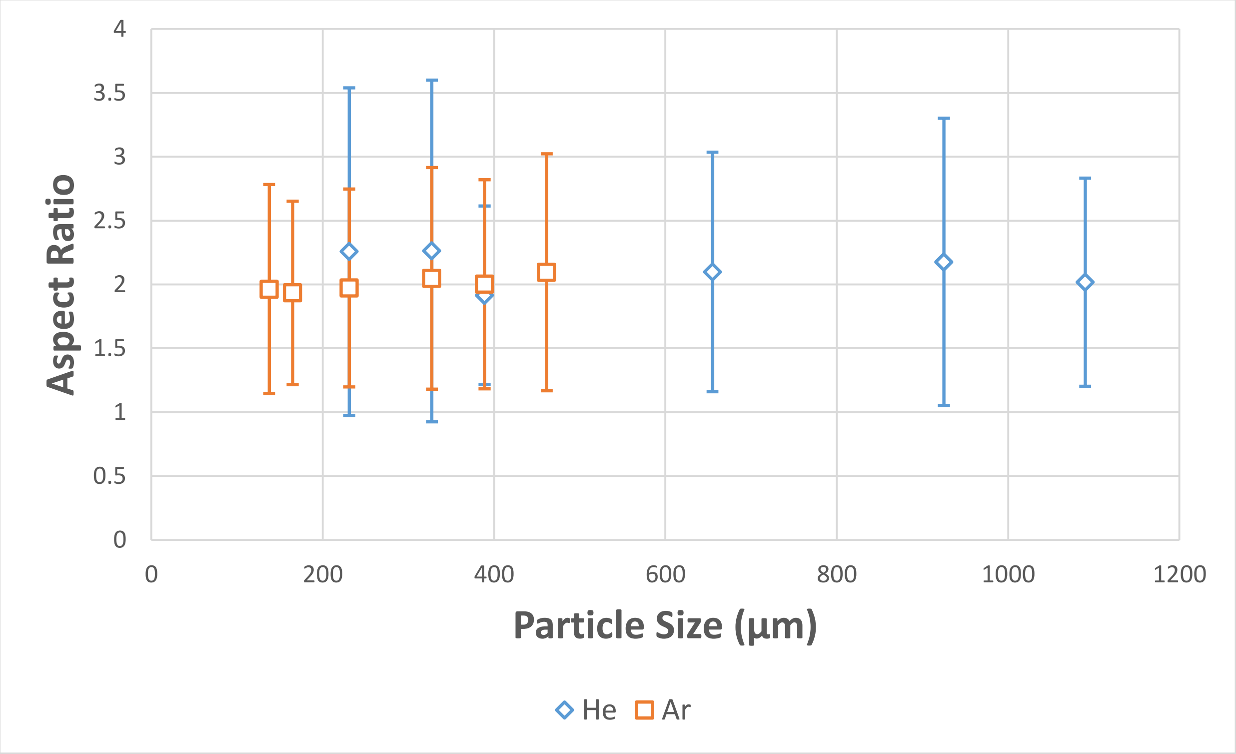

Figure 0-6: Aspect ratio as a function of the particle size.

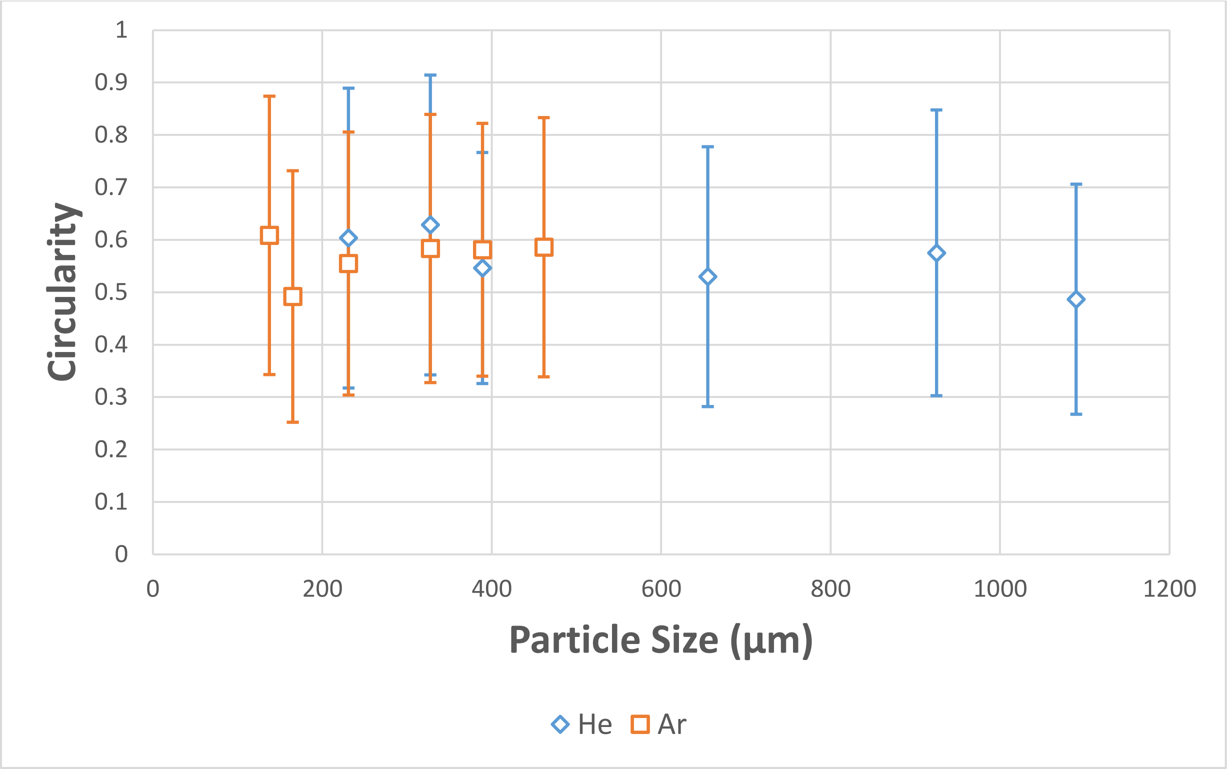

Figure 0-7: Circularity as a function of the particle size.

With the shape descriptors proving to be inadequate on their own, a new approach was attempted where the shape descriptor results were combined with the qualitative 2D analysis. To combine these results the average aspect ratio and the average circularity were calculated as a function of the 2D Si morphology. These results can be seen in Figure 0-8 and Figure 0-9 for the aspect ratio and the circularity respectively.

When examining the aspect ratio results in Figure 0-8 no clear relationship can be seen. As the average aspect ratio was very similar for each Si morphology and within the range of the standard deviation. However, the results of the average circularity in Figure 0-9 did show a relationship. Where an increase in the circularity occurred as the Si morphology became more “refined”. As the Globular morphology was considered, from qualitative analysis, to be more rounded in shape than the other morphologies (Fibrous and Flaky).

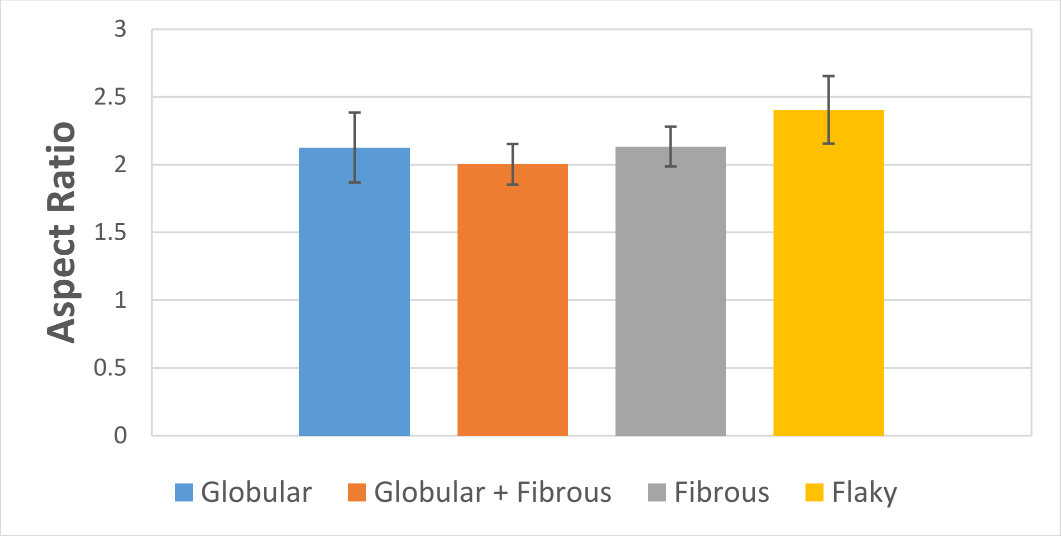

Figure 0-8: Aspect ratio as a function of the qualitative 2D Si morphology.

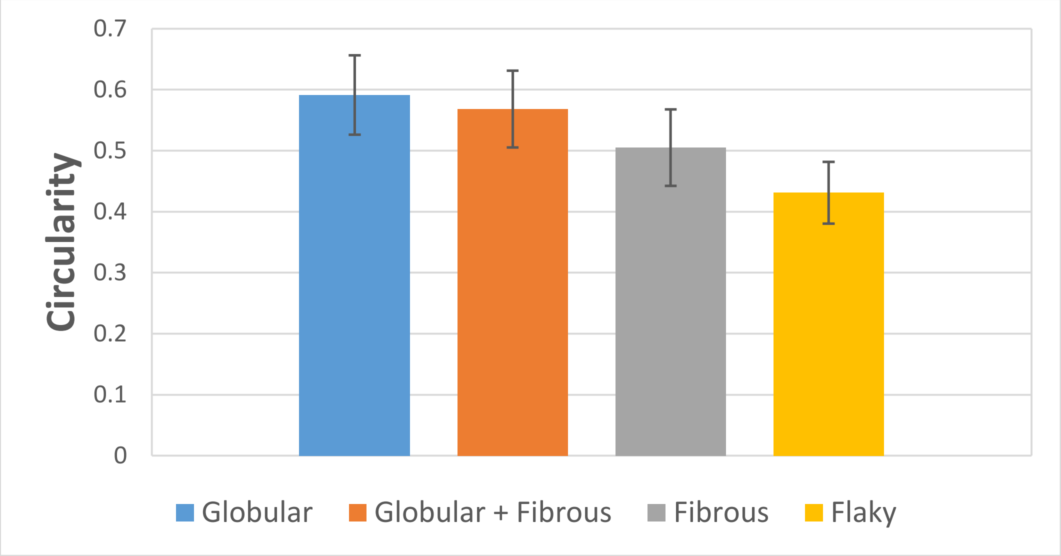

Figure 0-9: Circularity as a function of the qualitative 2D Si morphology.

In closing this analysis found that the aspect ratio is not a useful tool to describe the refinement of the eutectic Si morphology. However, it seems that the circularity might be able to quantitatively characterize the Si morphology. As this circularity seems to relate to variations in the Si morphology. While more development of this technique is required it has the capability to be a useful tool to help characterize refinement of the eutectic structure in Al-Si alloys.

# Appendix J: Quantitative Si Morphology Analysis MATLAB Code

This appendix displays the developed MATLAB code that was used to refine the excel file shape descriptor results outputted by ImageJ.

```
%% Quantiative Si Morphology Analysis

clear; clc;

%% User Input
filename = 'Results.csv';

min_cutoff = 0.079;                    %Pixel Area cutoff
max_cutoff = 1000000;

%% Extracting & Sorting Data from csv file

A = importdata(filename);
data = A.data;
x = length(data);
i = 1;

while i <= x
    if data(i,2) < min_cutoff
        data(i,:) = [];
        x = length(data);
        i = i;
    elseif data(i,2) > max_cutoff
        data(i,:) = [];
        x = length(data);
        i = i;
    else
    x = length(data);
    i = i+1;
    end
end

Area = data(:,2);
StDev = data(:,3);
XM = data(:,4);
YM = data(:,5);
Circ = data(:,6);
PercentArea = data(:,7);
AR = data(:,8);
Round = data(:,9);
Solidity = data(:,10);

%% Calculate Average & STDEV of Each Variable

Circ_Average = mean(Circ);
Circ_STDEV = std(Circ);
AR_Average = mean(AR);
AR_STDEV = std(AR);
```

```
%% Sorting Results by Circularity

m = 1;
fibrous = 0;
transition = 0;
rounded = 0;

while m <= x
    if Circ(m,1) < 0.5
        fibrous = fibrous+1;
    elseif Circ(m,1) >= 0.5 && Circ(m,1) < 0.7
        transition = transition+1;
    elseif Circ(m,1) >= 0.7 && Circ(m,1) <= 1
        rounded = rounded+1;
    end
    m = m+1;
end

%% Intializing matrix to store each type of Variable Sorted by circularity

fibrous_holder_matrix = zeros(fibrous,10);                 %10 chosen by the
number of categories in teh csv file
transition_holder_matrix = zeros(transition,10);
rounded_holder_matrix = zeros(rounded,10);

%% Create Vectors to Store Circularity Sorted Values

circ_loop_counter = 1;
fibrous_counter = 1;
transition_counter = 1;
rounded_counter = 1;

while circ_loop_counter <= x
    if data(circ_loop_counter,6) < 0.5
        fibrous_holder_matrix(fibrous_counter,2) = Area(circ_loop_counter,1);
        fibrous_holder_matrix(fibrous_counter,3) =
StDev(circ_loop_counter,1);
        fibrous_holder_matrix(fibrous_counter,4) = XM(circ_loop_counter,1);
        fibrous_holder_matrix(fibrous_counter,5) = YM(circ_loop_counter,1);
        fibrous_holder_matrix(fibrous_counter,6) = Circ(circ_loop_counter,1);
        fibrous_holder_matrix(fibrous_counter,7) =
PercentArea(circ_loop_counter,1);
        fibrous_holder_matrix(fibrous_counter,8) = AR(circ_loop_counter,1);
        fibrous_holder_matrix(fibrous_counter,9) =
Round(circ_loop_counter,1);
        fibrous_holder_matrix(fibrous_counter,10) =
Solidity(circ_loop_counter,1);
        fibrous_counter = fibrous_counter+1;
        circ_loop_counter = circ_loop_counter + 1;

    elseif data(circ_loop_counter,6) >= 0.5 && data(circ_loop_counter,6) <
0.7
        transition_holder_matrix(transition_counter,2) =
Area(circ_loop_counter,1);
```

```
        transition_holder_matrix(transition_counter,3) =
StDev(circ_loop_counter,1);
        transition_holder_matrix(transition_counter,4) =
XM(circ_loop_counter,1);
        transition_holder_matrix(transition_counter,5) =
YM(circ_loop_counter,1);
        transition_holder_matrix(transition_counter,6) =
Circ(circ_loop_counter,1);
        transition_holder_matrix(transition_counter,7) =
PercentArea(circ_loop_counter,1);
        transition_holder_matrix(transition_counter,8) =
AR(circ_loop_counter,1);
        transition_holder_matrix(transition_counter,9) =
Round(circ_loop_counter,1);
        transition_holder_matrix(transition_counter,10) =
Solidity(circ_loop_counter,1);
        transition_counter = transition_counter+1;
        circ_loop_counter = circ_loop_counter + 1;

    elseif data(circ_loop_counter,6) >= 0.7
        rounded_holder_matrix(rounded_counter,2) = Area(circ_loop_counter,1);
        rounded_holder_matrix(rounded_counter,3) =
StDev(circ_loop_counter,1);
        rounded_holder_matrix(rounded_counter,4) = XM(circ_loop_counter,1);
        rounded_holder_matrix(rounded_counter,5) = YM(circ_loop_counter,1);
        rounded_holder_matrix(rounded_counter,6) = Circ(circ_loop_counter,1);
        rounded_holder_matrix(rounded_counter,7) =
PercentArea(circ_loop_counter,1);
        rounded_holder_matrix(rounded_counter,8) = AR(circ_loop_counter,1);
        rounded_holder_matrix(rounded_counter,9) =
Round(circ_loop_counter,1);
        rounded_holder_matrix(rounded_counter,10) =
Solidity(circ_loop_counter,1);
        rounded_counter = rounded_counter+1;
        circ_loop_counter = circ_loop_counter + 1;
    end
end
%% Circularity Pie Chart

piechart = zeros(1,3);
piechart(1,1) = fibrous;
piechart(1,2) = transition;
piechart(1,3) = rounded;

%% AR Pie Chart

c = 1;
ARfibrous = 0;
ARtransition = 0;
ARrounded = 0;

while c <= x
    if AR(c,1) < 2
        ARrounded = ARrounded+1;
    elseif AR(c,1) >= 2 && AR(c,1) < 5
        ARtransition = ARtransition+1;
```

```
    elseif AR(c,1) >= 5
        ARfibrous = ARfibrous+1;
    end
    c = c+1;
end

ARpiechart = zeros(1,3);
ARpiechart(1,1) = ARfibrous;
ARpiechart(1,2) = ARtransition;
ARpiechart(1,3) = ARrounded;

%% Circ Pivot Chart
w = 1/0.05;
pivotchart_values = zeros(1,w);
pivotchart_groups = zeros(1,w);

%Setting up Grouping of Pivot Chart
d = 0;          %used for group names
t = 1;          %used to call the proper part of the array

while d <= 1
    pivotchart_groups(1,t)= d + 0.05;
    d = d + 0.05;
    t = t + 1;
end
f = 1;          %counter for storing values into groupings

while f <= x
    if data(f,6) < 0.05
        pivotchart_values(1,1) = pivotchart_values(1,1)+1;
    elseif data(f,6) >= 0.05 && data(f,6) < 0.1
        pivotchart_values(1,2) = pivotchart_values(1,2)+1;
    elseif data(f,6) >= 0.1 && data(f,6) < 0.15
        pivotchart_values(1,3) = pivotchart_values(1,3)+1;
    elseif data(f,6) >= 0.15 && data(f,6) < 0.2
        pivotchart_values(1,4) = pivotchart_values(1,4)+1;
    elseif data(f,6) >= 0.2 && data(f,6) < 0.25
        pivotchart_values(1,5) = pivotchart_values(1,5)+1;
    elseif data(f,6) >= 0.25 && data(f,6) < 0.3
        pivotchart_values(1,6) = pivotchart_values(1,6)+1;
    elseif data(f,6) >= 0.3 && data(f,6) < 0.35
        pivotchart_values(1,7) = pivotchart_values(1,7)+1;
    elseif data(f,6) >= 0.35 && data(f,6) < 0.4
        pivotchart_values(1,8) = pivotchart_values(1,8)+1;
    elseif data(f,6) >= 0.4 && data(f,6) < 0.45
        pivotchart_values(1,9) = pivotchart_values(1,9)+1;
    elseif data(f,6) >= 0.5 && data(f,6) < 0.55
        pivotchart_values(1,10) = pivotchart_values(1,10)+1;
    elseif data(f,6) >= 0.5 && data(f,6) < 0.55
        pivotchart_values(1,11) = pivotchart_values(1,11)+1;
    elseif data(f,6) >= 0.55 && data(f,6) < 0.6
        pivotchart_values(1,12) = pivotchart_values(1,12)+1;
    elseif data(f,6) >= 0.6 && data(f,6) < 0.65
        pivotchart_values(1,13) = pivotchart_values(1,13)+1;
    elseif data(f,6) >= 0.65 && data(f,6) < 0.7
        pivotchart_values(1,14) = pivotchart_values(1,14)+1;
```

```
    elseif data(f,6) >= 0.7 && data(f,6) < 0.75
        pivotchart_values(1,15) = pivotchart_values(1,15)+1;
    elseif data(f,6) >= 0.75 && data(f,6) < 0.8
        pivotchart_values(1,16) = pivotchart_values(1,16)+1;
    elseif data(f,6) >= 0.8 && data(f,6) < 0.85
        pivotchart_values(1,17) = pivotchart_values(1,17)+1;
    elseif data(f,6) >= 0.85 && data(f,6) < 0.9
        pivotchart_values(1,18) = pivotchart_values(1,18)+1;
    elseif data(f,6) >= 0.9 && data(f,6) < 0.95
        pivotchart_values(1,19) = pivotchart_values(1,19)+1;
    elseif data(f,6) >= 0.95 && data(f,6) <= 1
        pivotchart_values(1,20) = pivotchart_values(1,20)+1;
    end
    f = f+1;
end

%% AR Pivot Chart
AR_limit = 4/0.2;
pivotchart_ARvalues = zeros(1,AR_limit);
pivotchart_ARgroups = zeros(1,AR_limit);

%Setting up grouping of the Pivot Chart
dd = 1;          %used for group names
tt = 1;          %used to call the proper part of the array

while dd <= 5
    pivotchart_ARgroups(1,tt)= dd + 0.2;
    dd = dd + 0.2;
    tt = tt + 1;
end
k = 1;
while k <= x
    if data(k,8) < 1.2
        pivotchart_ARvalues(1,1) = pivotchart_ARvalues(1,1)+1;
    elseif data(k,8) >= 1.2 && data(k,8) < 1.4
        pivotchart_ARvalues(1,2) = pivotchart_ARvalues(1,2)+1;
    elseif data(k,8) >= 1.4 && data(k,8) < 1.6
        pivotchart_ARvalues(1,3) = pivotchart_ARvalues(1,3)+1;
    elseif data(k,8) >= 1.6 && data(k,8) < 1.8
        pivotchart_ARvalues(1,4) = pivotchart_ARvalues(1,4)+1;
    elseif data(k,8) >= 1.8 && data(k,8) < 2
        pivotchart_ARvalues(1,5) = pivotchart_ARvalues(1,5)+1;
    elseif data(k,8) >= 2 && data(k,8) < 2.2
        pivotchart_ARvalues(1,6) = pivotchart_ARvalues(1,6)+1;
    elseif data(k,8) >= 2.2 && data(k,8) < 2.4
        pivotchart_ARvalues(1,7) = pivotchart_ARvalues(1,7)+1;
    elseif data(k,8) >= 2.4 && data(k,8) < 2.6
        pivotchart_ARvalues(1,8) = pivotchart_ARvalues(1,8)+1;
    elseif data(k,8) >= 2.6 && data(k,8) < 2.8
        pivotchart_ARvalues(1,9) = pivotchart_ARvalues(1,9)+1;
    elseif data(k,8) >= 2.8 && data(k,8) < 3
        pivotchart_ARvalues(1,10) = pivotchart_ARvalues(1,10)+1;
    elseif data(k,8) >= 3 && data(k,8) < 3.2
        pivotchart_ARvalues(1,11) = pivotchart_ARvalues(1,11)+1;
    elseif data(k,8) >= 3.2 && data(k,8) < 3.4
        pivotchart_ARvalues(1,12) = pivotchart_ARvalues(1,12)+1;
```

```
    elseif data(k,8) >= 3.4 && data(k,8) < 3.6
        pivotchart_ARvalues(1,13) = pivotchart_ARvalues(1,13)+1;
    elseif data(k,8) >= 3.6 && data(k,8) < 3.8
        pivotchart_ARvalues(1,14) = pivotchart_ARvalues(1,14)+1;
    elseif data(k,8) >= 3.8 && data(k,8) < 4
        pivotchart_ARvalues(1,15) = pivotchart_ARvalues(1,15)+1;
    elseif data(k,8) >= 4 && data(k,8) < 4.2
        pivotchart_ARvalues(1,16) = pivotchart_ARvalues(1,16)+1;
    elseif data(k,8) >= 4.2 && data(k,8) < 4.4
        pivotchart_ARvalues(1,17) = pivotchart_ARvalues(1,17)+1;
    elseif data(k,8) >= 4.4 && data(k,8) < 4.6
        pivotchart_ARvalues(1,18) = pivotchart_ARvalues(1,18)+1;
    elseif data(k,8) >= 4.6 && data(k,8) < 4.8
        pivotchart_ARvalues(1,19) = pivotchart_ARvalues(1,19)+1;
    elseif data(k,8) >= 4.8 && data(k,8) <= 5
        pivotchart_ARvalues(1,20) = pivotchart_ARvalues(1,20)+1;
    end
        k = k+1;
end

%% Overall Average Distance Between Particles

overall_distance_between_points = zeros(x,x);

e = 1;          %first loop counter
t_overall = 1;          %second loop counter

while e <= x
    while t_overall <= x
        overall_distance_between_points(e,t_overall) = 
sqrt(((XM(t_overall,1)-XM(e,1)).^2)+((YM(t_overall,1)-YM(e,1)).^2));
        t_overall = t_overall+1;
    end
    t_overall = 1;
    e = e+1;
end

overall_distance_column_sum = sum(overall_distance_between_points);
overall_distance_overall_sum = sum(overall_distance_column_sum);

overall_average_distance = (overall_distance_overall_sum)/(x*(x-1));

%% Overall Individual Particle Area

overall_average_particle_area_sum = sum(Area);
overall_average_particle_area = overall_average_particle_area_sum/x;

%% Overall Particle Length

overall_average_particle_AR = sum(AR)/x;
overall_average_length = 
sqrt((overall_average_particle_area*overall_average_particle_AR)/pi);

%% Fibrous Average Area & Length
```

```
fibrous_sum_values = sum(fibrous_holder_matrix);

fibrous_average_particle_area_sum = sum(fibrous_sum_values(1,2));
fibrous_average_particle_area = fibrous_average_particle_area_sum/fibrous;

fibrous_average_AR = fibrous_sum_values(1,8)/fibrous;
fibrous_average_length =
sqrt((fibrous_average_particle_area*fibrous_average_AR)/pi);

%% Fibrous Average Distance Between Particles

fibrous_distance_between_points = zeros(fibrous,fibrous);
fibrous_XM_vector = fibrous_holder_matrix(:,3);
fibrous_YM_vector = fibrous_holder_matrix(:,4);

e_fibrous = 1;          %first loop counter
t_fibrous = 1;          %second loop counter

while e_fibrous <= fibrous
    while t_fibrous <= fibrous
        fibrous_distance_between_points(e_fibrous,t_fibrous) =
sqrt(((fibrous_XM_vector(t_fibrous,1)-
fibrous_XM_vector(e_fibrous,1)).^2)+((fibrous_YM_vector(t_fibrous,1)-
fibrous_YM_vector(e_fibrous,1)).^2));
        t_fibrous = t_fibrous+1;
    end
    t_fibrous = 1;
    e_fibrous = e_fibrous+1;
end

fibrous_distance_column_sum = sum(fibrous_distance_between_points);
fibrous_distance_overall_sum = sum(fibrous_distance_column_sum);

fibrous_average_distance = (fibrous_distance_overall_sum)/(fibrous*(fibrous-
1));

%% Transition Average Area & Length

transition_sum_values = sum(transition_holder_matrix);

transition_average_particle_area_sum = sum(transition_sum_values(1,2));
transition_average_particle_area =
transition_average_particle_area_sum/transition;

transition_average_AR = transition_sum_values(1,8)/transition;
transition_average_length =
sqrt((transition_average_particle_area*transition_average_AR)/pi);

%% Transition Average Distance Between Particles

transition_distance_between_points = zeros(transition,transition);
transition_XM_vector = transition_holder_matrix(:,3);
transition_YM_vector = transition_holder_matrix(:,4);
```

```
e_transition = 1;           %first loop counter
t_tranistion = 1;           %second loop counter

while e_transition <= transition
    while t_tranistion <= transition
        transition_distance_between_points(e_transition,t_tranistion) = 
sqrt(((transition_XM_vector(t_tranistion,1)-
transition_XM_vector(e_transition,1)).^2)+((transition_YM_vector(t_tranistion
,1)-transition_YM_vector(e_transition,1)).^2));
        t_tranistion = t_tranistion+1;
    end
    t_tranistion = 1;
    e_transition = e_transition+1;
end

transition_distance_column_sum = sum(transition_distance_between_points);
transition_distance_overall_sum = sum(transition_distance_column_sum);

transition_average_distance = 
(transition_distance_overall_sum)/(transition*(transition-1));

%% Rounded Average Area & Length

rounded_sum_values = sum(rounded_holder_matrix);

rounded_average_particle_area_sum = sum(rounded_sum_values(1,2));
rounded_average_particle_area = rounded_average_particle_area_sum/rounded;

rounded_average_AR = rounded_sum_values(1,8)/rounded;
rounded_average_length = 
sqrt((rounded_average_particle_area*rounded_average_AR)/pi);

%% Rounded Average Distance Between Particles

rounded_distance_between_points = zeros(rounded,rounded);
rounded_XM_vector = rounded_holder_matrix(:,3);
rounded_YM_vector = rounded_holder_matrix(:,4);

e_rounded = 1;           %first loop counter
t_rounded = 1;           %second loop counter

while e_rounded <= rounded
    while t_rounded <= rounded
        rounded_distance_between_points(e_rounded,t_rounded) = 
sqrt(((rounded_XM_vector(t_rounded,1)-
rounded_XM_vector(e_rounded,1)).^2)+((rounded_YM_vector(t_rounded,1)-
rounded_YM_vector(e_rounded,1)).^2));
        t_rounded = t_rounded+1;
    end
    t_rounded = 1;
    e_rounded = e_rounded+1;
end
```

```
rounded_distance_column_sum = sum(rounded_distance_between_points);
rounded_distance_overall_sum = sum(rounded_distance_column_sum);

rounded_average_distance = (rounded_distance_overall_sum)/(rounded*(rounded-
1));

%% Normalized Area % of Each Morphology

overall_area_sum = sum(Area);

fibrous_area_sum = sum(fibrous_holder_matrix(:,2));
transition_area_sum = sum(transition_holder_matrix(:,2));
rounded_area_sum = sum(rounded_holder_matrix(:,2));

area_addition_check = fibrous_area_sum + transition_area_sum +
rounded_area_sum;

fibrous_normalized_area_sum = (fibrous_area_sum / overall_area_sum) * 100;
transition_normalized_area_sum = (transition_area_sum / overall_area_sum) *
100;
rounded_normalized_area_sum = (rounded_area_sum / overall_area_sum) * 100;

%% Exporting Results to Excel
%Writing Overall Data to Excel

col_header={'Particle','Area','STDEV','XM','YM','Circularity','%Area','AR','R
ound','Solidity'};

xlswrite('Results_Holder',col_header, 1,'A1')
xlswrite('Results_Holder',data, 1,'A2')


%Writing Average & STDEV & Particle Information
l = zeros(1,1);
l(1,1) = Circ_Average;

ll = zeros(1,1);
ll(1,1) = Circ_STDEV;

lll = zeros(1,1);
lll(1,1) = AR_Average;

llll = zeros(1,1);
llll(1,1) = AR_STDEV;

lllll = zeros(1,1);
lllll(1,1) = overall_average_distance;

llllll = zeros(1,1);
llllll(1,1) = overall_average_particle_area;

lllllll = zeros(1,1);
lllllll(1,1) = overall_average_length;
```

```
xlswrite('Results_Holder', l, 2, 'A2')
xlswrite('Results_Holder', ll, 2, 'B2')
xlswrite('Results_Holder', lll, 2, 'C2')
xlswrite('Results_Holder', llll, 2, 'D2')
xlswrite('Results_Holder', lllll, 2, 'E2')
xlswrite('Results_Holder', llllll, 2, 'F2')
xlswrite('Results_Holder', lllllll, 2, 'G2')

col_header_2={'Average Circ','STDEV Circ','Average AR','STDEV AR','Average
Distance','Average Particle Area','Average Length'};
xlswrite('Results_Holder', col_header_2, 2, 'A1')

%Circ Pie Chart Values

xlswrite('Results_Holder', piechart, 3, 'A2')

col_header_3={'Fibrous','Transition','Rounded'};
xlswrite('Results_Holder', col_header_3, 3, 'A1')

%AR Pie Chart Values

xlswrite('Results_Holder', ARpiechart, 4, 'A2')
xlswrite('Results_Holder', col_header_3, 4, 'A1')

%Pivotchart Circ
xlswrite('Results_Holder', pivotchart_groups, 5, 'B1')
xlswrite('Results_Holder', pivotchart_values, 5, 'B2')

row_header_Circ={'Circularity'};
row_header_number={'# of particles'};

xlswrite('Results_Holder', row_header_Circ, 5, 'A1')
xlswrite('Results_Holder', row_header_number, 5, 'A2')

%Pivotchart AR
xlswrite('Results_Holder', pivotchart_ARgroups, 6, 'B1')
xlswrite('Results_Holder', pivotchart_ARvalues, 6, 'B2')

row_header_AR={'AR'};

xlswrite('Results_Holder', row_header_AR, 6, 'A1')
xlswrite('Results_Holder', row_header_number, 6, 'A2')

%Fibrous Raw Data
xlswrite('Results_Holder',fibrous_holder_matrix, 7,'A2')

xlswrite('Results_Holder',col_header, 7,'A1')

%Fibrous Particle Data
l_fibrous = zeros(1,1);
l_fibrous(1,1) = fibrous_average_distance;
```

```
ll_fibrous = zeros(1,1);
ll_fibrous(1,1) = fibrous_average_particle_area;

lll_fibrous = zeros(1,1);
lll_fibrous(1,1) = fibrous_average_length;

xlswrite('Results_Holder', l_fibrous, 8, 'A2')
xlswrite('Results_Holder', ll_fibrous, 8, 'B2')
xlswrite('Results_Holder', lll_fibrous, 8, 'C2')

col_header_4={'Fibrous Average Distance','Fibrous Average Particle
Area','Fibrous Average Length'};

xlswrite('Results_Holder', col_header_4, 8, 'A1')

%Transition Raw Data
xlswrite('Results_Holder',transition_holder_matrix, 9,'A2')

xlswrite('Results_Holder',col_header, 9,'A1')

%Transition Particle Data
l_transition = zeros(1,1);
l_transition(1,1) = transition_average_distance;

ll_transition = zeros(1,1);
ll_transition(1,1) = transition_average_particle_area;

lll_transition = zeros(1,1);
lll_transition(1,1) = transition_average_length;

xlswrite('Results_Holder', l_transition, 10, 'A2')
xlswrite('Results_Holder', ll_transition, 10, 'B2')
xlswrite('Results_Holder', lll_transition, 10, 'C2')

col_header_5={'Transition Average Distance','Transition Average Particle
Area','Transition Average Length'};

xlswrite('Results_Holder', col_header_5, 10, 'A1')

%Rounded Raw Data
xlswrite('Results_Holder',rounded_holder_matrix, 11,'A2')

xlswrite('Results_Holder',col_header, 11,'A1')

%Rounded Particle Data
l_rounded = zeros(1,1);
l_rounded(1,1) = rounded_average_distance;

ll_rounded = zeros(1,1);
ll_rounded(1,1) = rounded_average_particle_area;

lll_rounded = zeros(1,1);
lll_rounded(1,1) = rounded_average_length;
```

```
xlswrite('Results_Holder', l_rounded, 12, 'A2')
xlswrite('Results_Holder', ll_rounded, 12, 'B2')
xlswrite('Results_Holder', lll_rounded, 12, 'C2')

col_header_6={'Rounded Average Distance','Rounded Average Particle
Area','Rounded Average Length'};

xlswrite('Results_Holder', col_header_6, 12, 'A1')

%Normalized Area % Distribution by Morphology

xlswrite('Results_Holder', fibrous_normalized_area_sum, 13, 'A2')
xlswrite('Results_Holder', transition_normalized_area_sum, 13, 'B2')
xlswrite('Results_Holder', rounded_normalized_area_sum, 13, 'C2')

col_header_7={'Fibrous % Normalized Area','Transition % Normalized
Area','Rounded % Normalized Area'};

xlswrite('Results_Holder', col_header_7, 13, 'A1')
```